Sedimentology and Geometry of Fluvial and Deltaic Sandbodies in the Eocene Green River Formation, Eastern Utah

Øystein Spinnangr

Thesis for Master degree in Petroleum Geology/Sedimentology

Department of Earth Science
University of Bergen

June 2014

Abstract

A large part of the world's remaining hydrocarbon reserves are located in reservoirs of fluvial origin. The main building blocks of these reservoirs are channel-belt sandbodies with varied geometries and spatial stacking. In the subsurface, their thicknesses can be measured from well logs and/or cores, but their widths remain unknown. The aim of this study is to analyse the fluvial and mouth-bar sandbody thicknesses and widths in the Sunnyside Delta stratigraphic interval of the Eocene Green River Formation in the eastern Utah to find out if there is a relationship between these parameters, which might then possibly be used for subsurface hydrocarbon reservoir predictions.

Conventional sedimentological logging allowed distinction of a wide range of sedimentary facies representing various modes of sediment deposition and 12 subassociations of spatially and genetically related facies representing specific morphodynamic elements of the Green River Formation, including previously unrecognized channel bank-collapse deposits. They jointly form five main facies associations representing particular depositional palaeoenvironments, such as an open-water lacustrine system, a lacustrine shoreface system, a deltaic mouth-bar system, a fluvial channel-belt system and an alluvial delta-plain system. On the basis of the facies associations and their spatial organization, the studied stratigraphic interval is interpreted to have recorded the depositional history of an arid to semi-arid deltaic system building out into a large shallow-water lake. The low-gradient delta topography and large lake-level fluctuations resulted in frequent episodes of extensive flooding of the delta, during which lacustrine carbonate grainstones were deposited as marker stratigraphic horizons.

The sandbodies in the interval have a mean width of ~390 m, a mean thickness of ~9 m, and a mean width/thickness ratio of ~39. The width variance and thereby also the width/thickness ratio variance are both high. This is attributed to three main causes: the variable maturity level of channel-sinuosity development at the stage of channel avulsion; the variable rate of channel aggradation; and a mixture of channel-belt sandbodies formed by vertical, lateral or combined accretion. The role of this last factor was investigated further by dividing the bulk dataset according to the sandbody type: multi-storey multilateral channel-belts, multi-storey unilateral channel-belts, single-storey multilateral channel-belts, single-storey unilateral channel-belts and mouth-bar sandbodies. This grouping significantly reduced the variance in both width and thickness of sandbodies. The mean palaeo-channel bankfull width estimated from abandonment plugs is ~61 m and the mean bankfull palaeo-channel depth estimated from single-storey channel belts is ~6.8 m.

The fluvial system was distributive, and an analysis of the stratigraphic variation in channel-belt cross-sectional dimensions reveals two progradational phases separated a retrogradational phase. Based on this interpretation, two higher-order sequences are inferred, which supports the suggestion of Moore et al. (2012) that the sequences of Keighley et al. (2003) should rather be reconsidered as parasequences. The U8 interval of Keighley et al. (2003), originally attributed to a lowstand systems tract is reinterpreted as a transgressive systems tract. In the present interpretation there is a distinct trend towards narrower and thinner channel-belts in transgressive systems tracts and wider and thicker channel-belts in lowstand systems tracts. Analyses of the sandbody dimensions along depositional strike have also allowed the lateral location of possible fluvial distributive systems depaxes to be recognized.

Acknowledgements

I would like to express my great appreciation to my supervisor Prof. John Howell (CIPR UIB, currently at the University of Aberdeen) for picking out such an interesting study interval, guidance in the field and for editing my thesis. I would also like to offer my special thanks to my co-supervisor Prof. Wojtek Nemec (GEO UiB), although whose participation was unscheduled, joined the project the last couple of months, and provided a much appreciated editorial review of selected chapters.

Second, I would also like to thank the sponsors of the SAFARI project for financing the collection of the heli-lidar dataset and for inviting me to present my preliminary results at the biannual sponsor meetings in both Stavanger and Spain. A special thanks is oriented towards Statoil for covering flight thickets, to and from fieldwork, through sponsoring of the UiB Utah field course.

My field assistant and fellow student Jostein Koldingsnes is thanked for fruitful discussions both in the field and during subsequent studies as well as highly valued comradery. I would also like to thank Andreas Ritterbacher and his field assistant Jonas Aas Torland for doing fieldwork and processing of the heli-lidar data in 2010, Tore Aadland for help generating rose diagrams, and lecturers at the University of Bergen for rewarding and inspirational courses throughout my studies here the last five years.

Lastly I would also like to thank my girlfriend for occasionally managing to take my mind of rocks; my dear mother, Brit, for noticing my planned oral examination day was on a bank holiday; my brother, Salve, for infecting me with enough “nerdyness” to complete this thesis; and last but not least my father, Ånon, for sparking my curiosity towards sedimentology and for his highly appreciated proofreading.

Bergen, 2 June 2014

Øystein Spinnangr

Contents

1. Introduction

Recent estimates for the world's remaining hydrocarbon reserves conclude that 20% are situated in fluvial sandbodies (Keogh et al., 2007). Therefore, knowledge on the dimensions, connectivity, heterogeneity and spatial distribution of such subsurface sandbodies is of key interest for the petroleum industry. This is especially important for the Norwegian Continental Shelf where most of the giant fields are at the tail-off stage of their production. Having produced most of the petroleum from the more convenient marine sands (e.g. marine formations of the Brent Gp.), much of the remaining resources are located in the more difficult fluvial sandbody reservoirs (e.g. Ness, Statfjord, Snadd, and Lunde formations).

Fluvial channel belts are the main reservoir bodies in alluvial successions. Their thicknesses can be measured from well logs and cores, but they are generally thinner than the seismic resolution at hydrocarbon reservoir depths and thus their width and spatial distribution of channel belts cannot readily be imaged. One way to estimate the sub-surface dimensions of fluvial and mouth-bar sandbodies is to study their outcrop analogues. Sandbody widths and thicknesses can be measured from outcrops to analyse their relationships. Such empirical data gathered from outcrops may later be used as input for stochastic reservoir models. This particular issue is the principle aim of the present study: to investigate sandbody thicknesses and widths in order to find out if there is a relationship between these parameters, that might then be used to predict the unknown sandbody width from a known sandbody thickness in a subsurface hydrocarbon reservoir. Sedimentological analysis is used to recognize the genetic type of sandbodies in the studied succession (channel belts vs mouth bars) and to distinguish channel-belt varieties.

Recent advances in the technique of helicopter-based lidar scanning allow huge and poorly accessible cliff outcrops to be scanned in a relatively short time frame. After processing, these heli-lidar data allow for sandbody dimensions to be estimated with a high degree of spatial accuracy.

An extensive, ~20 km wide heli-lidar dataset was collected from the Eocene Green River Formation in the Nine Mile Canyon of eastern Utah, USA, by the SAFARI project during a

campaign in 2010. The sandbodies there are situated within cyclic packages of lacustrine fluvial-deltaic deposits interbedded with lacustrine carbonates, deposited in an arid to semi-arid environment at the margin of the large, internally draining palaeo-lake which filled most of the Uinta Basin. Petroleum exploration of hydrocarbon reservoirs in the basin centre provided a well-documented tectonic and stratigraphic framework for this stratigraphic interval (Bradley, 1931; Dickinson et al., 1988; Keighley et al., 2003; Morgan, 2002; Remy, 1992; Ryder et al., 1976; Taylor and Ritts, 2004). Fieldwork for the present thesis was carried out in May 2013 and the heli-lidar dataset was analysed on a computer workstation at the University of Bergen. The project was supervised by Prof. John Howell (CIPR UIB, currently at the University of Aberdeen) and co-supervised by Prof. W. Nemec (GEO UiB).

2. Regional Geological Setting

2.1 Tectonic Background

The Uinta Basin was one of a series of intermontane basins formed during the Laramide orogeny. Prior to the onset of the Laramide uplift, the study area was located in the foreland basin in front of the Sevier thrust belt, which formed the Western Interior Seaway (**Fig. 2.3AB**) (Dickinson et al., 1988).

The Uinta Basin formed in the Late Cretaceous to early Cenozoic (Dickinson et al., 1988). In contrast to the thin-skinned tectonics of the preceding Sevier orogeny, the Laramide orogeny was dominated by deep-seated tectonics that produced large uplifts separating intermontane basins. The orogeny was related to a change in the angle of subduction of the Pacific oceanic lithosphere under the Laurentian continental lithosphere (Dickinson and Snyder, 1978). During the Sevier orogeny, the subducting slab plunged steeply beneath the Laurentian continent (**Fig. 2.1A**). In the Late Cretaceous, the subduction angle decreased, with the subducting slab shearing against the continental lithosphere and causing the Laramide orogeny (**Fig. 2.1B**) (Dickinson and Snyder, 1978). Several causes have been proposed for this change in subduction angle: (a) an increase in the rate of subduction; (b) a decrease in the age of the subducting oceanic lithosphere, causing it to be more buoyant; and (c) a large-scale geochemical anomaly with more buoyant lithology of the subducting oceanic plate (Dickinson et al., 1988; English and Johnston, 2004).

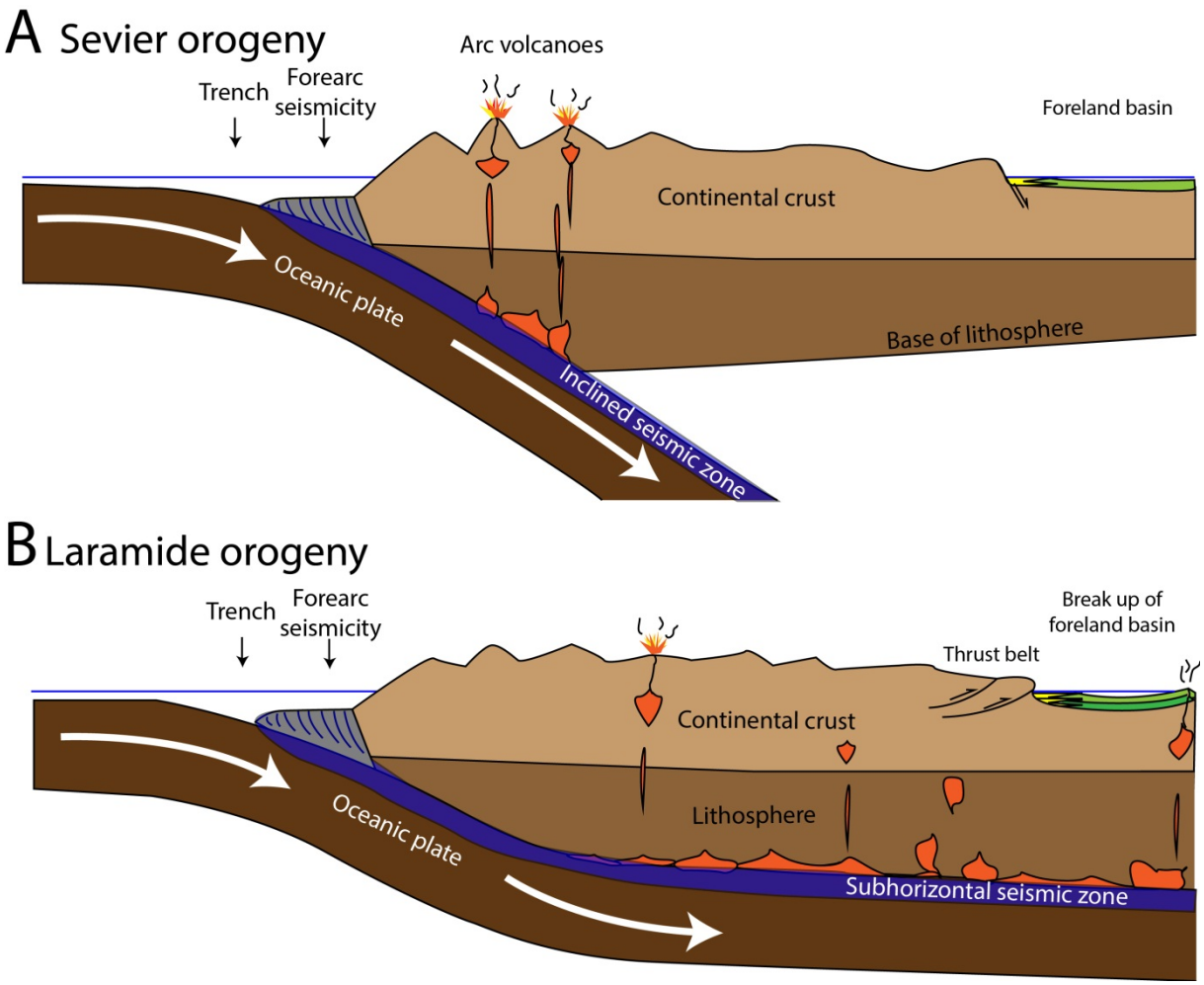

Fig. 2.1. The postulated different subduction modes during (**A**) the Sevier orogeny and (**B**) the Laramide orogeny. Modified from Dickinson and Snyder (1978).

The Laramide orogeny (80 – 55 Ma) caused the Cretaceous foreland basin to break up through the growth of multiple basement-cored uplifts which resulted in the formation of several isolated basins (Dickinson et al., 1988; English and Johnston, 2004). One of the largest of these basins was the Uinta Basin, bounded to the north by the Uinta Mountains, to the south east by the Uncompahgre uplift and to the south west by the San Rafael Swell. The basin was separated from the neighbouring Piceance Creek Basin to the east by the Douglas Creek Arch (**Fig. 2.2**) (Dickinson et al., 1988).

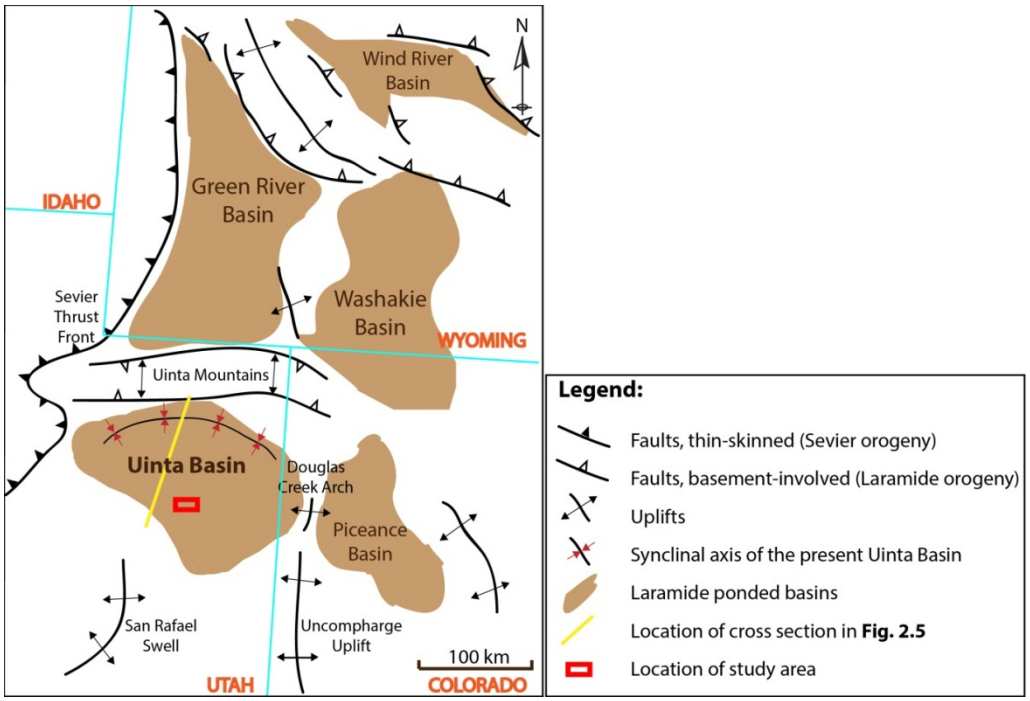

Fig. 2.2. Laramide Basins of the northern Colorado Plateau. Modified from Dickinson et al. (1988) and Keighley and Flint (2008).

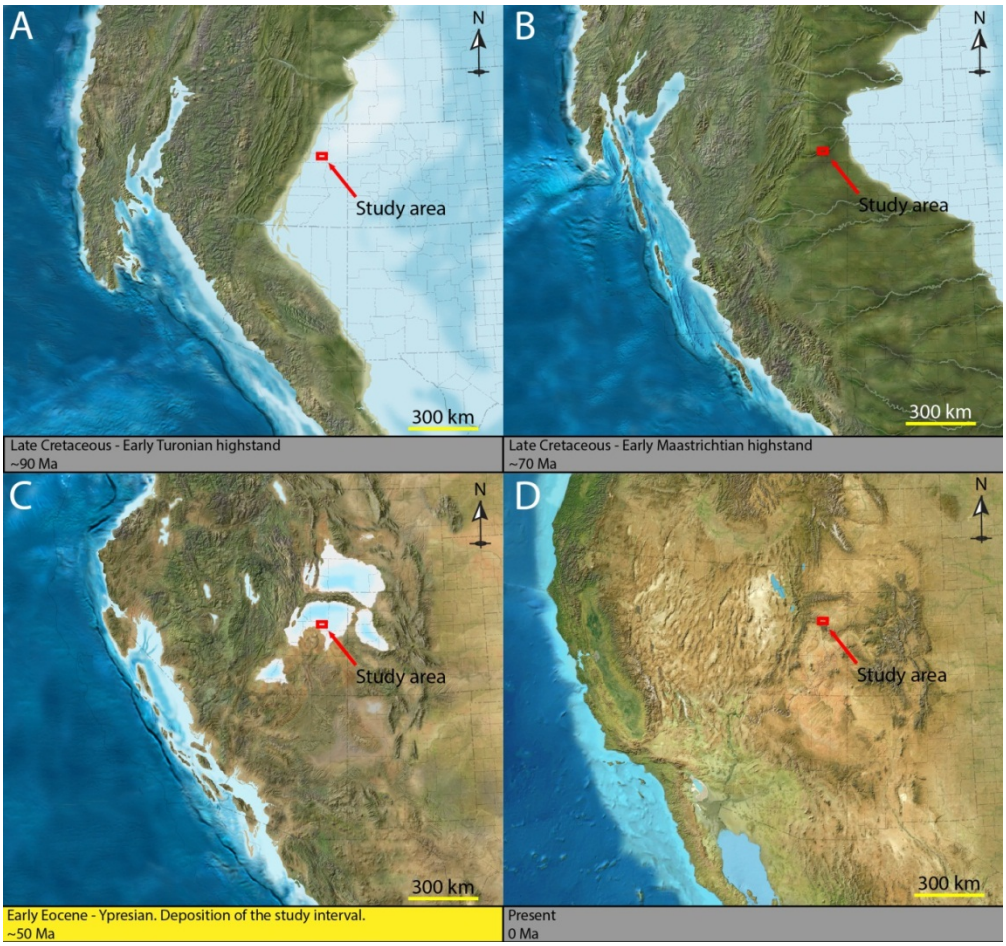

Fig. 2.3. Late Cretaceous-Cenozoic palaeogeography of the western USA. (**A**) Late Cretaceous sedimentation in eastern Utah occurred in a marine foreland basin. (**B**) The onset of Laramide orogenyand retreat of the Western Interior Seaway . (**C**) Early Eocene sedimentation proceeds in internally draining lakes, including the Uinta Basin where the study area is located. (**D**) Present-day geography of the western USA. The location of the study area is marked with a red rectangle. Modified from Ron Blakey's webpage <http://cpgeosystems.com>.

2.2 Stratigraphic Background

The continental deposits of the Uinta Basin overly the marine and marginal marine deposits of the Cretaceous foreland basin (**Fig. 2.3AB**). The onset of the Laramide orogeny resulted in a transition from marine-connected basin to a series of internally draining lacustrine basins which included the Uinta Basin (**Fig. 2.3C**) (Ryder et al., 1976). During the latest Cretaceous (**Fig. 2.4A**) the foreland basin was covered mostly with alluvial-plain sediments, with the exception of local clay-rich deposits in isolated ponds along the axis of the Uinta Basin syncline (**Fig. 2.2**), where the subsidence rate was greatest (Ryder et al., 1976).

By the middle Palaeocene (**Fig. 2.4B**), the Uinta Basin had formed and was occupied by Lake Uinta, a large lake system with open lacustrine deposits trending in SW–NW direction and surrounded by marginal lacustrine and fluvial sediments (Ryder et al., 1976). The sediments encircling the open lacustrine facies on the northern flank of the basin are both coarser, narrower and thicker than those on the southern flank (Keighley et al., 2003). This was caused by the asymmetry of the basin, with a steeper depositional dip on the northern flank and a gentle depositional dip on the southern flank (Ryder et al., 1976). This gentle dip allowed deltas on the southern flank to prograde further into the basin. One of the largest deltaic complexes was centred near the present town of Green River (Remy, 1992). Supplied with feldspathic sands from the Laramide bedrock of San Luis Uplift in the present south-western Colorado, they prograded into the centre of the basin, depositing important reservoir rocks for many of the oil fields in the Uinta Basin (Remy, 1992). These alluvial and deltaic deposits form the Colton, North Horn and Wasatch formations (**Fig. 2.5**) (Ryder et al., 1976). During pluvial periods, Lake Uinta merged with Lake Flagstaff to the west and thick deposits of lake-margin carbonate flats accumulated. These deposits constitute the Flagstaff Member of the Green River Formation (**Fig. 2.5**) (Ryder et al., 1976).

Lake Uinta expanded further during the early Eocene (**Fig. 2.4D**), allowing widespread sedimentation of open-lacustrine organic-rich mudstones and marginal-lacustrine ooid and ostracode carbonate grainstones. These deposits formed a ~30 m thick succession known as the Carbonate Marker Unit, which is distinguishable in subsurface data throughout most of the basin (**Fig. 2.5**) (Remy, 1992; Ryder et al., 1976). This episode was followed by a new episode of major siliciclastic input and the progradation of fluvio-deltaic systems into the basin from the southern shore, including the informally-named Sunnyside Delta interval (Remy 1992) which contains the sedimentary succession studied in this thesis.

During the middle Eocene, the Lake Uinta expanded to its widest extent, allowing another thick succession (~500 m) of organic-rich mudstones to be deposited (Remy, 1992; Ryder et al., 1976). The Mahogany oil shale was deposited during this time of major lake expansion (**Fig. 2.5**) (Ryder et al., 1976). Eventually the lake became hypersaline and evaporites were deposited (Ryder et al., 1976). During the late Eocene and early Oligocene, Lake Uinta was buried under a succession of coarse-grained alluvial deposits of the Uinta and Duchesne River formations (**Fig. 2.5**) (Ryder et al., 1976).

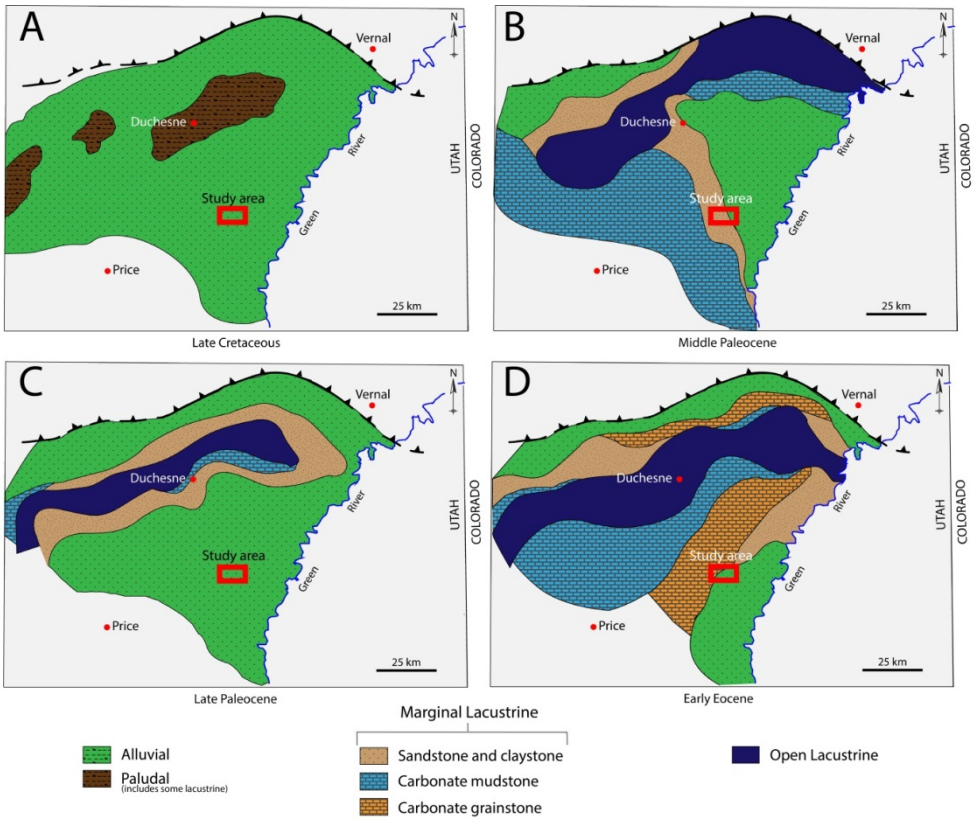

Fig. 2.4. Distribution of depositional environments in western Lake Uinta in (**A**) Late Cretaceous; (**B**) Middle Palaeocene; (**C**) Late Palaeocene, with open lacustrine environment constrained to a relatively narrow zone by prograding shorelines; and (**D**) Early Eocene. The study area indicated by red rectangle. Modified from Ryder et al. (1976).

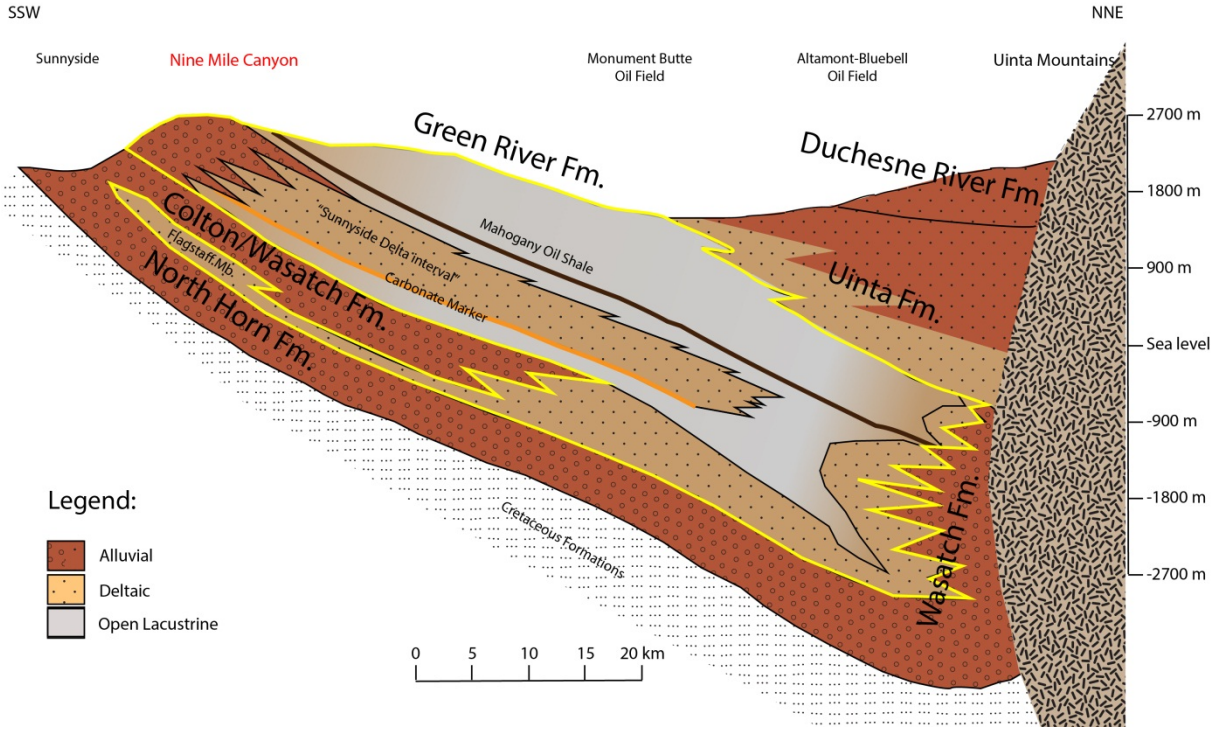

Fig. 2.5. Generalized cross-section through the SW Uinta Basin. The Green River Formation outlined in yellow. Modified from Keighley and Flint (2008) and Moore et al. (2012); based on Fouch (1975), Remy (1992) and Ryder et al. (1976)

2.3 The Green River Formation

There have been various subdivisions of the Green River Formation in the south-central Uinta Basin since the original work of Bradley (1931). Remy (1992) reviewed the previous literature from the south-central Uinta Basin and combined this with detailed fieldwork to produce a composite stratigraphic section for the Green River Formation in the Nine Mile Canyon (**Fig. 2.6C**). Remy (1992) defined the base of the formation at the Carbonate Marker Unit. It is overlying the interval informally named by Remy (1992) as the Sunnyside Delta interval, which comprises ~550 m of sandstones and mudstones of both fluvial and lacustrine origin interbedded with shallow water carbonates (Remy, 1992). The Sunnyside Delta interval is topped by the "Transitional Interval", in which the deposits become increasingly lacustrine and pass upwards passing into the "Upper Member" comprising a ~300 m thick succession of mostly fine-grained deposits lain down in a nearshore to offshore

open-lacustrine environment, at a time when the Lake Uinta was at its widest extent (Remy, 1992).

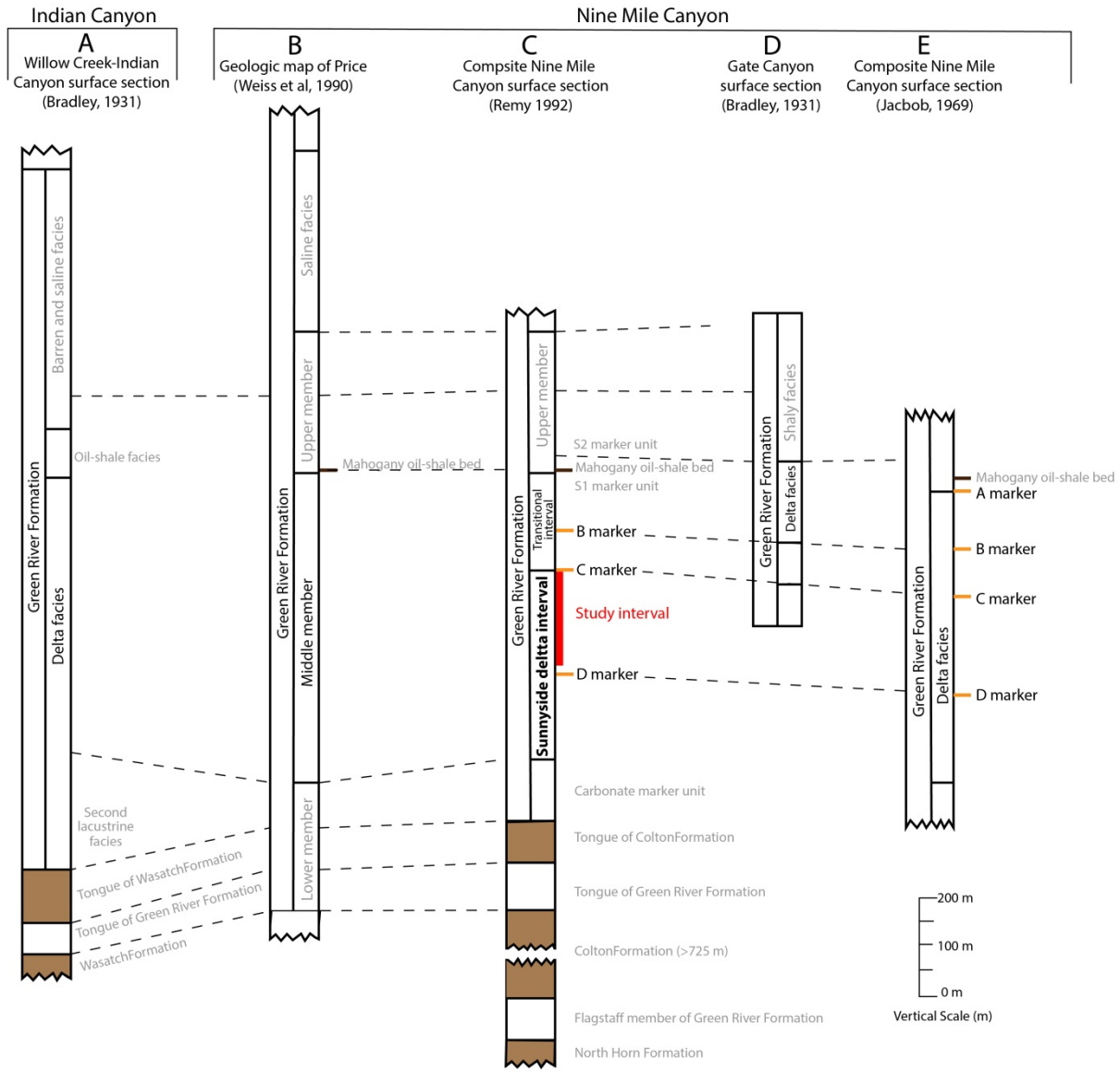

Fig. 2.6. Stratigraphic nomenclature for the Green River Formation in the south-central part of the Uinta basin, Utah. Modified from Remy (1992)

2.3.1 Sunnyside Delta interval

The stratigraphic succession studied is in the upper part of the Sunnyside Delta interval of Remy (1992) (**Fig. 2.6C**). This interval together with the overlying Transitional Interval were referred to as the "Delta facies" by Bradley (1931) and Jacob (1969) (**Fig. 2.6AE**). Geological maps group the Sunnyside Delta with the Transitional Interval as the "Middle Member" (**Fig. 2.6B**) (Remy, 1992).

The Sunnyside Delta interval consists of cyclic packages of alluvial/deltaic deposits interbedded with lacustrine grain-supported carbonates deposited during lake flooding of the delta (Keighley et al., 2002; Moore et al., 2012; Remy, 1992; Ryder et al., 1976; Schomacker et al., 2010; Taylor and Ritts, 2004). Sandbodies in this interval originated in two main environments: (1) a distributive fluvial system of meandering channels with associated crevasse splays and overbank deposits; and (2) a delta-front system of mouth bars intercalated with shallow-water lacustrine sandsheets (Remy, 1992). The relative abundance of fluvial channel-belt and mouth-bar sandbodies has been a topic of some controversy. Most previous publications describe the majority of the sandbodies to be fluvial in origin, whereas a recent publication Schomacker et al. (2010) reinterpreted most of the sandbodies in the Sunnyside Delta interval to have been deposited as mouth-bars by scouring hyperpycnal flows. This interpretation was questioned by Keighley (2013).

2.3.2 Carbonate markers

The Sunnyside Delta interval is commonly subdivided using laterally continuous carbonate marker beds (Jacob, 1969; Keighley et al., 2002; Remy, 1992). Remy (1992) defined the Sunnyside delta interval as extending from the top of the Carbonate Marker Unit upwards to the carbonate marker bed C1 of Jacob (1969). In the study area, the C1 marker is located some 4–18 m above a pair of prominent yellow-weathered ostracode grainstone beds labelled as the C2 and C3 markers by Jacob (1969). Another prominent marker in the Sunnyside Delta interval is the D-marker of Jacob (1969), located ~160 m above the Carbonate Marker Unit and ~215 m below the C1 marker (Remy, 1992). "The D marker consists of approximately 2.0 m of carbonate mudstone, ostracode grainstone, domal stromatolite, greenish-grey mudstone, and a distinctive bed of oolite grainstone containing

ostracode nuclei" (Remy, 1992). The D-marker dips into the subsurface approximately 500 m to the west of the western boundary of the study area.

In addition to the D- and C-markers Keighley et al. (2002) recognized 9 more carbonate markers and labelled them, from the oldest to the youngest, as M1–M11 (with the D-marker = M1 and C3-marker = M11)(**Fig. 2.7**). On this basis, Keighley et al. (2002) divided the interval between markers M1 and M11 into 10 units labelled U1–U10, where U1 overlies marker M1, U2 overlies marker M2 etc.

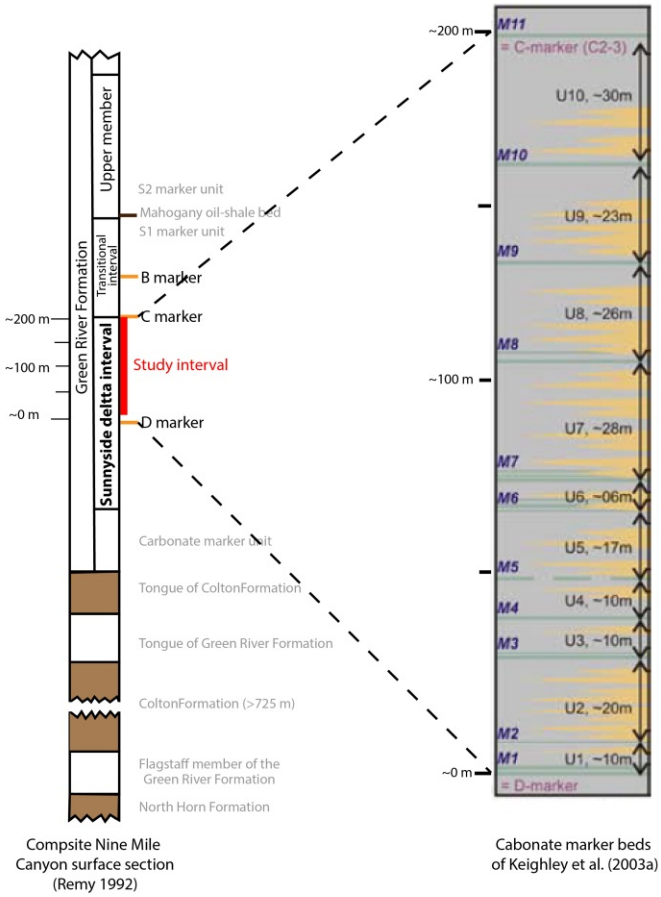

Fig. 2.7. The M1 to M11 marker beds of Keighley et al. (2003) and the corresponding units U1-U10. The thickness given are the average thickness of these units in the area studied by Keighley et al. (2003). Modified from Keighley and Flint (2008); Remy (1992)

2.3.3 Sequence stratigraphy

Sequence stratigraphic concepts, first developed for marine environments, have in later years been successfully applied to terrestrial systems (Keighley et al., 2003). Keighley et al. (2003) highlights the differences between marine-connected systems and systems with a

lacustrine base level. One of the key differences is that lake-level fluctuations can be very rapid and lakes generally have a much shorter lifetime than epicontinental seaways or oceans. The second key difference is that lakes commonly have a very shallow bathymetric profile. A modern-day example of rapid lake-level fluctuations can be observed in the internally draining Lake Turkana in the East African Rift (**Fig. 4.15**).

A high-resolution sequence stratigraphic framework was suggested for the interval between markers M1 and M11 by Keighley et al. (2003) (**Fig. 2.8**, right hand column). They describe cyclic alterations of ~20 m thick floodplain-dominated intervals overlying ~10 m thick lacustrine-dominated intervals (**Fig. 2.8**)(Keighley et al., 2003). Sequence boundaries are placed where there is an abrupt basinward shift in facies across a regional mappable surface (Keighley et al., 2003; Van Wagoner, 1988). Two types of sequence boundaries were distinguished. Type A sequence boundaries are placed where lacustrine-dominated intervals are overlain erosionally by floodplain-dominated intervals and/or where there is an angular unconformity between the lacustrine and floodplain intervals. Type A boundaries were interpreted above the M2, M8, M9 and M10 carbonate markers (**Fig. 2.8**)(Keighley et al., 2003). Type B sequence boundaries were placed where lacustrine-dominated intervals pass gradually upwards into floodplain-dominated intervals without a distinct erosion surface or angular unconformity. Type B boundaries were interpreted above the carbonate markers M4 and M7 (**Fig. 2.8**) (Keighley et al., 2003).

Major lacustrine flooding surfaces were inferred where alluvial deposits abruptly pass upward into lacustrine deposits. Since most of these contacts involve a carbonate marker, the carbonate markers can be used as indicators of flooding surfaces. The maximum flooding surfaces were inferred as surfaces where a thin oil shale is present, interpreted to have been deposited in a profundal setting (Keighley et al., 2003). Maximum flooding surfaces were postulated above the carbonate markers M2 and M9 (**Fig. 2.8**) (Keighley et al., 2003).

In the interval beneath the M10 carbonate marker in the Argyle Canyon, Moore et al. (2012) recently labeled some of the sequences of Keighley et al. (2003) as lacustrine parasequences, using flooding surfaces as parasequence boundaries (after Van Wagoner (1988). Moore et al. (2012) have interpreted the interval M1-M10 as deposited in a fluvial-

influenced marginal lacustrine setting, rather than in a lacustrine-influenced fluvial setting suggested by Keighley et al. (2003).

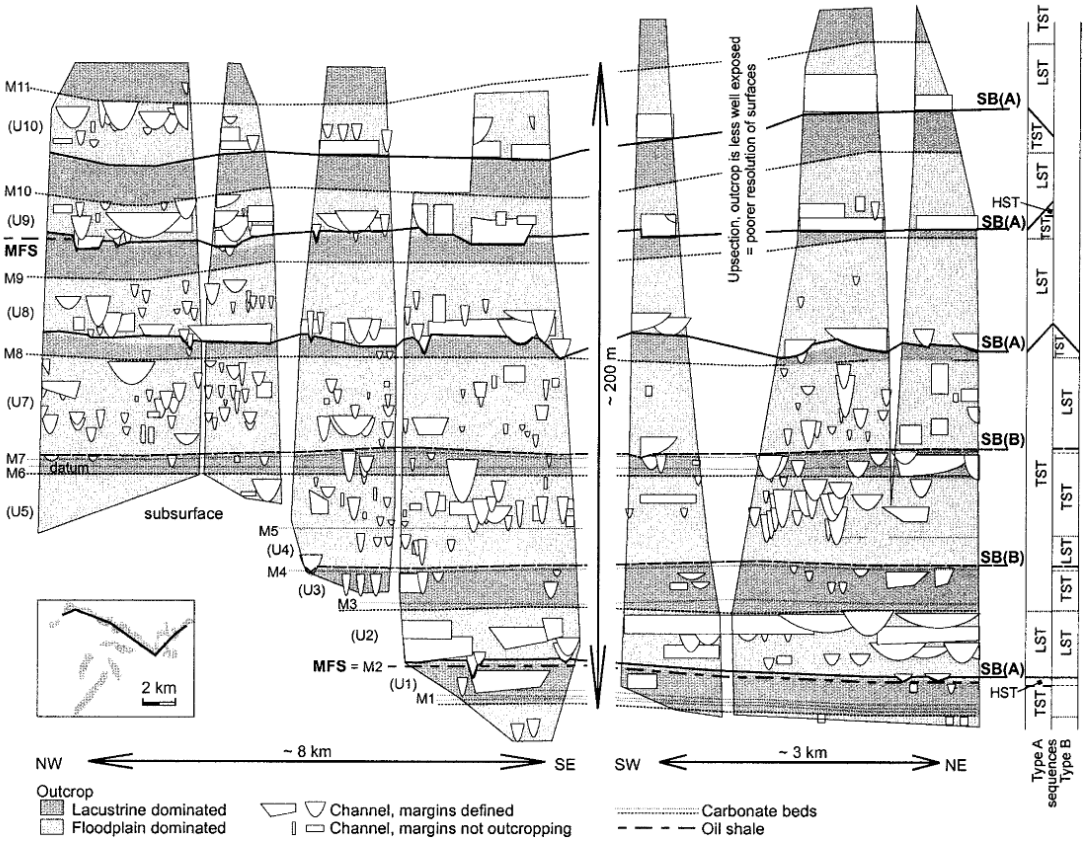

Fig. 2.8. Summary panel of the Keighley et al. (2003) photomontaged sections. M1-M11 are carbonate marker beds, dividing the stratigraphic interval into units U1-U10. MFS = maximum flooding surface, SB(A) = type A sequence boundary, SB(B) = type B sequence boundary, LST = low stand systems tract, TST = transgressive systems tract, HST = highstand systems tract. From Keighley et al. (2003)

2.4 Study Area

The study area is located in the Nine Mile Canyon on the border between Carbon and Duchesne counties of eastern Utah, approximately 60 km north east of the city Price (**Fig. 2.9B**). It is approximately 13 km wide and stretches from the junction with Gate Canyon in the west to the junction with Devils Canyon in the east.

The area was chosen because of its good and laterally continuous exposures of channelized sandstones, situated within a well-documented structural and stratigraphic framework. The general dip of the studied succession along strike of the canyon, from west to east is ~-1.7 degrees, while the drop in elevation of the canyon floor, in the same interval, is ~-1 degree.

The exposed study interval therefore generally thins from 130 m thick in the western part to 80 m thick in the easternmost part as the stratigraphy dips down under the valley floor. The interval dips ~5 degrees northwards towards the centre of the Uinta Basin. The maximum thickness of the study interval in the study area is ~165 m is found near the junction with Blind Canyon. The vegetation in the area decreases from west to east because of the ~150 m drop in elevation, leading to a more arid climate eastwards, but even in the west it is so sparse that it does not cause any visibility issues in the study area.

Fig. 2.9. (**A**) Map of western USA with the location of north-eastern Utah shown in red rectangle (**B**) Map of north-eastern Utah with location of study area shown in yellow rectangle (**C**) Study area outlined with orange polygon. Maps from Google Earth™.

3. Methods

3.1 Description of Lidar Technology

3.1.1 Terrestrial lidar

Lidar devices consist of a laser that measures the distance and angles from the scanner to a reflective surface. Together with satellite navigation data it puts the point into a 3D coordinate system. Lidar devices are capable of collecting hundreds of thousands of these points per second, resulting in a large cloud of 3D points (**Fig. 3.1A**) (Bellian et al., 2005; Rittersbacher et al., 2013). These 3D points can be made triangulated to create a surface (**Fig. 3.1B**). Photographs are simultaneously collected with the points and used to create a texture for the surface (**Fig. 3.1C**). The final result is a photorealistic 3D model of the scanned area (Rittersbacher et al., 2013). The term Virtual Outcrop will be used in this thesis when discussing these 3D models of a geologic outcrop.

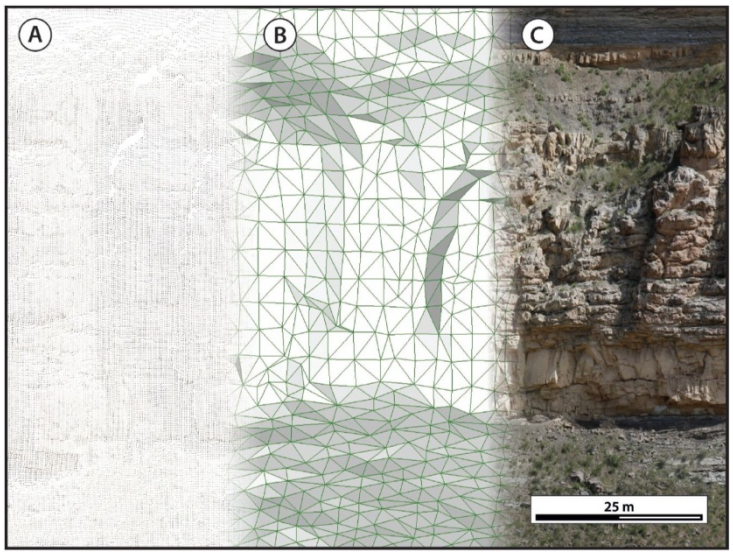

Fig. 3.1. Processing stages of building a virtual outcrop. (**A**) Lidar 3D point cloud; (**B**) triangulated surface made from the 3D point cloud; (**C**) Photographs added as texture onto triangulated surface. From (Rittersbacher et al., 2013) after (Buckley et al., 2008).

Terrestrial based lidar scanning has been widely used for geological purposes over the last decade (Rittersbacher et al., 2013). It is a better tool for capturing the three dimensionality of a geological outcrop, than classic photomosaics which only show the outcrop in two

dimensions, making objects proximal to the position of the camera seem larger in comparison to objects distal to the camera.

Terrestrial based lidar scanning has several limitations, especially when studying very large cliff sections. When scanning an outcrop with a scanner positioned at the base of the outcrop, "scan shadows" may appear in areas that are not in line of sight of the scanner e.g. behind ledges and terraces (**Fig. 3.2**). This results in empty holes in the virtual outcrops (Rittersbacher et al., 2013). The scanner range is also a limitation, while this varies between different lidar devices; the maximum range is usually around ~1 km. The scanner therefore has to be moved and set up in multiple locations in order to scan larger outcrops. The final limitation is that in large outcrops, the photos taken with the camera linked to the scanner are often not taken from an optimal angle, reducing the quality of the virtual outcrop. Although the time needed to collect each single scan has greatly improved since the first lidar scanners were used to scan outcrops (S. Buckley, oral comm. 2014), scanning long sections is still a time consuming process, often taking days.

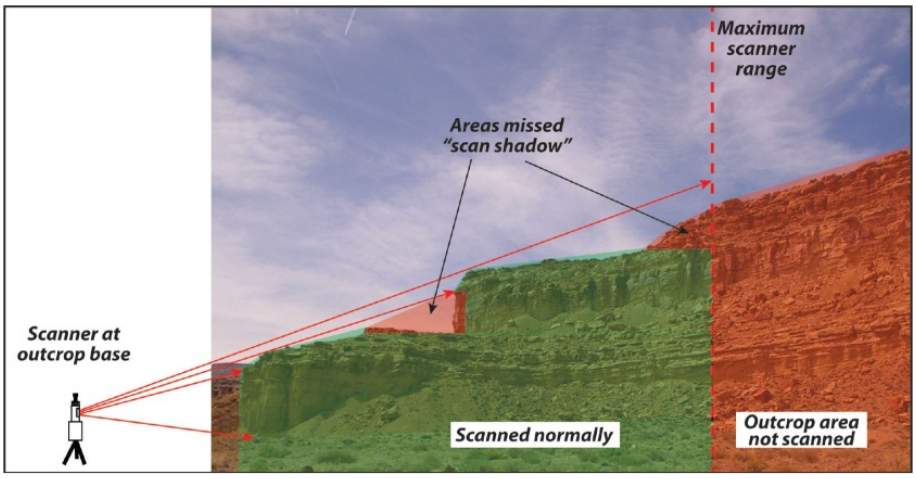

Fig. 3.2. Terrestrial lidar scanning limitations. "Scan shadows" appear behind ledges and terraces, maximum range is ~1 km. From Rittersbacher et al. (2013)

3.1.2 Helicopter-based lidar

Many of the limitations with the terrestrial based lidar scanner can be removed by mounting the scanner on to an airborne vehicle. The airborne based lidar scanning technique removes scan shadows caused by ledges and back-stepping benches in the outcrop and provides an optimal platform for acquiring the images. Huge outcrops, that would have taken days to

scan with ground based lidar, can be scanned in hours, and the problem with accessibility to suitable scanning locations is decreased to accessibility to airfields within range and flight permits. Due to weight limitations commercial UAVs are unsuited for carrying current lidar equipment. Both small planes and helicopters are however suitable to carry the equipment needed, but scanning the outcrops from a plane's birds-eye perspective does not capture much of the geology that is usually exposed in vertical cliff-faces, the best angle for scanning an outcrop is therefore from an oblique angle. Helicopters' ability for low altitude and precise flying is therefore the most suitable object to mount the lidar equipment onto.

The basics of helicopter based lidar scanning is the same as terrestrial based lidar scanning (a laser scanner and a digital camera), but in contrast to the stationary position of the lidar scanner during a terrestrial based scan, the helicopter is in constant motion which adds complexity to calculating the position of the point on the cliff. To address this a GNSS ("global navigation satellite system") antenna is mounted on the side of the helicopter to continuously store the position of the scanner, together with an MSU ("inertial measurement unit") that records the orientation of the helicopter. This enables the distance and angle from the scanner to the outcrop to be calculated, and correct placing of the points in a global reference system (Rittersbacher et al., 2013).

There are however some limitations with heli-lidar scanning, new scan shadows may occur underneath overhangs, huge amounts of data have to be stored, processed and later visualized, the costs related to heli-lidar data are quite high, and in addition there are restrictions in importing the lidar equipment into several states due to weapons grade measurement units in the setup (Rittersbacher et al., 2013). However, overall the approach provides very high quality data, over large areas and was highly suited to the outcrops studied in this project.

3.2 Data Collection

The Heli-lidar data from the Nine Mile Canyon was collected by the SAFARI project as part of Andreas Rittersbachers PhD project (Rittersbacher 2012). The data were processed and the virtual outcrop created, but never interpreted. In 2013 the virtual outcrops and seven logs collected during fieldwork in 2010 were passed on to form the basis of this MSc project.

More fieldwork by the present author was executed in May 2013. This resulted in seven more logs from within the study area.

3.2.1 Heli-lidar

The virtual outcrop from the Nine Mile Canyon was collected in 2009 by the SAFARI project. All the components needed for the scanning was coordinated by a system called the Helimap System, which was originally developed to measure snow volumes in the Alps to determine avalanche risks (**Fig. 3.3**) (Vallet and Skaloud, 2004). The scanner used was a Riegl LMS Q240i-60 airborne laser scanner. A Hasselblad H1 22 megapixel digital camera with a calibrated 35 mm lens was mounted on the side of the scanner, taking photos simultaneously with the laser scanning. To record the helicopter's constant movement a dual frequency Global Navigation Satellite System (GNSS) was mounted on the setup, measuring the helicopter trajectory up to ten times per second. The angle from the scanner to the outcrop was recorded by an inertial measurement unit (IMU) that was mounted under the digital camera, measuring the orientation angle of the scanner hundreds of times per second (Rittersbacher et al., 2013). The scanner continuously recorded a vertical 2D profile, by using the IMU and GNSS data a horizontal dimension later added, resulting in a 3D scan. A detailed description of the Helimap System can be found in Vallet and Skaloud (2004).

Fig. 3.3. The Helimap System mounted on a commercial helicopter during the SAFARI projects heli-lidar campaign in Utah in 2009. Modified from Rittersbacher et al. (2013)

3.2.2 Fieldwork

Fieldwork was executed during the periods 13-16 May and 25-31 May 2013. The first day was used for reconnaissance of the study area and to review the previous work in the area between Argyle Canyon and Nine Mile Canyon (Keighley et al. (2002); Schomacker et al. (2010) and in the nearby Parley Canyon (Moore et al. (2012); Taylor and Ritts (2004). The second day was used to locate Ritterbacher's logging routes anno 2010 and locating new suitable logging routes, the rest of the fieldwork involved collecting seven sedimentary logs. The logging was done using traditional sedimentary logging techniques at a scale of 1:50. At the end of each day the logging routes were traced out directly onto the Virtual Outcrop. The final data set includes a total of 827 m of log, 395 m from Ritterbacher and 432 m from the current study.

3.3 Analysis of Field Data

3.3.1 Processing of heli-lidar data

In order to make a virtual outcrop suitable for geologic analysis from the collected raw point cloud and photographic data, the data needs to be processed, this was done by Rittersbacher in 2009. It was done in several steps described in Rittersbacher et al. (2013) summarized below:

- **Dividing up data in modules:** The main difference in processing terrestrial based lidar data and heli-lidar data is the number of 3D points. To make the data more manageable for processing, the data was segmented up in modules of ~1-2 km length. This resulted in 15 modules, labelled 9MC_1 to 9MC_15, see **Fig. 3.4**.
- **Reducing point cloud density:** The density of points collected exceed the precision of the Helimap System, and therefore contained significant noise (Rittersbacher et al., 2013). To reduce both the total storage space needed for the data and also the noise, the density of the point cloud was strongly reduced and smoothed (**Fig. 3.5A**).
- **Creating 3D surface:** Creating a 3D surface by triangulating between the points in the point cloud. This was done with the software PolyWorks v11.0.12. (**Fig. 3.5BC**).
- **Adding texture:** The digital photographs that were collected simultaneously as the lidar scanning were added onto the triangulated surface. The principle is adding colour from the photographs onto each of the triangles building up the surface. The result is a realistic 3D model of the outcrop (**Fig. 3.5D**).

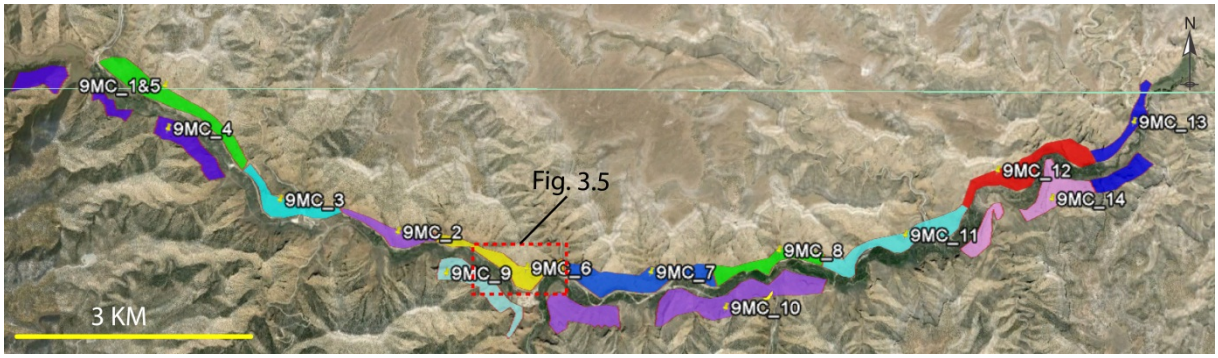

Fig. 3.4. Virtual Outcrop divided into 15 modules. Location of **Fig.3.5** shown with red stippled line. Background map from Google Earth™.

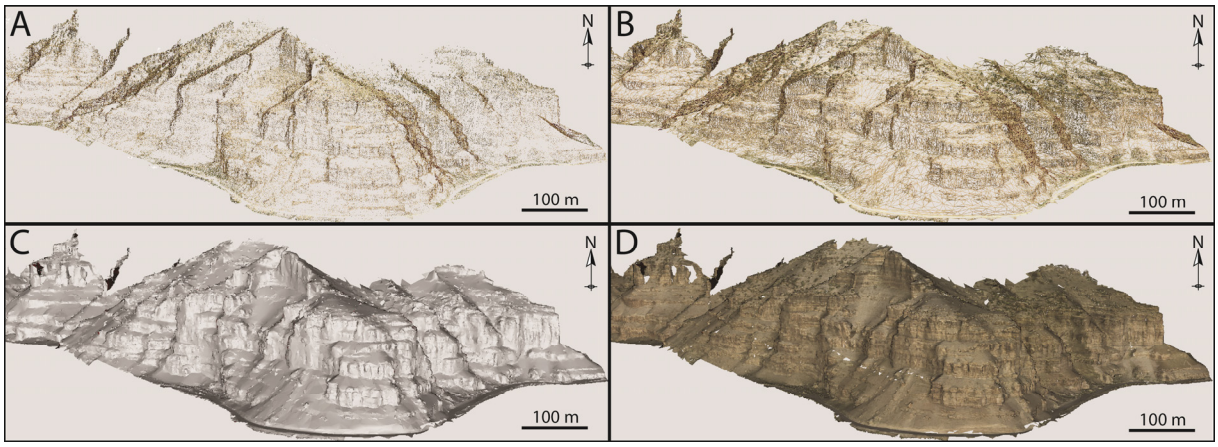

Fig. 3.5. Processing steps when building virtual outcrop. Example from the 9MC_6 module, located west of the junction between Nine Mile and Daddy Canyon, looking towards North (Location shown with red stippled box in **Fig. 3.4.** The scale represents the nearest cliff-face. (**A**) Point cloud (**B**) Triangulation results in a wireframe (**C**) Wireframe is made solid making a surface with artificial shading (**D**) Photographs added onto model as texture with artificial shading.

3.3.2 Digitalization of sedimentary logs

The sedimentary logs were digitized using the SedLog software described in Zervas et al. (2009) and are included in the appendix.

3.3.3 Interpretation on the Virtual Outcrop

The in-house software Lime v0.5.3 was used for interpretations. It allows users to interpret directly onto the virtual outcrop. Interpreted lines are based on extrapolation between user defined points that have a x,y,z coordinate, automatically created when clicking on the virtual outcrop while in editing mode. The following steps were used for interpreting the Nine Mile Canyon Virtual Outcrop:

Mapping out carbonate markers in the interval: To provide a framework for the interpretation and to tie to previous work, the carbonate markers were mapped on to the virtual outcrop. As many of the carbonate markers are locally eroded by above sandbodies or covered by scree, the following approach was made to extrapolate their position into areas with no exposure: Since all the carbonate markers are sub-parallel the most continuous marker, the M11, was interpreted and the interpreted line was exported out of the Lime software and imported into the seismic interpretation software Petrel™ as points. The points were transformed into a solid surface and multiple copies of the surface were

made and shifted down in the z direction so that when exported back into the Lime software they would help to locate the carbonate markers were they were present in the dataset (**Fig. 3.6**).

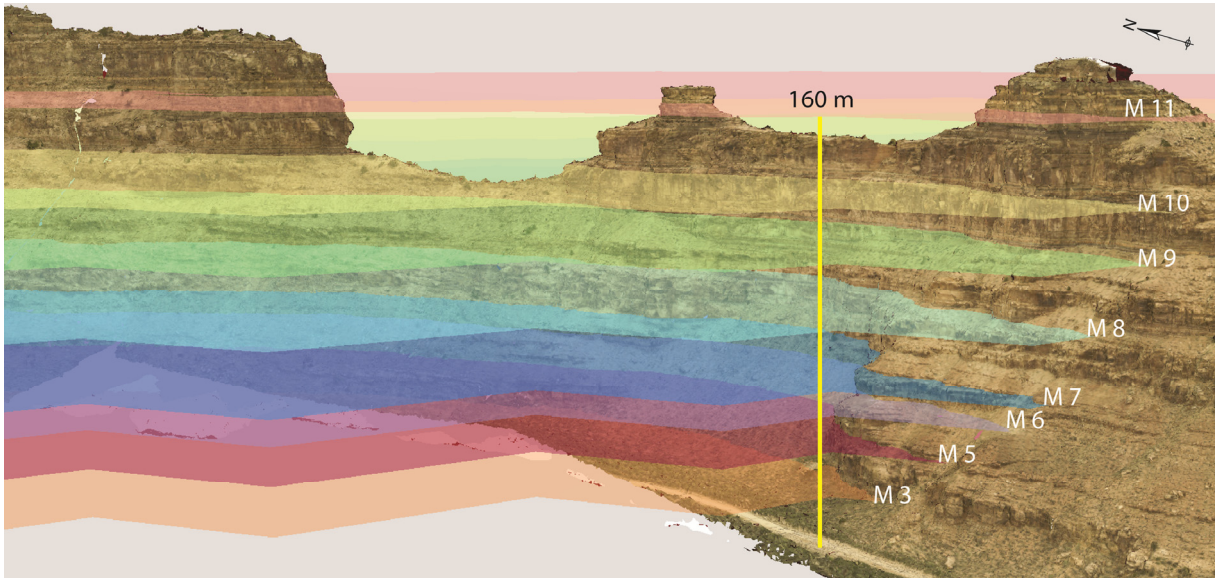

Fig. 3.6. Western part of the 9MC_3 module. Coloured surfaces represent carbonate markers M3-M11. They are created based on the well exposed M11 marker, and shifted down in the z-direction to represent the less well exposed carbonate markers below. Height from road and up to the M11 is ~160 m (yellow line).

Mapping of sandbodies: All major sandbodies (~>3 m max. thickness) were mapped. This was done by interpreting their upper and lower boundary and lateral terminations. If sandbodies extended into areas of poor or no exposure, and there was a sandbody with similar dimensions and properties continuing on the other side of the poor exposure, an interpretation was made whether or not to connect the two sandbodies. If the extent of the poor exposure was too wide to make a reasonable connection then the two sandbodies were interpreted as separate units. This "confidence width" varied with the dimensions of the sandbodies, e.g. a 15 m thick sandbody extending 2 km on either side of a 250 m wide area with no exposure may be correlated, while a 5 m thick sandbody extending 200 m on either side would be interpreted as two different sandbodies. Another factor when deciding on the "confidence width" was studying the topography of the outcrop and determining the likelihood that the sandbody extends below the non-exposed interval. The measured sandbodies were documented an Excel™ spreadsheet. Each sandbody was given a unique ID and the following variables were measured:

- Width, measured in a direct line between margins (X)
- Maximum thickness (Z)
- Average thickness (estimation)
- Orientation between the two margins of the sandbody
- Height below the local datum (M11)
- Distance east of the western most point of the Virtual Outcrop, Gate Canyon.

3.3.4 Grouping of sandbodies

The interpreted sandbodies were grouped according to their mode of deposition and stacking pattern into five sub-groups, one group for sandbodies of mouthbar origin and four groups of fluvial origin. The distinction between mouthbars and fluvial channel-belts is based on observations fitting with the facies associations FA-MB (mouthbar) and FA-F (fluvial channel-belt system) (see section 4.3). The grouping of the fluvial channel-belts is based on the stacking pattern of individual storeys, into "single-storey unilateral" for channel-belts consisting of only one storey (**Fig. 3.7A**), "single-storey multilateral" for channel-belts consisting of only one storey in the vertical direction and with minimum of two storeys laterally (**Fig. 3.7B**), "multi-storey unilateral" for channel-belts consisting of a minimum of two storeys vertically and only one storey laterally (**Fig. 3.7C**), "multi-storey multilateral" for channel-belts consisting of a minimum of two storeys vertically and two storeys laterally (**Fig. 3.7D**). An example from the Virtual Outcrop is shown in **Fig. 3.8**.

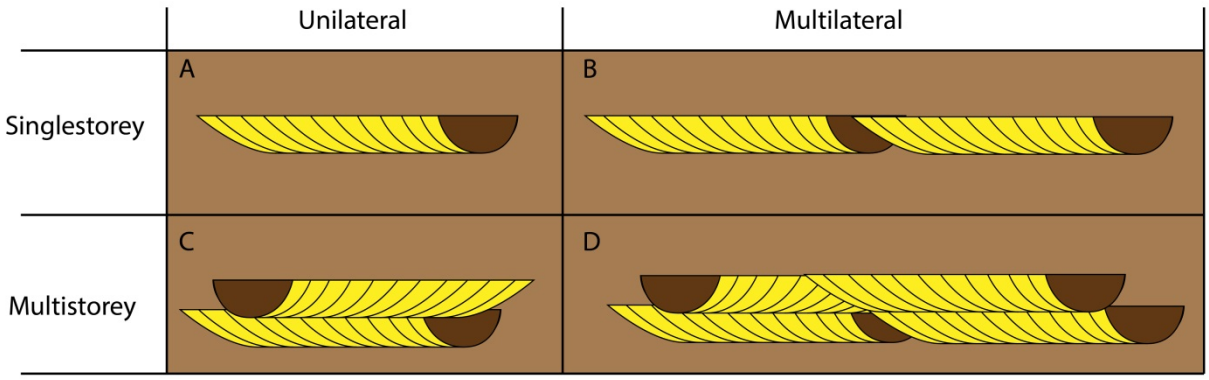

Fig. 3.7. Simple sketch illustrating grouping of fluvial channel-belts based on stacking pattern of storeys. (**A**) Single-storey unilateral, (**B**) Single-storey multilateral, (**C**) Multi-storey unilateral, (**D**) Multi-storey multilateral. Note that the sketched storeys are vertically exaggerated.

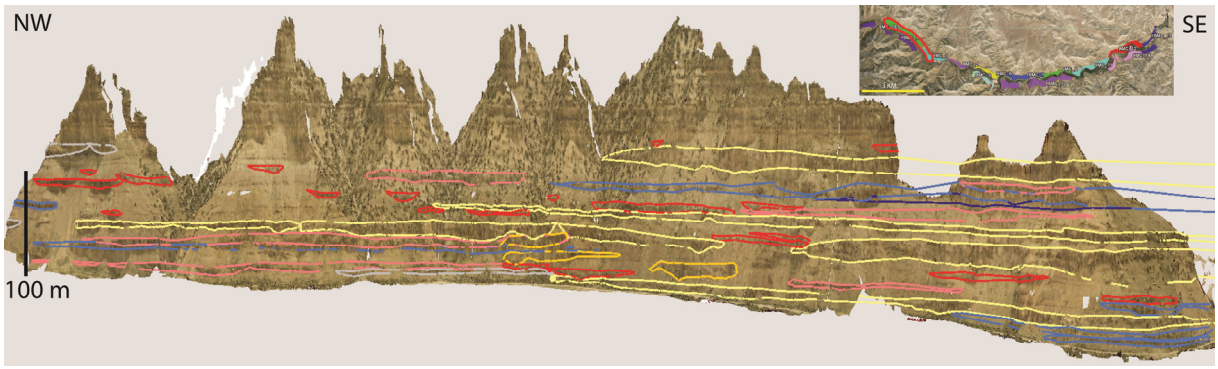

Fig. 3.8. ~3 km wide section in the western most part of the Virtual Outcrop, between Gate Canyon and Blind Canyon, location is show with red outline on the embedded map. Exaggerated vertical scale (3x). Interpreted sandbodies are grouped in red: SU, pink: SM, orange: MU, yellow: MM, blue: MB, grey: undifferentiated.

3.3.5 Correcting sandbody width

The width of a sandbody is measured in straight line between its two margins. Since outcrop orientation is rarely perpendicular to the palaeocurrent of the sandbody, the apparent width measured on the Virtual Outcrop is in most cases an overestimation of the true width of the sandbody. The true width of the sandbody may be calculated using the simple trigonometric approach of Fabuel-Perez et al. (2009):

Calculation of sandbody real width:

$$Wr = Wa \times \sin \mu \qquad \text{(Equation 1)}$$

$$\mu = \beta - \phi \qquad \text{(Equation 2)}$$

Wr = real width, Wa = apparent width, β = orientation between margins, and ϕ = sandbody palaeocurrent (**Fig. 3.9**)

Since palaeocurrents have not been measured for each individual sandbody in the interval an average of all measured palaeocurrents was used as input. All widths given in this study are corrected widths unless otherwise is noted.

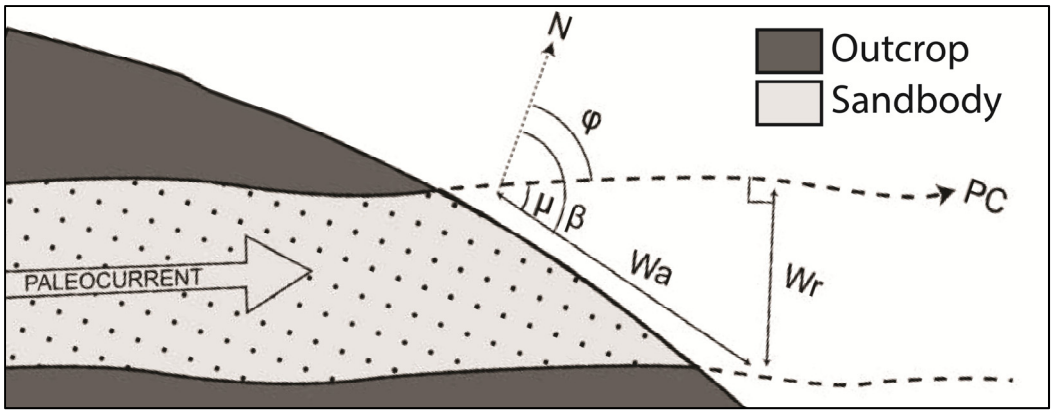

Fig. 3.9. Illustration of the different variables in equation 1 and 2. Slightly modified from Fabuel-Perez et al. (2009)

3.3.6 Palaeocurrent analysis

The collected palaeocurrents are grouped in both a bulk palaeocurrent dataset and sub-datasets from the individual logging locations. Rose diagrams were plotted using the statistical computer program R™ (provided by the R Project for Statistical Computing). Statistical analysis on the palaeocurrent data-sets includes calculating mean direction and angular standard deviation. The Kuiper, Watson and Rayleigh tests were done to verify whether the palaeocurrents have a preferential direction or not (Nemec, 2005).

Estimation of channel-sinuosity (S) for the bulk palaeocurrent dataset done based on the calculated angular standard deviation using the method suggested by Le Roux (1992a).

The Le Roux (1992b) formulae for estimation of channel sinuosity:

$$S = \pi(\frac{\varphi}{360})/\sin(\frac{\varphi}{2}) \quad \text{for } \varphi \leq 180° \quad \text{(Equation 3)}$$

$$S = \pi(\frac{\varphi}{360})/\sin(\frac{360-\varphi}{2}) \quad \text{for } \varphi > 180° \quad \text{(Equation 4)}$$

φ = “operational range” of palaeocurrent direction = 3.2 x the angular standard deviation

3.4 Sources of Error

- Poor quality of the Virtual Outcrop in some parts may distort sandbodies causing errors in the measurements.
- In the easternmost part of the study area the Virtual Outcrop is poorly processed (9MC_11 module), the texture does not fit the topography.

- Sandbody boundaries are difficult/impossible to distinguish on the Virtual Outcrop in very amalgamated intervals.
- Difficult/impossible to distinguish facies in certain non-logged sections of the Virtual Outcrop
- A mean palaeocurrent is used to correct all sandbody widths. Since there is a big scatter in measured palaeocurrents this may cause significant errors in calculating true widths.

3.5 Statistical Methods

3.5.1 Exceedence frequency plots

In order to reveal the distribution type of the sandbody widths and thicknesses, exceedence frequency plots were made (Drummond and Wilkinson, 1996; Middleton et al., 1995). Exceedence frequency, $EF(x_i)$, of a particular value x_i of the measured variable (x) is defined as the number of data (n_i) with values greater than x_i , divided by the total number of data (n) (Nemec, 2005).

$$EF(x_i) = \frac{n_i(x>x_i)}{n} \quad \text{(Equation 5)}$$

By plotting the EF (x_i) against (x_i) the data will plot with different shapes depending on their distribution (**Fig.3.10**, first row). By applying various combinations of logarithmic and probability scales on the, x and y axis, the data will plot out linearly revealing the distribution type of the data (**Fig. 3.10**, green boxes).

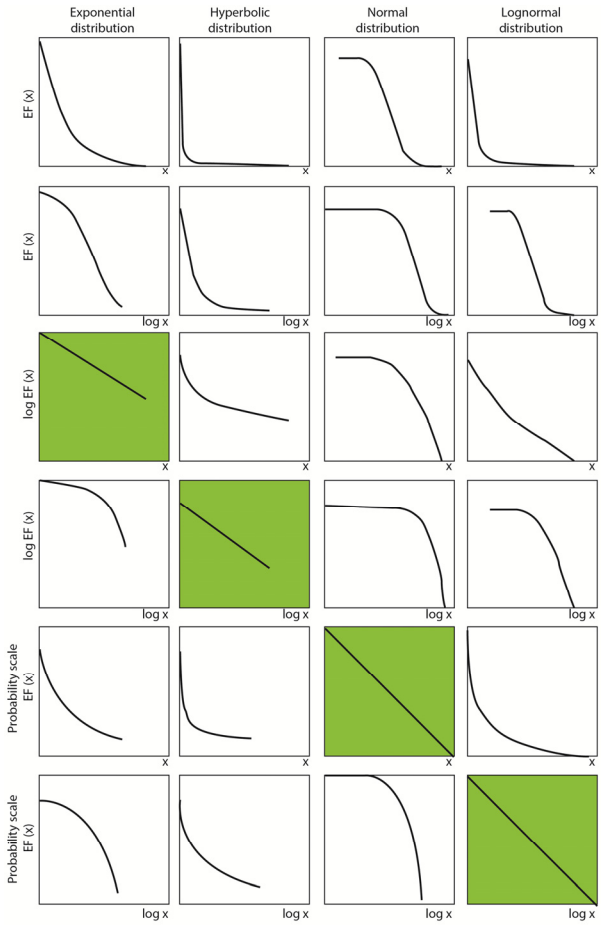

Fig. 3.10. Exceedence frequency (EF) plots of four common types of data distribution in different scales. Used to recognize dataset distribution type. Four scale combinations (highlighted in green) make the plotted data linear, and the distribution type may be recognized. Slightly modified from Nemec (2005).

To identify normal and lognormal distribution a probability scale is needed on the y-axis. This scale is not implemented into the Microsoft Excel™ software and therefore it either needs to be plotted manually on a pre-made probability scale or by making a probability scale manually in Excel™. Because EF plots are made for multiple datasets, a probability scale was manually made in Microsoft Excel™ by following a method outline by Peltier Technical Services, Inc., retrived from http://peltiertech.com/Excel/Charts/ProbabilityChart.html. This resulted in the scale seen in **Fig. 5.7.**

3.5.2 Calculating basic statistical parameters

Since all datasets widths and thicknesses revealed lognormal distributions (see Chapter 5), the dataset variables were transformed to logarithmic values and the simple statistical parameters, mean ($\overline{x}_L$), variance (S_L^2) and standard deviation (S_L) was found using built in

functions in Microsoft Excel™. In order to transform these logarithmic statistical parameters back to arithmetic mean, variance and standard deviation special formulae are used (Wilks, 1995).

Transforming the logarithmic statistical parameters to arithmetic values (Wilks, 1995):

$$\bar{x} = 10^{[\bar{x}_L + \frac{S_L^2}{2}]} \quad \text{(Equation 6)}$$

$$S^2 = (10^{S_L^2} - 1)10^{2S_L + S_L^2} \quad \text{(Equation 7)}$$

$$S = \sqrt{(10^{S_L^2} - 1)10^{2S_L + S_L^2}} \quad \text{(Equation 8)}$$

where $\bar{x}$ is the arithmetic mean, S^2 is the arithmetic variance and S is the arithmetic standard deviation; x_L is the mean of logarithmic x values and S_L^2 is the variance of log x values

3.5.3 Further statistical analysis

Since sandbodies with width = 0 cannot have thickness > 0 and vice versa, an *n*-amount of dummy values {X = 0, Z = 0} were added to the datasets to force the linear regression line through this physical required point. Because of the use of logarithmic values, a dummy close-to-zero value 0.0001 was used in practice, since the numerical value log 0 cannot be calculated. Linear regression is then done on this extended dataset (dataset supplemented with *n*-amount of dummy values) by plotting thickness against width in Microsoft Excel™ and using the trend line function which also provides the coefficient of determination, R^2.

The coefficient of linear correlation between sandbody width and thickness is found by taking the square root of the coefficient of determination (r =$\sqrt{R^2}$).

To test the significance of the coefficient of linear correlation the Fisher t-test was used (Davis, 2002; Nemec, 2005)

Fisher t-test function for significance of linear correlation:

H_0: $\delta_{xy} \leq 0$, none or negative correlation

H1: $\delta_{xy} > 0$, positive correlation

$$t = |\, r_{xy} |\sqrt{\frac{n-2}{1-r_{xy}^2}} \quad \text{(Equation 9)}$$

Degrees of freedom (DF) = n -2

The t-critical (t_α) was found in the standard probability table of t-distribution (Davis, 2002; Nemec, 2005).

For testing significance of observed trends relative to the vertical datum, in section 5.4.5, Spearman's rank-correlations tests were used. All the sandbody cross-sectional dimension values were given value ranks (VR) from smallest to largest and their corresponding heights below datum were given position ranks (PR) from smallest to largest. The Spearman's rank correlation coefficient (r_s) was found by using the equation below (Nemec, 2005).

Spearman's rank-correlation coefficient

$$r_s = 1 - \frac{6\sum_{i=0}^{n} D_i^2}{n(n^2-1)} \qquad \text{(Equation 10)}$$

$D_i = PR_i - VR_i$

4. Sedimentological Analysis

4.1 Facies Analysis

13 facies have been distinguished in the logged outcrop sections. They form the genetically- and spatially-related basic building blocks of 12 facies sub-associations, which are grouped further into 5 major facies associations representing the main depositional palaeoenvironments of the studied stratigraphic succession. For practical reasons, the facies sub-associations and associations are given informative interpretive labels, but their descriptions and interpretations are clearly separated in the text.

A summary review of the sedimentary facies with their brief interpretation is given in **Table 2.1.** Digitalized sedimentological logs of outcrop sections are given in the appendix.

Table 2.1. Sedimentary facies distinguished in the studied stratigraphic succession on the basis of outcrop logs. Facies code after Miall (1978), supplemented for carbonates.

Facies	Structure	Grain size/lithology	Interpretation	Outcrop examples
Gm	Non-graded	Pebble to granule carbonate rip up clasts. Matrix supported in a sandy matrix	Intraformational conglomerate	**Fig. 2.1A**
Sh	Plane-parallel stratification	Medium to fine sand	Plane-bed transport of sand by current in the upper flow regime	**Fig. 2.1B**
St	Trough cross-stratification	Medium to fine sand	Sand transport as short-crested (3D) dunes by current in the upper range of lower flow regime	**Fig. 2.1C**
Sp	Planar tabular cross-stratification	Medium to fine sand	Sand transported as long-crested (2D) dunes by current in the middle range of lower flow regime	**Fig. 2.1.J**
Sr	Current ripple cross-lamination	Fine to very fine sand	Sand transported as asymmetric ripples, occasionally climbing, by current in the lower range of lower flow regime	**Fig. 2.1DEF**
Sw	Wave ripple cross-lamination	Fine to very fine sand	Transport by oscillatory waves with low orbital velocities	**Fig. 2.1GH**
Fl	Plane-parallel lamination	Fine sand to mud	Suspension fall-out of fines. Lamination associated with weak currents of unidirectional or oscillatory origin.	
Sm	Massive (structure-less)	Medium sand to mud	Rapid, non-tractional sediment dumping from current; gravitational collapse; or strong bioturbation	
Lo	Massive, trough cross-stratification, ripple cross lamination, wave ripple cross-lamination	Fine to very coarse carbonates grains with ostracode nuclei	Carbonate ooids formed by carbonate coating of grains in a wave agitated shallow lacustrine settings. May have unidirectional flow structures if eroded and subsequently re-	**Fig. 2.1LM**

			deposited in fluvial channels.	
Ls	Domal stromatolites	Limestone	Stacking of algal mats in a shallow water environment, in the photic zone, distal from siliciclastic input	**Fig. 2.1NO**
Lm	Massive, may have roots	Micritic limestone	Suspension fall out of fines in a quiet lacustrine setting, or if rooted in a lagoonal setting.	
P	Laminated to massive, bio/pedoturbated, reddish brown, with greenish/grey mottles	Mudstone	Palaeosol	**Fig. 2.1K**
Los	Massive, can be bioturbated.	Dolomitic limestone, micritic, grey, dark grey, black or purple, kerogenous. may contain vertebrate and invertebrate fossils	Oil shale. Suspension fall out of fines in an open lacustrine, profundal setting	

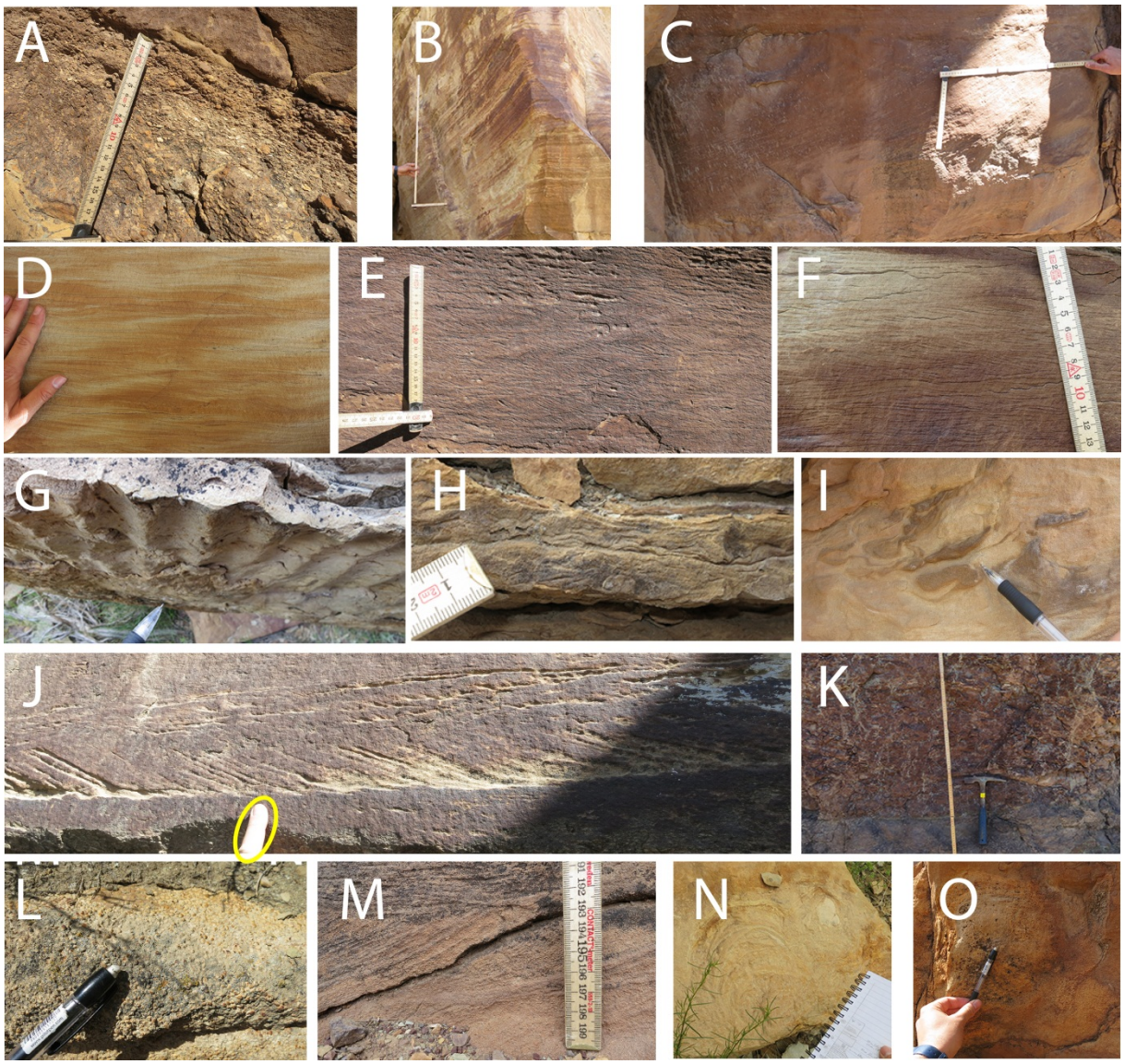

Fig. 2.1. Outcrop images of different facies (**A**) Gm (intraformational conglomerate) (**B**) Sh (plane-parallel stratification) (**C**) St (trough cross-stratification) (**D,E,F**) Sr (current ripple cross-lamination) (**G,H**) Sw (wave ripple cross-lamination) (**I**) soft sediment deformation (**J**) Sp (planar tabular cross-stratification) note finger for scale (**K**) P (palaeosol) (**L,M**) Lo (ooid/ostracode grainstone) (**N,O**) Ls (domal stromatolites)

4.2 Facies Sub-Associations (FsA)

4.2.1 Facies sub-association A: Fluvial lateral-accretion deposits

Description: This sub-association occurs within sandbodies that typically have an erosional base overlain by Gm (intraformational conglomerate). It consists of fine grained sandstone with large scale inclined strata that are commonly heterolithic. There is usually a fining upwards trend within each inclined bed, from fine to medium sandstone at the base to fine/very fine sandstone or siltstone towards the top, although in some cases this trend is not observed (**Fig. 4.2**). Common facies in the lower part are Sh (plane-parallel stratification), St (trough cross-stratification), and Sp (planar tabular cross-stratification). Towards the top Sr (current ripple cross-lamination) becomes more common and Fl (plane-parallel lamination) is in some cases present at the top. Sm (massive) is also common for the sub-association. In cross section the inclined stratification has a sigmoidal geometry, beds dip between 11-25°. Palaeocurrents measured from ripples, St (trough cross-stratification) and sole marks are generally perpendicular to the dip direction of the inclined strata.

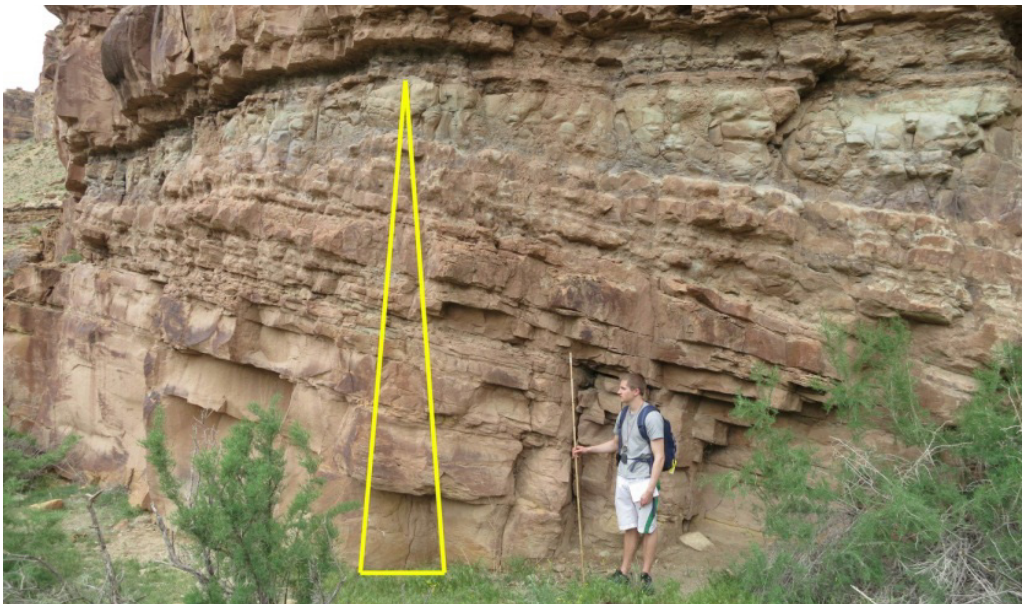

Fig. 4.2 Facies sub-association A: Fluvial lateral accretion deposits. Example from the U8 interval at location of log 1.

Interpretation: The sub-association A is interpreted to have formed as lateral accretion in a fluvial channel, as point bars on the inside of a meander bend, or by lateral accretion on the sides of mid-channel bars. High sinuosity increases the centripetal force, causing water on the outside of a channel bend to flow faster than water on the inside of a bend. This causes

coarser sediments to be deposited in the deeper outer part of the bend and sediments become gradually finer towards the inner bend. The high flow power in the outer bend causes the channel to erode into previous deposits and expand, allowing deposition on the inner bend causing lateral accretion. The deposited sandbodies usually fine upward from a channel floor lag conglomerate to very fine sandstone or siltstone at top. The structures generally show a reduction in flow power from base to top. Starting with Sh (plane-parallel stratification) deposited in the upper flow regime near the erosive base surface passing into St (trough cross-stratification) and Sp (planar tabular cross-stratification) facies, and further upwards into Sr (current ripple cross-lamination) facies when the flow power is either too weak or the water depth to shallow to develop dunes.

4.2.2 Facies sub-association B: Channel-bank collapse deposits

Description: FsA-B is composed of steeply inclined heterolithic bedding. Because of inaccessibility there are no logged sections of FsA-B. In the Virtual Outcrop a ~50 m wide and ~8 m thick package of FsA-B is found where it sharply overlies a lense shaped sandbody of FA-F (fluvial) that is incised into deposits of FA-LS (lacustrine shoreface)(**Fig. 4.3**). The dip of the inclined bedding is measured on to Virtual Outcrop to 30°. The inclined strata shows a coarsening lateral trend towards the right in **Fig. 4.3.**

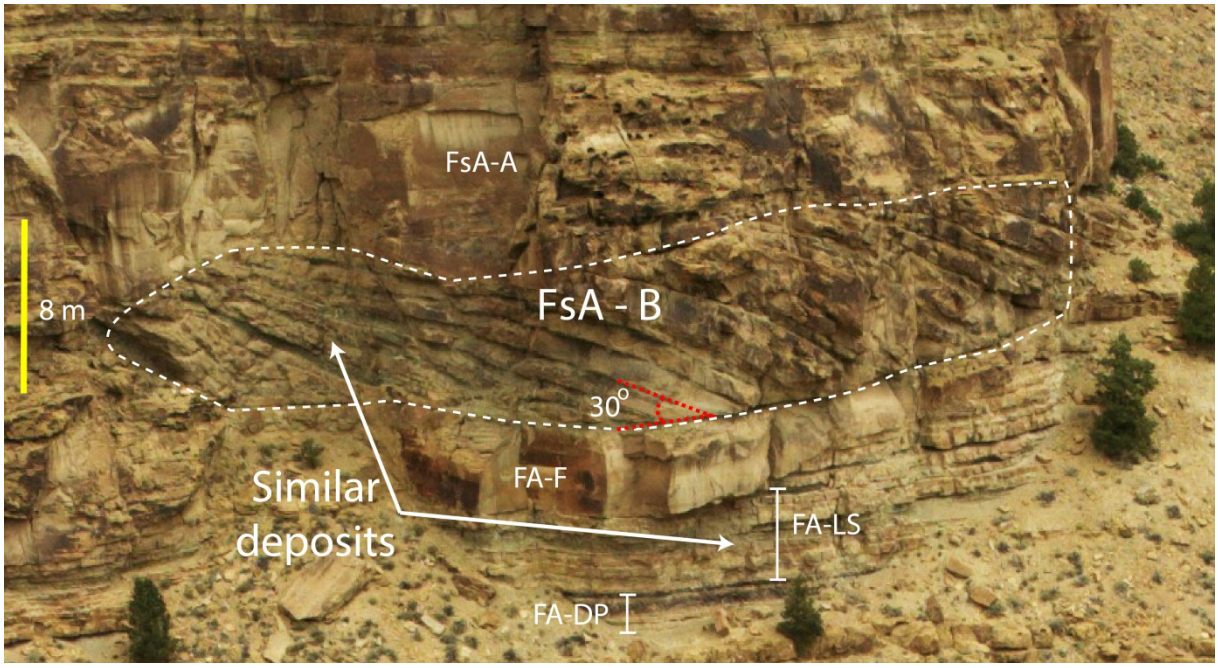

Fig. 4.3. FsA-B overlying an erosive lens of FA-F (fluvial) and FA-LS (lacustrine shoreface). The example is located in the U10 interval, between Blind Canyon and Daddy Canyon. View is toward the north.

Interpretation: The deposits of FsA-B are interpreted to be deposited by gravitational collapses of channel-banks caused by undercutting. The example above has been interpreted in the following way: a deeply incised channel formed due to lake level fall (**Fig. 4.4B**). The steep cut-bank collapsed, half-plugging the channel with a slide body of pre-existing heterolithic deposits (**Fig. 4.4C**). The high coherence of these deposits preserved the parallel bedding with only minor deformation (Nemec, 1990). The coarsening lateral trend inside the slide deposit body, towards the right in **Fig. 4.4A,** reflects the coarsening upwards trend of the incised deposits. Lastly the river scoured its way through the slide deposits while it considerably widened its channel due to the deficit of vertical accommodation space. The river was thereby forced to use lateral accommodation for sediment deposition by lateral accretion and it acquired a meandering channel pattern (**Fig. 4.4D**). The facies sub-association B, at the scale shown in example above, has as far as the present author is aware of not previously been described in the Sunnyside Delta interval.

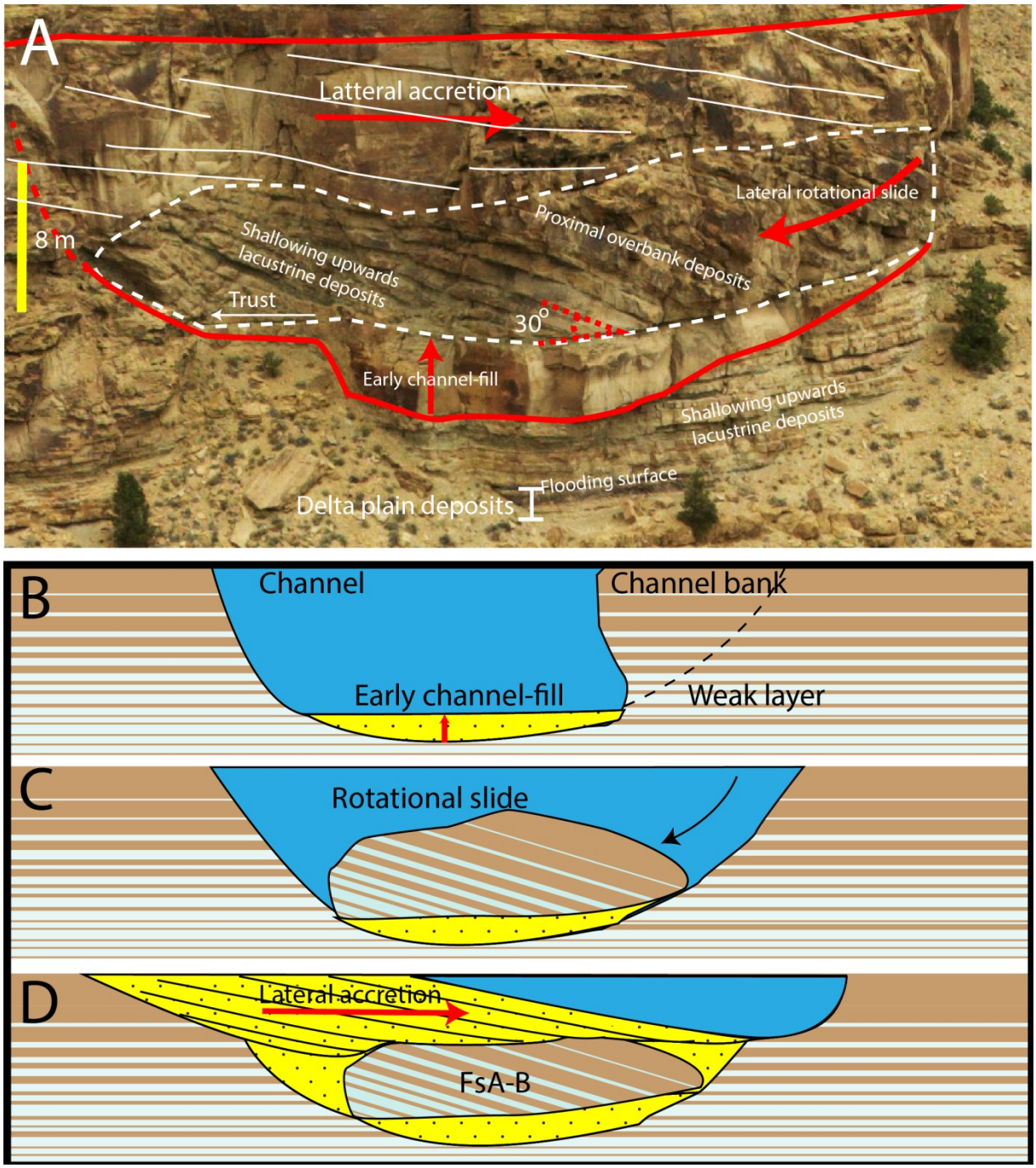

Fig. 4.4. Interpretation of deposition of FsA-B in the U10 interval between Blind and Daddy Canyon. (**B, C, D**) Generalized interpretation for the formation of the FsA-B observed in **Fig. 4.3** (**B**) Channel-bank undercutting (**C**) Gravitational collapse of channel-bank (**D**) stage of channel fill by lateral accretion.

4.2.3 Facies sub-association C: Downstream-accretion deposits

Description: FsA-C (downstream accretion) occurs within FA-F (fluvial channel-belt system). In contrast to the FsA-A (lateral accretion) were palaeocurrents are ~perpendicular to inclined stratification, the palaeocurrents in FsA-C are sub-parallel to the dip direction of the bedding. They are composed of mainly St (trough cross-stratification) and Sm (massive).

Interpretation: FsA-C is interpreted as downstream accretion deposits, deposited on the downstream side of meander-bends or on downstream side of a mid-channel bar in channel-sections with some degree of braiding (Bridge, 2003)

4.2.4 Facies sub-association D: Abandonment plug deposits

Description: Channelized incision containing facies Fl (plane-parallel lamination) often interbedded with thin subhorizontal sandstone beds onlapping incised FA-F (fluvial channel-belt system) (**Fig. 4.6**). Containing laminated mudstone and laminated siltstone interbedded with very fine sandstone beds. Widths commonly range between 40-100 m (**Fig. 4.5A**) and the most common thicknesses 5-7 m (**Fig. 4.5B**).

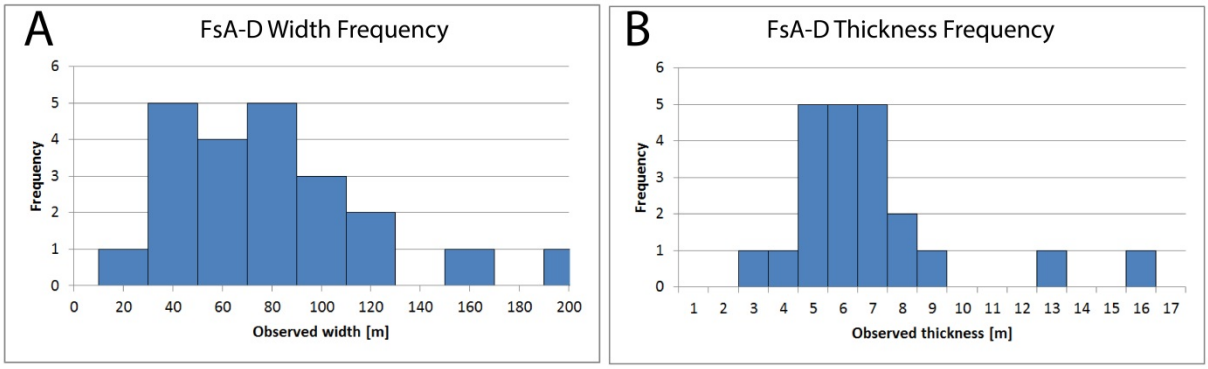

Fig. 4.5. Frequency histograms showing observed width (**A**) and thickness (**B**) of the concave upwards shaped FsA-D.

Fig. 4.6. Facies sub-association D: Abandonment plug. Located in the U6 interval near the rest stop in Daddy Canyon.

Interpretation: The sub-association D is interpreted to be abandonment plug deposits. Deposited in a fluvial channel when avulsion has occurred further upstream and abandoned the previous channel or when a meander bend was abandoned by chute or neck cut off. The abandoned fluvial channel became an oxbow lake that eventually filled up by vertical accretion of fine grained flood derived sediments. The heterogeneity of the abandonment plug depends on the type and rate of which the channel segment has been abandoned.

Depending on the angle between the newly cut channel and the abandoned channel, bed load sediments may continue to be deposited in the abandoned channel, mostly in the part in proximity to the cut-off (Bridge, 2003). The thickness and width of abandonment fills may be used to find the depth and width of the palaeochannel (Bridge, 2003).

4.2.5 Facies sub-association E: Undifferentiated overbank sandbodies

Description: Sandbodies typically < 2 m thick, both channelized and non-channelized, lenticular, tabular or wedge-shaped, consists mostly of very fine sandstone with unidirectional flow structures. In most cases interbedded with FsA-F (palaeosol) (**Fig. 4.7**). Laterally they pass into FA-F (fluvial channel-belt system) in one direction and pinches out into FsA-F (palaeosol) in the other, with the coarsest grain sizes present proximal to FA-F (fluvial channel-belt system) and gradually fines away from FA-F (fluvial channel-belt system). Sr (current ripple cross-lamination) is commonly observed often climbing, Sh (plane-parallel stratification) and Sm (massive). Commonly non-graded or slightly normal graded.

Fig. 4.7. FsA-E (overbank sandbodies) interbedded with the reddish FsA-F (palaeosols)

Interpretation: Overbank sandbodies deposited in crevasse splays, crevasse channels or levee sandsheets. As channels overflow their banks the flows rapidly decelerate and deposit the coarsest grains closest to the channel margin, finer grains are transported further into

the floodplain. The overflow may be as a sheetflow depositing a wedgeshaped levee sandsheet, or, if the levees gave way, as a crevasse channel feeding sediment from the channel onto the floodplain and depositing it in a crevasse splay. Where overbank sediments build out into small standing bodies of water on the floodplain small mini-deltas may occur depositing small coarsening upwards packages.

4.2.6 Facies sub-association F: Palaeosol

Description: Reddish/brown/purple to mottled grey/green. Internal colour variations are often changing from the dark colours to the lighter colours when the sub-facies is in contact with a sandbody. It consists of laminated mudstone and siltstone and is commonly bioturbated and rooted. Roots are commonly encrusted with calcium carbonate and calcrete nodules are common (**Fig. 4.8B**). The thickness of these deposits range between ~10cm to ~150cm, and they are very laterally extensive unless cut into by FA-F (fluvial channel-belt system). They are easily eroded and therefore often only the top of the FsA-F is found where it underlies more resistant sandstones. Desiccation cracks are observed at a few locations, although not common in the studied stratigraphic interval (**Fig. 4.8C**).

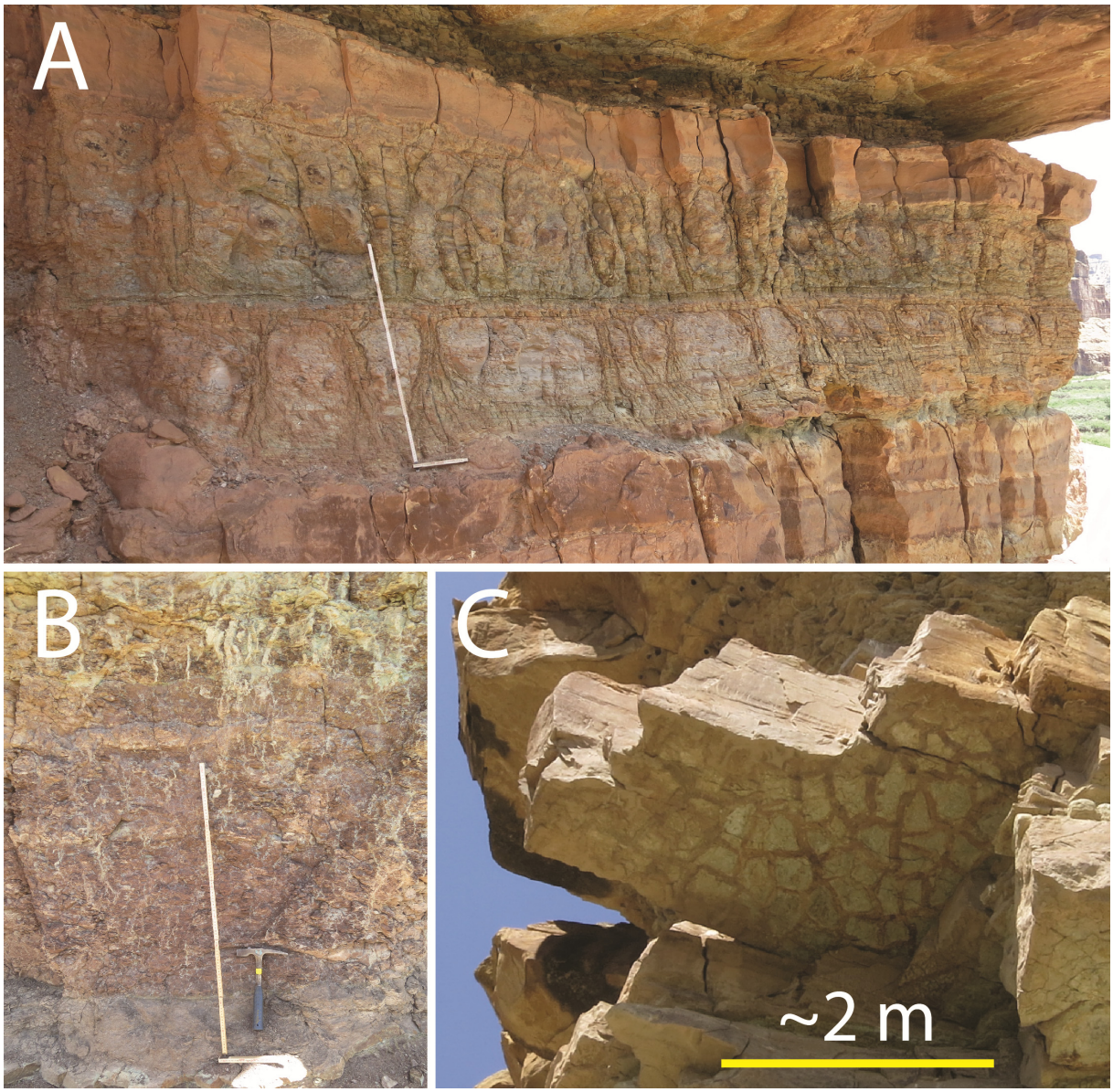

Fig. 4.8. Facies sub-association F (palaeosol) **(A)** Two horizons with rooted palaeosol. Measuring stick is 1 m (**B**) Palaeosol with roots encrusted with calcium carbonate. Measuring stick is 1 m (**C**) Desiccation cracks preserved in sandstone above FsA-F (palaeosol)

Interpretation: The sub-association F is interpreted based on colour and pedoturbation to be palaeosol deposits. Deposited as soils on a floodplain, and commonly rooted. Reddish colour of the soils is caused by oxidation of iron minerals. The prominent reddish colour of the palaeosols in the interval is attributed high temperatures during deposition, enhancing the weathering reaction rate, enhancing the decay of organic water which decreases the acidity and the reducing potential of the pore water (Reading, 1996). Areas in contact with sandbodies may be mottled grey/green most likely due to leaching by reducing groundwater

flowing through permeable sandbodies during shallow burial (Keighley et al., 2002). Areas around roots may also be mottled grey/green because of biological leaching. The vertical veined calcretions are caliche, precipitation of calcium carbonate around plant roots, common in semi-arid environments where high evaporation at the surface sucks water up by capillary forces and leaves the calcium carbonate. The red colouration, desiccation cracks and presence of calcretes suggests an arid to semi-arid climate.

4.2.7 Facies sub-association G: Mouthbars with tabular clinoforms

Description: Tabular sandbodies that are composed of very fine to fine grained sandstone. Each individual sandbody is typically non-graded or normal graded, but the sandbodies stack forming coarsening upwards packages. The sandbodies are rhythmically interbedded with FsA-K (lacustrine mudstone) (**Fig. 4.9A**) or amalgamated. They generally have a tanner colour than sandbodies within FA-F (fluvial channel-belt system). The tabular bedding is gently dipping ~2°. Measured palaeocurrents are ~parallel to the bedding dip direction. St (trough cross-stratification), Sr (current ripple cross-lamination), Sw (wave ripple cross-lamination), Sh (plane-parallel stratification), Sm (massive) and soft sediment deformation are common. In some examples the base of the facies sub-association is injected by green siltstone of FsA-K (lacustrine mudstones) (**Fig. 4.12**). FsA-G commonly overlies FsA-I (high energy carbonates) and are overlain by sandbodies of FA-F (fluvial channel-belt system). An uncommon relationship is found in U6 where FsA-G directly overlies FsA-A (fluvial lateral accretion) (**Fig. 4.9B**)

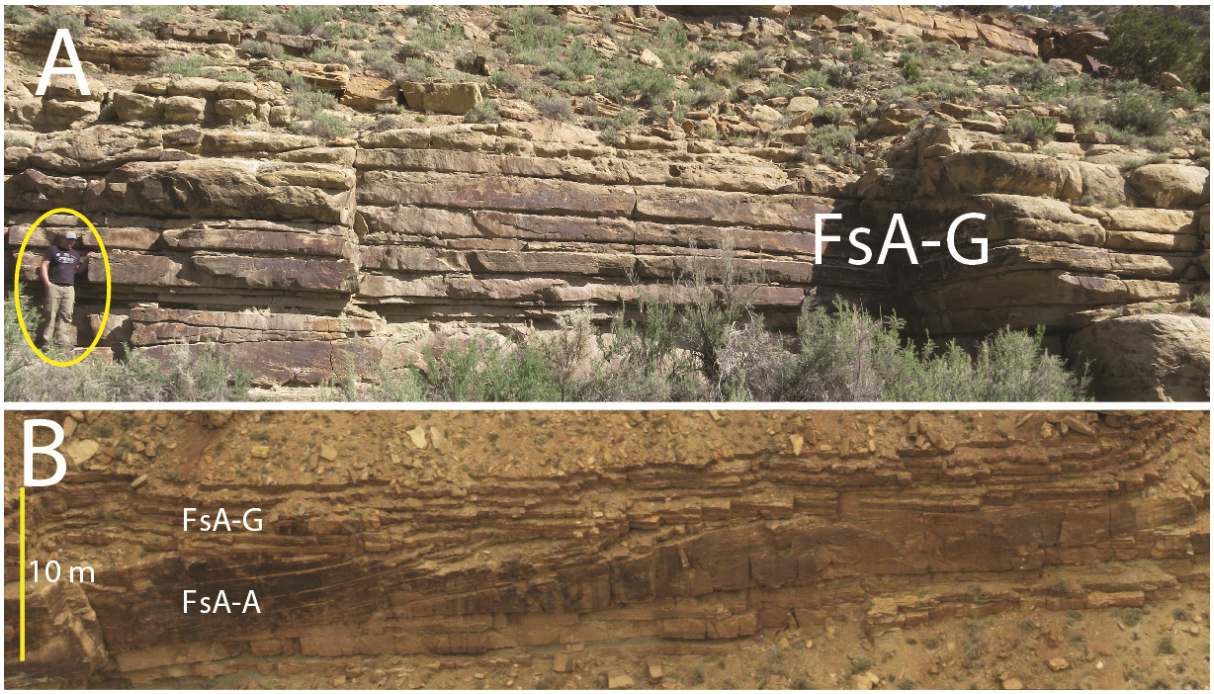

Fig. 4.9. Facies sub-association G (tabular mouthbars) (**A**) Picture of FsA-G (tabular mouthbars) from Argyle Canyon. Note person in the left of the picture for scale. (**B**) The uncommon relationship between FsA-G (tabular mouthbars) and FsA-A (fluvial lateral accretion), where FsA-G (tabular mouthbars) conformably overlies FsA-A (fluvial lateral accretion). Example from U6 between Gate Canyon and Blind Canyon.

Interpretation: These are interpreted as mouthbar deposits. Flow velocities rapidly decrease when a channelized flow meets a standing body of water and deposits its sediment load as hyperpycnal density currents producing subaqueous sandsheets. The normal grading of each individual bed reflects a waning flow.

4.2.8 Facies sub-association H: Mouthbars with sigmoidal clinoforms

Description: Inclined heterolithic clinoforms with a sigmoidal geometry. Each individual inclined bed fines laterally from fine grained sandstone to siltstone at the toe of the clinothem. The clinothems form coarsening upwards packages. Laterally FsA-H thins and is found onlapping another similar sandbody. This sub association may be hard to distinguish from FsA-A (fluvial lateral accretion) and B (steep fluvial lateral accretion) in areas of poor exposure. Clinoforms of the FsA are observed dipping towards the south in location near the Cottonwood Canyon on the U8 interval (**Fig. 4.10**).

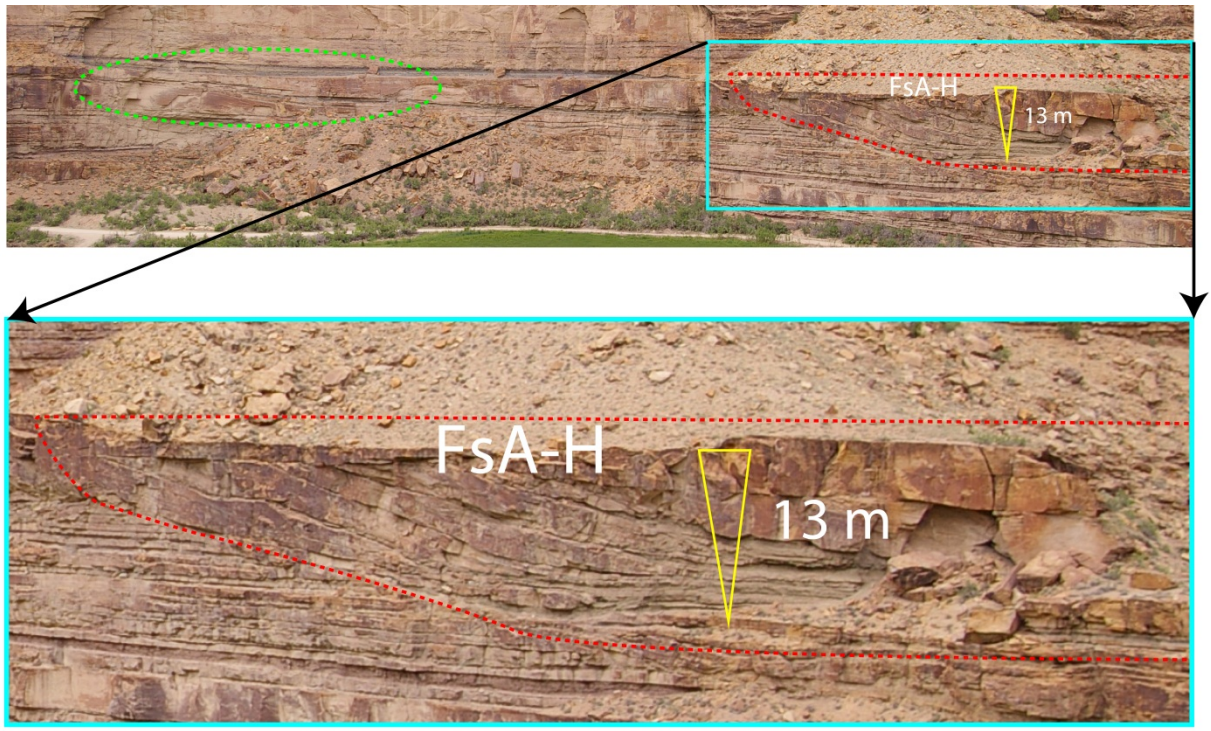

Fig. 4.10. Facies sub-association H: Clinoform mouthbars (inside red stippled line). In the U8 ~1.5 km east of Cottonwood Canyon. Note onlaping sandbody relationship inside area of green stippled line.

Interpretation: Sharp based mouthbars, deposited by hyperpycnal flows formed when dense sediment loaded river discharge enters the less dense waters of Lake Uinta. During flow events combined with limited accommodation the hyperpycnal flow scours the substrate in areas proximal to the river mouth. As the flow wanes it goes from erosional to depositional and deltaic beds are deposited into the scour (Fielding et al., 2005; Schomacker et al., 2010). The lateral onlaping (**Fig. 4.10**, green stippled area) onto similar sandbodies is interpreted to be formed by compensational stacking of mouthbar lobes. The dip direction of the clinoforms indicates the palaeocurrent of the mouthbars. The observed direction in **Fig.4.10**, towards the south, is in the opposite direction of the mean palaeocurrent (see section 5.3), and is therefore evidence pointing towards deposition in a fluvial dominated delta with a "bird foot" morphology.

4.2.9 Facies sub-association I: High-energy carbonates

Description: Tabular, very extensive limestones. ~20 cm to ~1.5 m thick. Weathered orange/yellow. Consists mainly of facies Lo (ooid/ostracode grainstone). Shell fragments, fish shales (**Fig. 4.11**), fish teeth are also observed. Other workers have recognized Coquina,

gastropods, bivalves, ostracodes, algal hashs and ostracode hashs (Keighley et al., 2003). Beds commonly extend throughout the entire study area, but may be locally eroded away by overlying sandbodies. Sandbodies eroding into the FsA-I (high energy carbonates) commonly contain ooids eroded from below. Structures observed in the ooidal limestones are Sw (wave ripple cross-lamination), St (trough cross-stratification) and Sm (massive). Where FsA-I (high energy carbonates) overlies sandstones burrows filled with oolithic content have commonly been observed (**Fig. 4.11**).

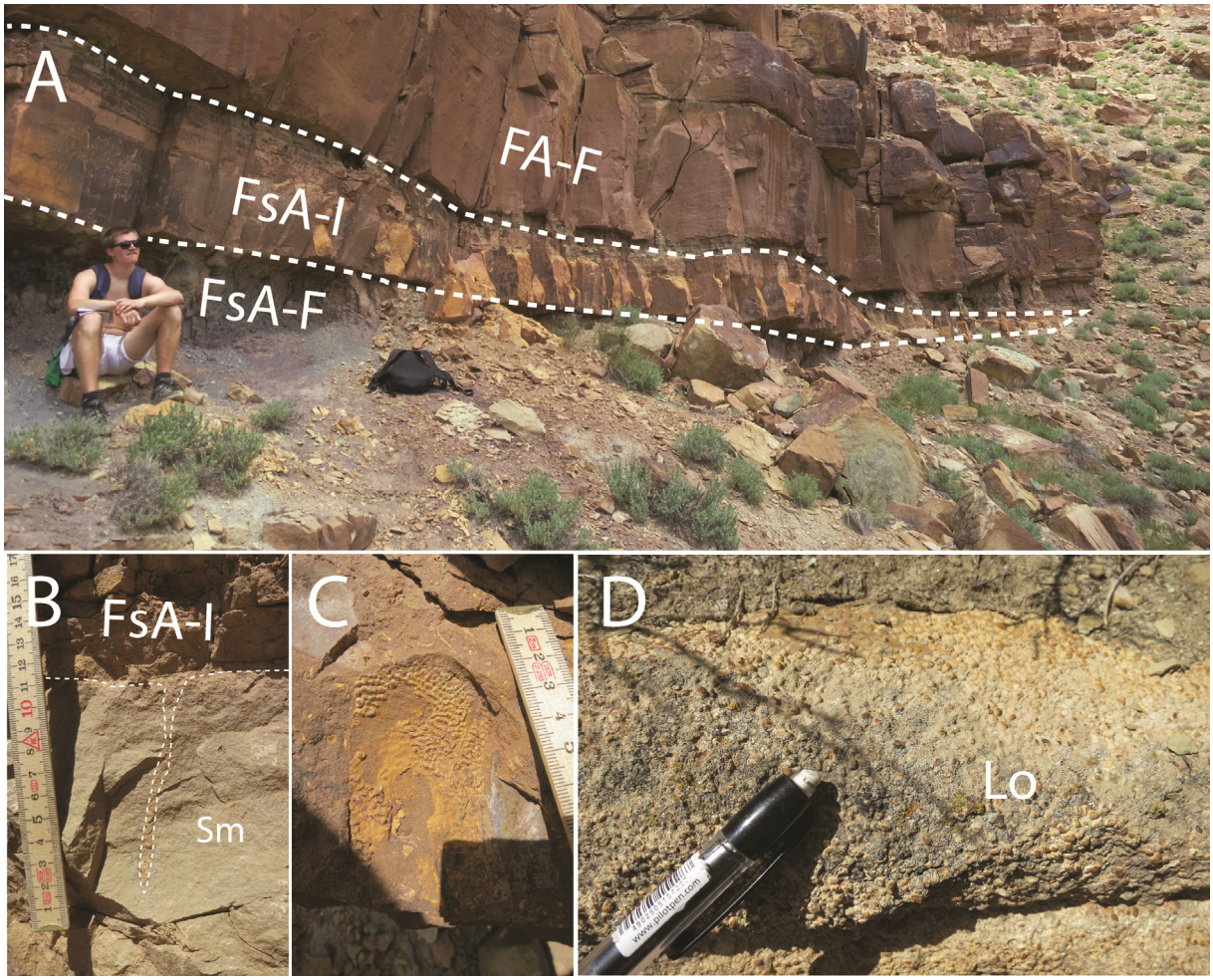

Fig. 4.11. (**A**) Laterally extensive tabular bed of FsA-I (high energy carbonates), weathered yellow/orange (**B**) sandstone with burrow filled with ooids from FsA-I layer above ***C)*** fish scales inside FsA-I (**D**) Oolite grainstone with ostracode nuclei inside FsA-I

Interpretation: Ooids form in very shallow waters saturated with $CaCO_3$, they start as small ostracode grains that are swashed back and forth by wave actions, gradually growing in size

by aggrading layers of CaCO3 (Reading, 1996). The facies sub-association I is therefore interpreted to be deposited in high energy shoals, bars, beaches and shorefaces, primarily deposited by wave energy. In places where they have been later incised by fluvial channels, unconsolidated grains have been incorporated in the flows and re-deposited by unidirectional currents.

4.2.10 Facies sub-association J: Low-energy carbonates

Description: Laterally continuous limestone beds. Weathered orange/yellow. Composed of facies Lm (micritic limestone) and Ls (domal stromatolites). Laminated or massive. In some places rootlets are observed within the facies Lm (micritic limestone).

Interpretation: Deposits from low energy carbonate environments, distal from siliciclastic input. Most likely intershoals and interdistributary. Where there are made observations of rootlets the FsA-J is most likely deposited in a lagoonal setting or in ponds on a floodplain or lacustrine mud flats.

4.2.11 Facies sub-association K: Lacustrine mudstones

Description: Greenish/grey fine grained deposits. Facies Fl (plane-parallel lamination). In a few places found injected into above sandbodies of FA-MB (**Fig. 4.12**).

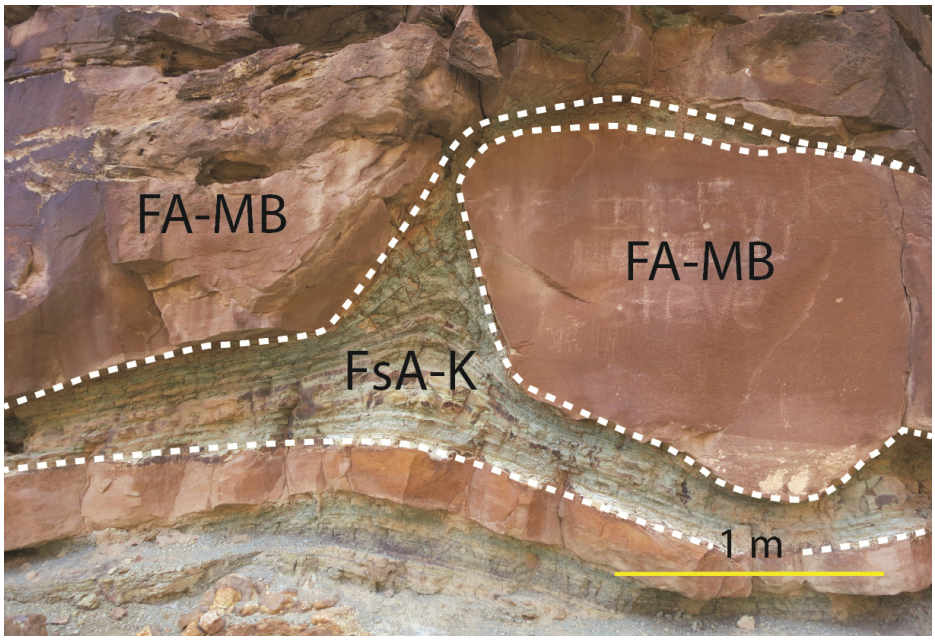

Fig. 4.12 FsA-K (lacustrine mudstone) injected into base of a FA-MB (mouthbar) sandbody in the U3 interval in Blind Canyon

Interpretation: Suspension fall-out of fines in a low energy lacustrine environment. If the sediment is rapidly deposited on top of FsA-K pressures may build up if the pore water cannot escape. Eventually this can cause the sub-facies association to inject up into above deposits as seen in **Fig. 4.12**.

4.2.12 Facies sub-association L: Shallow lacustrine sandsheets

Description: Tabular sandbodies of very fine sandstone, 10–50 cm thick. Tan in colour. Commonly interbedded with FsA- I, J and K. Often forming coarsening-upwards packages.

Interpretation: Siliciclastic shoreface deposits extended lakewards by storm waves and minor lake-level fluctuations.

4.3 Facies Associations (FA)

The facies and facies sub associations described above have been grouped into facies associations, summarised in **Table 4.2**. Percentage of each facies association is measured at various vertical sections along the Virtual Outcrop.

Table 4.2. Summary of facies associations and their component sub-associations in the Sunnyside Delta interval. The distribution of facies associations are given in a per cent range, based on measured vertical sections at various locations on the Virtual Outcrop.

Facies association		Component sub-associations	% of study interval
FA-F	Fluvial channel-belt system	FsA - A, B, C, D	35-70%
FA-DP	Alluvial delta plain system	FsA - E, F	10-40%
FA-MB	Deltaic mouthbar system	FsA - G, H	7-14%
FA-LS	Lacustrine shoreface system	FsA - I, J, K, L	15-20%
FA-OL	Open-water lacustrine system		< 0.05%

4.3.1 Facies association F: Fluvial channel-belt system

Description: Compromises 35-70% of the study interval, lowest percentage in the west and higher eastwards. FA-F commonly forms elongated sandbodies that may have many internal erosion surfaces. This facies is primarily comprised of facies FsA-A (lateral accretion), FsA-C (downstream accretion) is less common. The facies association also includes FsA-B (channel-

bank collapse) and FsA-D (abandonment plugs). Commonly erodes into FA-DP (delta plain) laterally.

Interpretation: The FA-F is interpreted to be channel-belt deposits deposited by predominantly meandering fluvial channels with some component of local braiding (Bridge, 2003; Reading, 1996; Ryder et al., 1976). The facies association includes both terminal distributary channels and delta plain fluvial channels.

4.3.2 Facies association DP: Alluvial delta plain system

Description: Compromises 10-40% of the study interval, highest in the west and lower eastwards. The facies sub-association E (overbank sandbodies) and F (palaeosols) are commonly found as interbedded packages which are up to 16 m thick (**Fig. 4.7**) and pass laterally into FA-F (fluvial).

Interpretation: The FA-DP is interpreted to be deposited on an alluvial delta plain system as overbank mudstones and unconfined sheet sands (Bridge, 2003; Reading, 1996). The red colouration and presence of calcrete nodules support an arid to semi-arid environment.

4.3.3 Facies association MB: Deltaic mouthbar system

Description: Compromises 7-14% of the study interval. The facies sub-associations FsA-G (tabular mouthbars) and FsA-H (sigmoidal mouthbars) may form very laterally continuous sandbodies, up to ~5700 m wide. They have less variation in thickness than the fluvial sandbodies (FA-F), do not erode into delta plain deposits of FA-DP, and commonly overlie lacustrine shoreface deposits (FA-LS). Uncommon examples of tabular mouthbars (FsA-G) conformably overlying fluvial deposits (FA-F) are found in the U6 interval.

Interpretation: Mouthbars deposits in a delta front system laid down where sediment loaded streams decelerates when entering a standing body of water in the lake. The presence of facies Sw (wave ripple cross-lamination) is evidence that they were later subjected to some degree of wave reworking. Because of density differences between the fluvial streams and the lacustrine water, hyperpycnal flows develop and may have scoured the substrate accounting for the sharp based nature of some of these deposits (Schomacker et al., 2010).

4.3.4 Facies association LS: Lacustrine shoreface system

Description: Compromises 15-20% of the study interval. Facies association LH is made up by interbedded deposits of high energy carbonates (FsA-I), low energy carbonate (FsA-J), lacustrine mudstones (FsA-K) and shallow lacustrine sandsheets (FsA-L). The facies association is more tan and pale in colour than the FA-DP (delta plain) deposits. The usually underlie mouthbar sandbodies (FA-MB).

Interpretation: The facies association LS is interpreted to be deposited in shallow lacustrine environments; pro-delta, interdistributary bays, and shoals at or close to the shoreline of a shallow lake.

4.3.5 Facies association OL: Open-water lacustrine system

Description: Compromises <0.05% of the study interval. Composed of facies Los (lacustrine oil shale). Only observed in one location underlying the M9 carbonate marker.

Interpretation: Deposited in an offshore profundal setting by suspension fallout of fines. The FA-OL is the most distal facies observed in the studied interval and is deposited on the study area during periods of maximum extent of the Lake Uinta, thereby marking maximum flooding surfaces (Keighley et al., 2003).

4.4 Depositional Model

Based on the above facies analyses together with available literature on the Sunnyside Delta interval, the succession is interpreted to be deposited in a semi-arid fluvial dominated deltaic depositional environment, subjected to a high degree of shoreline fluctuation. **Fig. 4.13** is an illustration of how the depositional environment is envisaged. The figure illustrates both deposition during delta regression (east) and during transgression (west), and how the two delta states might coincide at the same time with changing sediment supply caused by avulsions upstream.

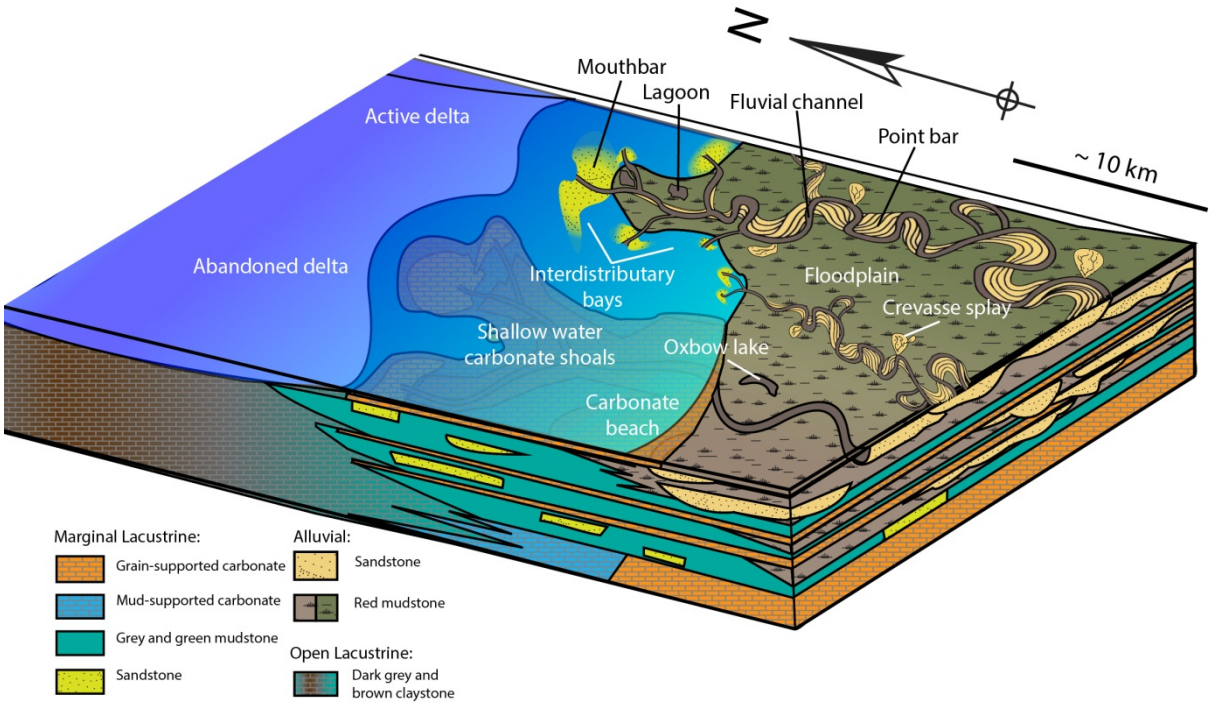

Fig. 4.13. Depositional model for the Sunnyside delta interval. Showing an abandoned delta to the west and an active delta to the east. Note the dimensions of architectural elements are not to scale.

4.5 Modern Analogue: the Omo River Delta, Kenya

A potential modern analogue for the palaeo Sunnyside Delta is the Omo River Delta. It is located on the northern shore of the internally draining Lake Turkana, in the northern Kenyan rift. It is Africa's fourth largest lake and the largest arid lake in the world. The lake contains 3.5 km of lacustrine sediments deposited during the last 4.3 Ma (Johnson and Malala, 2009). From 1973 – 1989 a 6 m fall in lake level was recorded and is attributed increased aridity and a decrease in precipitation (**Fig. 4.15**) (Haack, 1996), causing the delta to prograde by ~20 km from 1973 to today. The available historical imagery provided by

Google Earth™ gives a unique insight in the flooding and subsequent progradation of the Omo River Delta (**Fig. 4.14**).

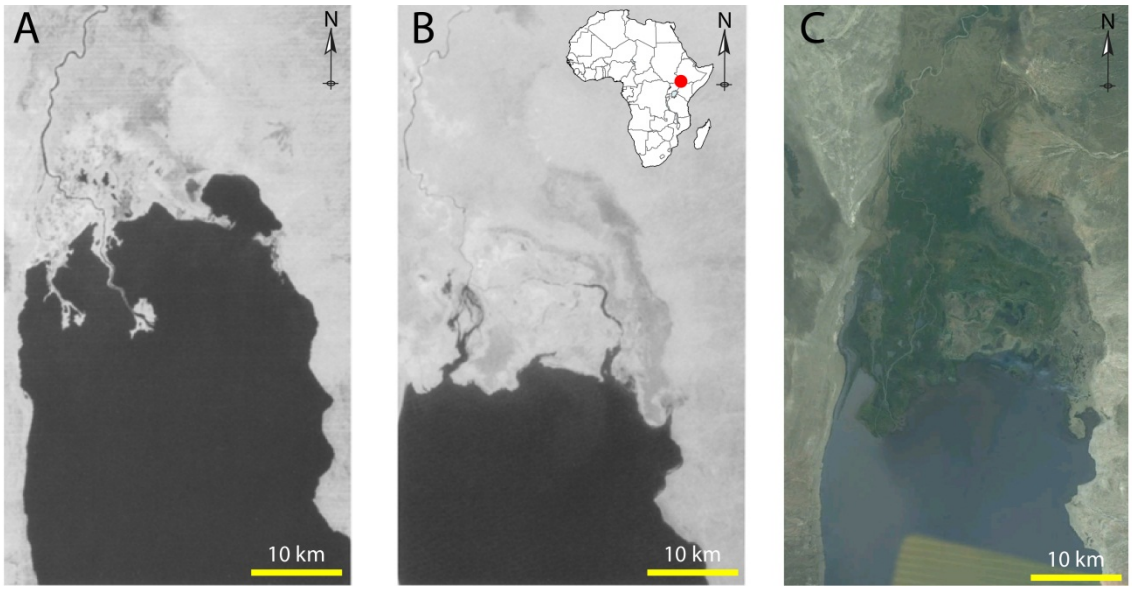

Fig. 4.14. The Omo River Delta on the Ethiopian-Kenyan border in (**A**) 1973 (**B**) 1989 (**C**) 2013. Location shown with red dot on embedded map of Africa. Modified from Haack (1996).

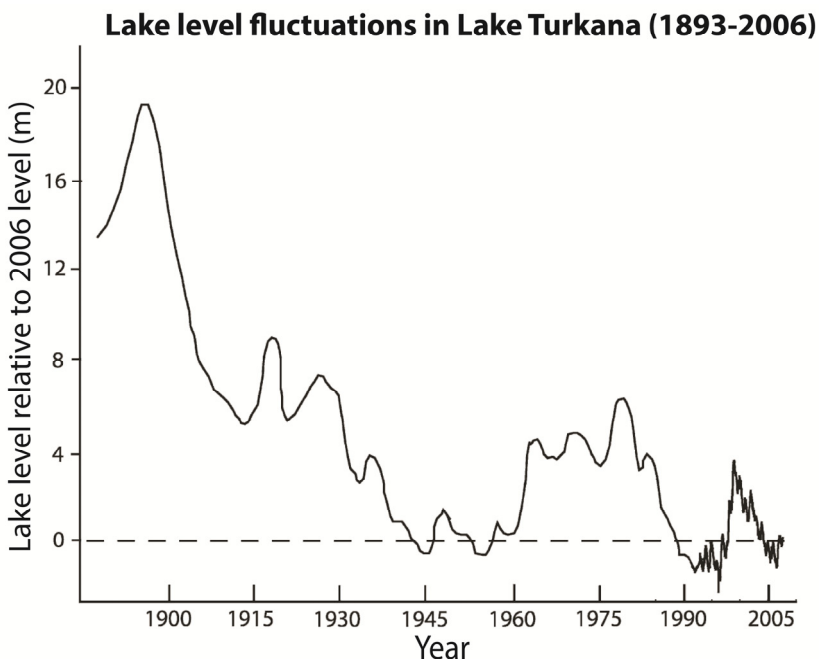

Fig. 4.15. Lake level fluctuations (in metres relative to the 2006 lake level) in the internally draining Lake Turkana in the northern Kenyan rift, in the period 1893 - 2006. Slightly modified from Johnson and Malala (2009)

The major difference between the Lake Turkana and the palaeo-lake Uinta is the basin type. The Omo River Delta is confined to a relatively narrow rift valley, while the Sunnyside Delta was most likely less confined. In spite of this difference there are still fundamental similarities between the two; they both build out into large internally draining lakes with gentle gradients, are located in arid to semi-arid climates and are subjected to high fluctuations in lake levels. This allows observations to be taken from the Omo River Delta as input for creating a depositional model for the Sunnyside Delta interval. A key observation is that even in a large lake that has winds labeled by Johnson and Malala (2009) as "unforgettable" (gusting over 110 km/h), there is a coexistence of both the fluvial dominated Omo River Delta and the wave dominated Turkwel River Delta (**Fig. 4.16**). This may be attributed two main factors; (1) the waves being attenuated when interacting with the shallow lake bed in the northern part of the lake, (2) the shallow water allowing the Omo River Delta to prograde into the lake at a faster rate than the basin processes can redistribute it. A similar coexisting relationship is described from the Green River formation in Uinta Basin by Taylor and Ritts (2004) who described a wave-dominated facies near Raven Ridge on the north-eastern margin of the palaeo-Lake Uinta, where the lake had a steeper depositional gradient than it had on the southern margin where the Sunnyside Delta was deposited.

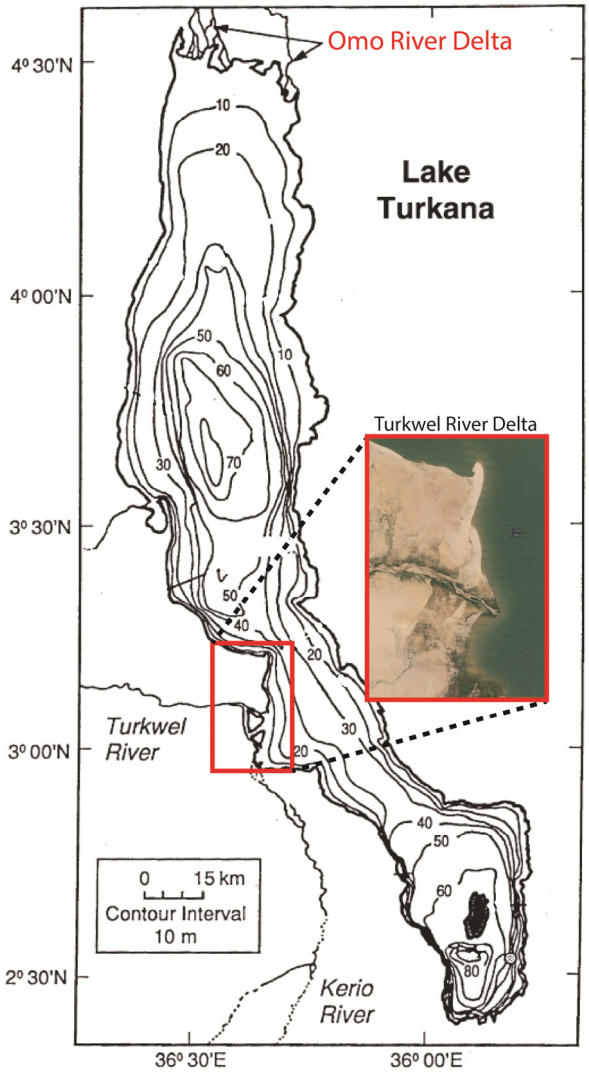

Fig. 4.16. Bathymetric map of Lake Turkana. The Omo River Delta is located in the northern part of the lake, building out onto a gentle gradient. The more wave dominated Turkwei River Delta is building out into a part of the Lake Turkana with a steep depositional gradient. Modified from Johnson and Malala (2009)

5. Sandbody Geometry

5.1 Previous Research

Fluvial channels migrate across floodplains depositing sediments on either the channel margins; by lateral accretion of point bars, or within the channel; by downstream and/or lateral accretion of mid channel bars. As the channels migrate the different bar-forms merge to create channel-belts. The channel-belts are typically quite straight and represent all the deposits within a channel between avulsion events (Bridge, 2003). Williams (1986) gathered empirical data from all published data on modern meandering rivers, and derived equations to estimate fluvial parameters from bankfull channel depth or channel-belt thickness (**Table 5.1**).

Table 5.1. Empirical equations for characteristics of meandering-river channel-belts. Formulae (1)-(6) from (Williams, 1986), formula (7) from (Collinson, 1978). Slightly modified. All correlation coefficients are significant within a confidence level of 99.95%

Reference number	Equation	Units	Standard deviation of residuals, in per cent		Correlation coefficient
			+	–	
[1]	$L_m = 240\ D^{1.52}$	m	142	59	0.86
[2]	$L_b = 160\ D^{1.52}$	m	128	56	0.90
[3]	$W_c = 0.23\ L_b^{0.89}$	m	56	36	0.97
[4]	$W_m = 148\ D^{1.52}$	m	115	53	0.90
[5]	$R_b = 42\ D^{1.52}$	m	165	62	0.90
[6]	$S = 5.26\ D^{0.68}\ W_c^{-0.4}$	m	73	42	0.86
[7]	$Q = 0.00014\ W_m^{2.13}$	ft, sec	35	30	0.95

Parameter symbols:

D = mean bankfull channel depth
L_m = meander wavelength
L_b = along-channel bend length
Q = mean annual discharge
R_b = channel-bend radius of curvature
S = channel sinuosity
W_c = mean bankfull channel width
W_m = meander-belt width

There are high degrees of spread in collected data on fluvial dimensions. This is attributed the varied stages of development of the measured fluvial system. Generally meandering rivers initially expand transversely (**Fig. 5.1A**), increasing the channel curvature and increasing the channel-belt width (Ghinassi et al., 2014). At a certain time in the channel-belts evolution, related to channel depth and discharge, the transverse expansion decreases and longitudinal expansion dominates (**Fig. 5.1B**). The meander-belt width/thickness ratio thus depends on the maturity of its meander-bends. Similarly for ancient channel-belts the

width/thickness ratio is connected with the maturity of the channel-belts which is controlled by the time available between channel avulsions.

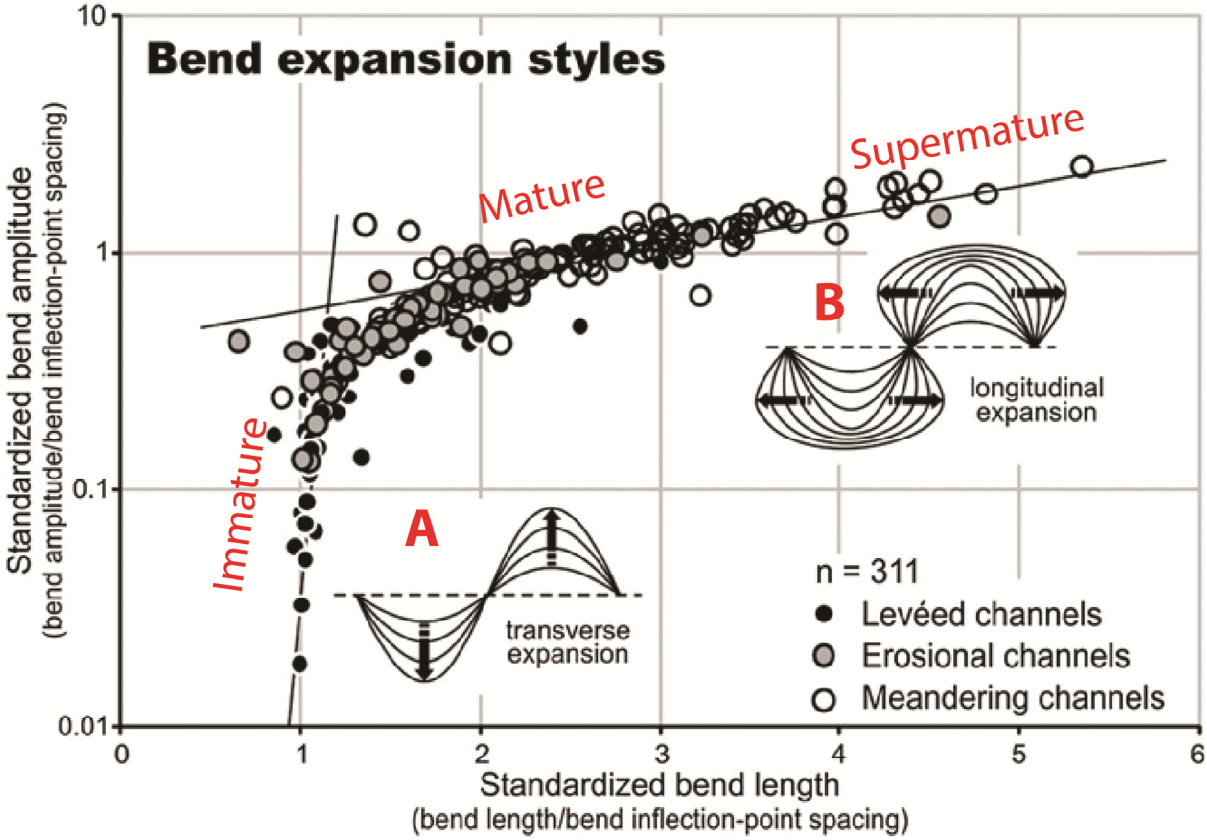

Fig. 5.1. Scatter plot of bend length vs. bend amplitude of meandering channels, revealing two distinctly different bend expansion styles. (**A**) Dominantly transverse expansion. (**B**) Dominantly longitudal expansion. Slightly modified from Janocko et al. (2013). The dataset is from submarine channels, but consistent with observations from fluvial channel-belts (Ghinassi et al., 2014).

Fielding (1987) compiled channel-belt width and thickness dimensions from 45 different sources. They observed big variations in the width/thickness ratio when comparing channel-belts deposited by channels with different morphology (**Fig. 5.2**). Although their dataset of channel-belts dimensions plotted in **Fig. 5.2** are objectively measured, their corresponding trendlines are questionable. None of them show trends towards the physically required point of width = 0 and thickness = 0. Instead the trendlines are converging, which is most likely attributed under sampling of the true population of channel-belts dimensions. The choice of hyperbolic (power law) trendline functions are also questionable. Similar work on modern channel-belt width/thickness ratios has been done by Collinson (1977), Davies et al.

(1993) and Lorenz et al. (1985) and for mouthbars Tye (2004). The resulting width/thickness ratio data has a high amount of spread and therefore high standard deviations.

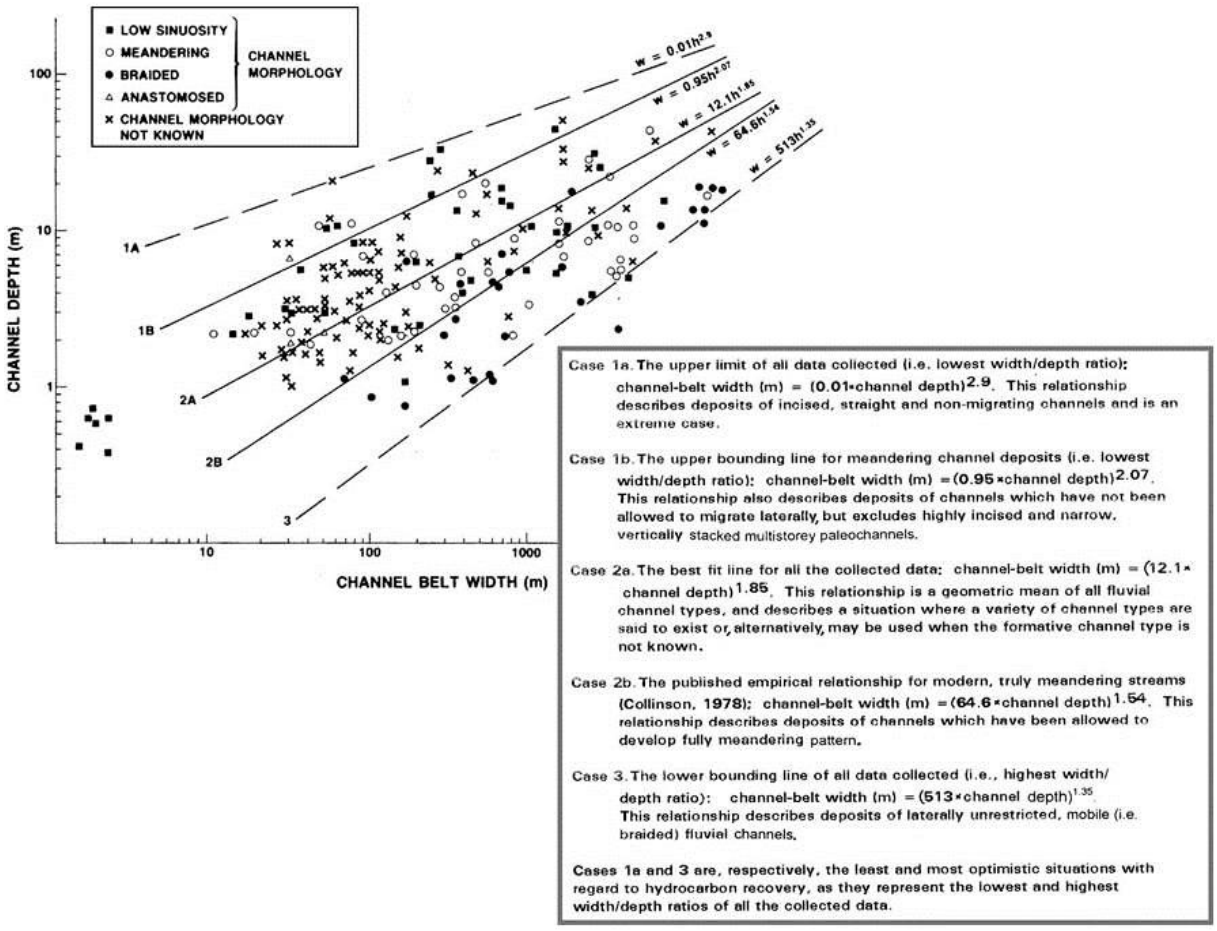

Fig. 5.2. Scatter plot of channel-belt width vs. channel depth, from both modern and ancient fluvial systems (from 45 different sources). From Fielding and Crane (1987)

The spread in the global data on fluvial dimensions can be reduced by dividing up the fluvial deposits into sub-groups based on different criteria, e.g. channel-morphology, depositional climate, type of depositional basin, sediment supply, lithology of the sediment source, system tracts, etc.. Since there are so many factors that influence channel-belts dimensions and spatial distribution, there is an almost unquenchable demand for further population of fluvial channel-belts into the “global channel-belt dimension database” in order for more precise estimations of channel-belt dimensions in the subsurface.

5.2 Measurement of Sandbody Thickness and Width

The tectonic tilt in the Nine Mile Canyon area is very minor (see section 2.4), and therefore not been taken into consideration when measuring the thicknesses of sandbodies on the Virtual Outcrop. The measured thicknesses are therefore an approximation of true thickness. Most of the sandbodies in the interval are however obliquely cut by the outcrop; this causes their measured widths to be wider than their real widths. Therefore the measured widths were corrected, this was done with the simple geometrical calculation (see section 3.3.5 for outline of method; based on Fabuel-Perez et al. (2009). For an ideal result the palaeo-channel orientation is needed for each individual sandbody. For practical reasons the palaeocurrents for each individual sandbody were not available, therefore a mean orientation based on 107 collected palaeocurrents was used (see Section 5.3). **Fig. 5.3** shows an example of how two abandonment plug widths were corrected with the mean palaeocurrent as input.

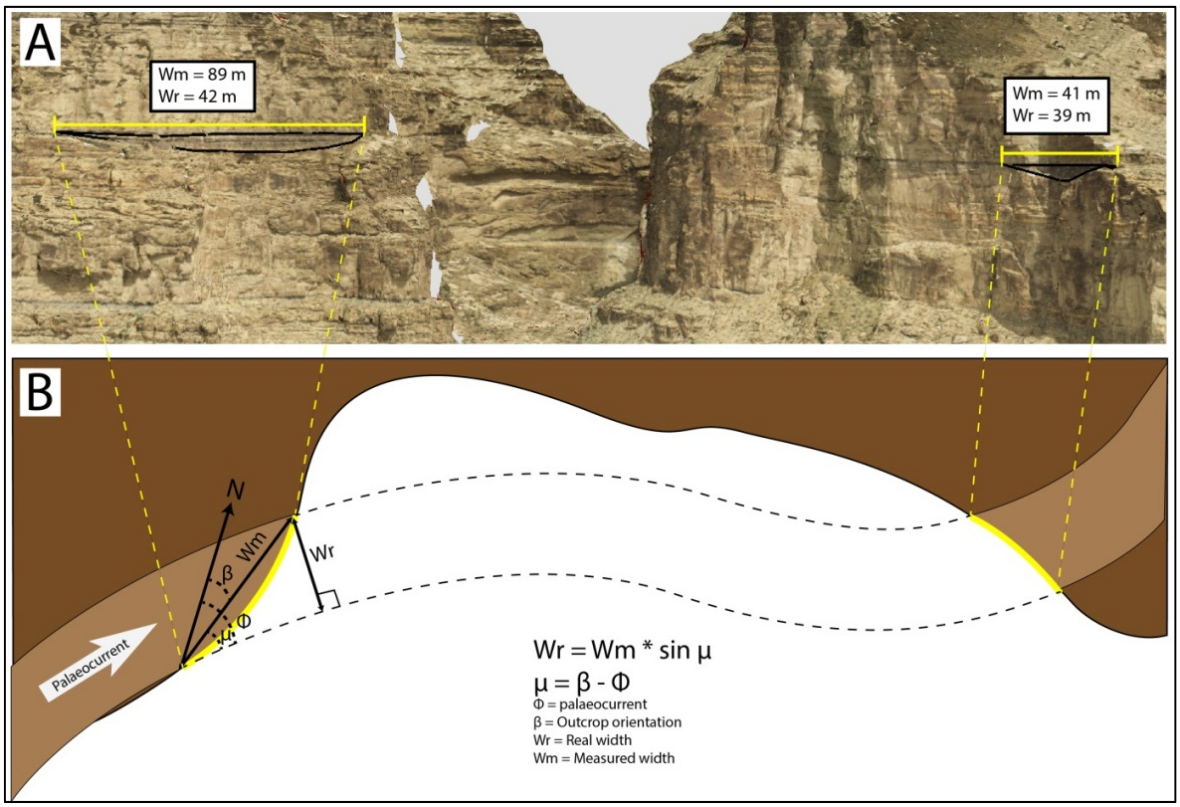

Fig. 5.3. Correction of measured widths. (**A**) Snapshot from Virtual Outcrop, near junction between Cottonwood and Nine Mile canyon, two abandoned channels are interpreted in black. The channel to the left has a measured width ~117% wider than the channel to the right. After calculating the real width for both channels, based on the regional palaeocurrent for the

study interval, the width difference between the channels is reduced to only ~8%. (**B**) Plan view sketch of the outcrop showing possible palaeo-channel outline and calculations to calculate the real width based on measured width and regional palaeocurrent.

5.3 Palaeocurrent Analysis

A total of 107 palaeocurrent measurements were collected during logging. The data are displayed graphically in **Fig. 5.4** and are also given in the sedimentary logs in the appendix. The mean local vector direction is towards 005°, with an angular standard deviation of 65.2^{o}. No vertical trends have been found.

The scatter in the palaeocurrent values may reflect channel sinuosity during deposition (Ghosh, 2000; Le Roux, 1992a; Shukla et al., 1999), but the scatter may also be caused by other factors. The bulk palaeocurrent dataset consists mostly of palaeocurrent measurements from ripple cross-lamination which have low palaeocurrent accuracy; they are supplemented by measurements from trough cross-stratification and solemarks.

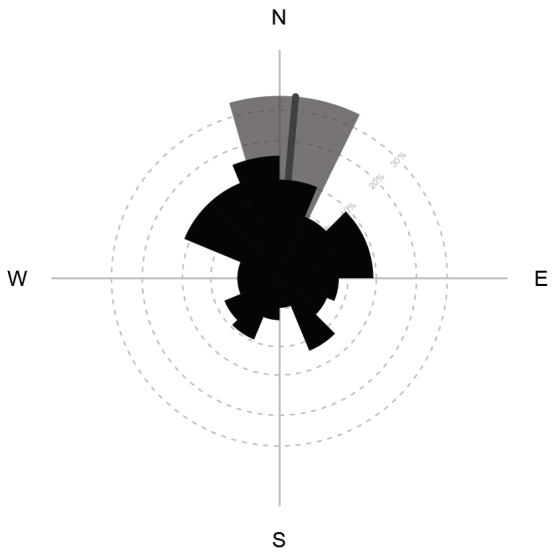

Fig. 5.4. Rose diagram of the bulk palaeocurrent dataset from the Sunnyside Delta interval in the Nine Mile Canyon. *n* = 107. The dark line indicated the mean vector direction and magnitude (length), the grey cone indicated range of ± 1 standard deviation around the mean vector direction.

Statistical results for palaeocurrent analysis:

- Kuiper and Watson tests concludes that the palaeocurrents have a preferential orientation within a confidence level of 95%

- Reyleigh test concludes that the palaeocurrents have a mean/resultant vector within a confidence level of 95%
- Mean channel sinuosity is estimated using Le Roux's (1992) method to be S = 1.87.

5.4 Sandbody Width/Thickness Dimensions

A total of 104 sandbodies were interpreted within the Virtual Outcrop of the Sunnyside Delta interval cropping out in the Nine Mile Canyon. 86 sandbodies are classified as *complete* (both margins exposed), 14 sandbodies are classified as *partly complete* (one margin exposed) and four sandbodies are classified as *incomplete* (no margins exposed). While incomplete and partially complete sandbodies can provide information on minimum width in the absence of other information, the quantity of data from complete sandbodies allowed these to be discarded in this study.

In addition 22 abandonment plugs were interpreted within the Virtual Outcrop. Eight are only partially complete, and therefor discarded, leaving 14 complete abandonment plugs for further analysis.

The bulk dataset is a mixture of sandbodies deposited by different mechanisms, during different sequences and different sequence stratigraphical system tracts. Based on this the bulk data has therefore been subdivided into sub-sets, in order to analyse and reveal potential trends in the data-set (Sections 5.4.2, 5.4.3, 5.4.4). In addition the fluvial sandbodies of the bulk dataset were analysed relative to a vertical datum (section 5.4.5), and a horizontal reference point (section 5.4.6) to investigate vertical and lateral changes in sandbody dimensions. The data-sets are summarized by the below statistical parameters:

- n = number of {*x*, *z*} measurements (i.e., number of channel belts in dataset)
- $\bar{x}$ = mean channel-belt width
- $\bar{z}$ = mean channel-belt thickness
- s^2 = variance (separately for width s_x^2 and thickness s_z^2)
- s = standard deviation (separately for width s_x and thickness s_z)
- mean x/z = $mean\ width/thickness\ ratio$
- $s_{x/z}^2$ = variance of *x*/*z* ratios
- $s_{x/z}$ = standard deviation of *x*/*z* ratios

- r_{xz} = linear correlation between x and z
- $\hat{x} = f(z)$ trend function describing the dependence of x on z
- R^2 = coefficient of determination (the strength of dependence of x on z)

Exeedence frequency (EF) plots with a log-probability scale are made for each of the data-sets. This is a statistical tool that can be used to predict sandbody width and thickness based on the measured values in the data-set. The method has proven to be more robust than traditional probability density plots with arithmetic scale (Drummond and Wilkinson, 1996; Middleton et al., 1995). The usage of EF plots is demonstrated below for the bulk data-set.

5.4.1 Analysis of the bulk dataset

The bulk dataset consists of all 86 interpreted sandbodies. It consists of 14 multi-storey multilateral channel-belts, 12 multi-storey unilateral channel-belts, 12 single-storey multilateral channel-belts, 41 single-storey unilateral channel-belts, 6 mouthbar sandbodies and 1 undifferentiated sandbody.

The exceedene frequency plots are used as a graphical method to recognize the distribution type of the dataset (see chapter 3 for outline of method). Plots for both sandbody width and thickness are made, using logarithmic scale on the x-axis and a probability scale on the y-axis (**Fig. 5.7**).

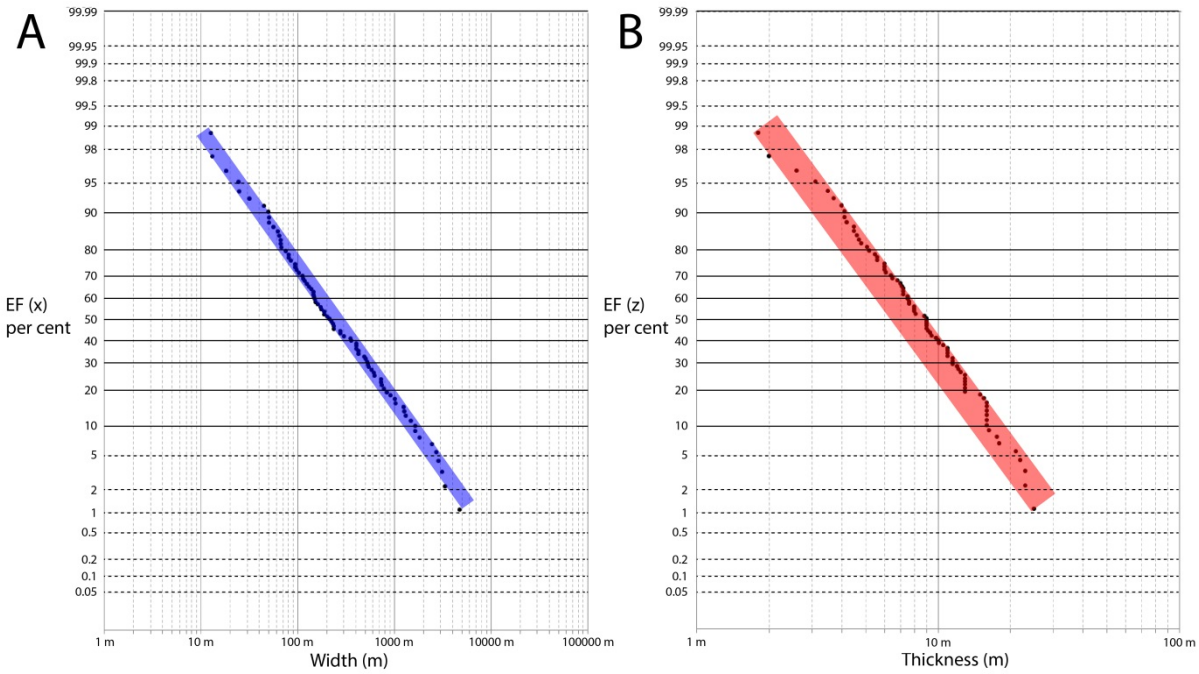

Fig.5.7. EF plots of bulk sandbody width (**A**) and thickness (**B**) in log-probability scale. Both plots show a linear trend, indicating a lognormal distribution. Slight deviation from a perfect linear trend is most likely caused by under sampling, and additionally in **B**, the maximum thickness is used to represent the non-uniform sandbody thickness.

Both the width and the thickness plots show a linear trend of the data points. This indicates a lognormal distribution of the data. The slight deviations from the linear trend are attributed under sampling of dataset variables. While 86 sandbodies is a large amount of data, compared to the total number of sandbodies in the Sunnyside Delta interval it may not be sufficient enough to be a true representation of the general population of sandbodies. The thickness data shows a higher degree of frequency fluctuations than the width data. While the width is a fixed measurement between the two outer margins of the sandbody, the thickness of the sandbodies are laterally non-uniform and the thickness used to represent it is the maximum thickness, which results in a biased dataset.

Given the lognormal distribution of the variables in the dataset, they cannot be represented by conventional Gaussian curves, and therefore arithmetic calculations of the variables mean, standard deviation and variance cannot be used. To transform the statistical parameters that are based on logarithmic values (geometric) back to arithmetic values special formulae are used (equations 6-8 given in Chapter 3;(Wilks, 1995)). The statistical summary of the bulk dataset is presented in **Table 5.2**.

Table 5.2. Statistical summary of bulk dataset of sandbody width and thicknesses from the Sunnyside delta interval. The symbols for the statistical parameters are described in the introduction to section 5.4)

$\bar{x}$	392.16
s_x	445.72
s_x^2	198667.91
$\bar{z}$	9.22
s_z	3.53
s_z^2	12.47
Mean x/z	39.20
$S_{x/z}$	32.69
$S_{x/z}^2$	1069.01
Correlation x vs. z	0.96
$\hat{x} = f(Z)$	$\hat{x} = 2.52 \cdot Z$
n	86

The sandbody widths range from ~13 m to ~5700 m, with a mean of ~392 m ± a standard deviation of ~445 m. The thicknesses range from 1.8 m to 25 m, with a mean of ~9 m ± a standard deviation of ~3.5 m. The width/thickness (x/z) ratio ranges from ~2.2 to 712, with a mean of ~39 m ± a standard deviation of ~33 m (**Table 5.2**).

One way to present the data visually is by fitting lognormal probability-density curves over frequency histograms of measured sandbody widths and thicknesses using a simple arithmetic scale (**Fig. 5.8A, B**). The curves are based on the variables calculated mean and standard deviation and are an approximation of the histograms. There is a significant visual margin of uncertainty related to their goodness of fit with the actual measured data. This uncertainty also applies for the cumulative probability-density functions of the dataset which are also derived from the mean and the standard deviation of the measured data (**Fig.5.8C, D).**

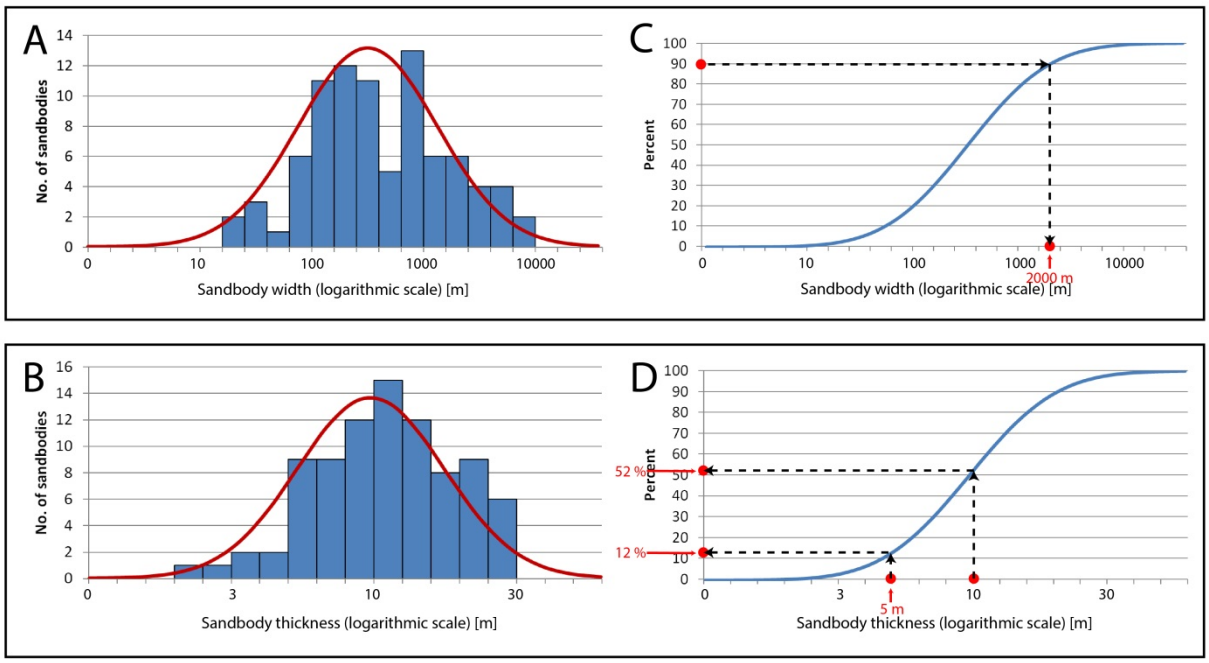

Fig. 5.8. (**A**, **B**) Lognormal probability-density curves (red lines), matching the frequency histograms of sandbody width and thickness from the Sunnyside delta interval. (**C**, **D**) Cumulative lognormal probability-density curves based on the mean and standard deviation of the width and thickness. Two examples of usage are shown with stippled arrows; the plot predicts that 90% of the sandbodies have a width narrower than ~2000 m (**C**), Sandbodies with a width range between ~5 - ~10 m have an occurrence probability of ~40% (**D**). Note than the scales of the x-axis are logarithmic, with increments of $10^{0.2}$ for **A**, **C** and $10^{0.1}$ for **B**, **D**.

The visual uncertainty in the two probabilistic plots (**Fig. 5.8**) are attributed the use of an arithmetic scale to present the lognormal distributed data. The exceedence frequency plots (**Fig.5.7**) provide an alternative way of viewing the data which, instead of being based on the calculated mean and standard deviation of the dataset, is based on a linear approximation of the plotted width and thickness dataset resulting in a de-cumulative probability-density distribution. A case study is presented below demonstrating e.g. how a reservoir modeller, who has selected the Sunnyside Delta interval as a possible analogue to his hydrocarbon reservoir, can extract useful information from the EF plots and use it as input for stochastic modelling of sandbody widths within his reservoir model.

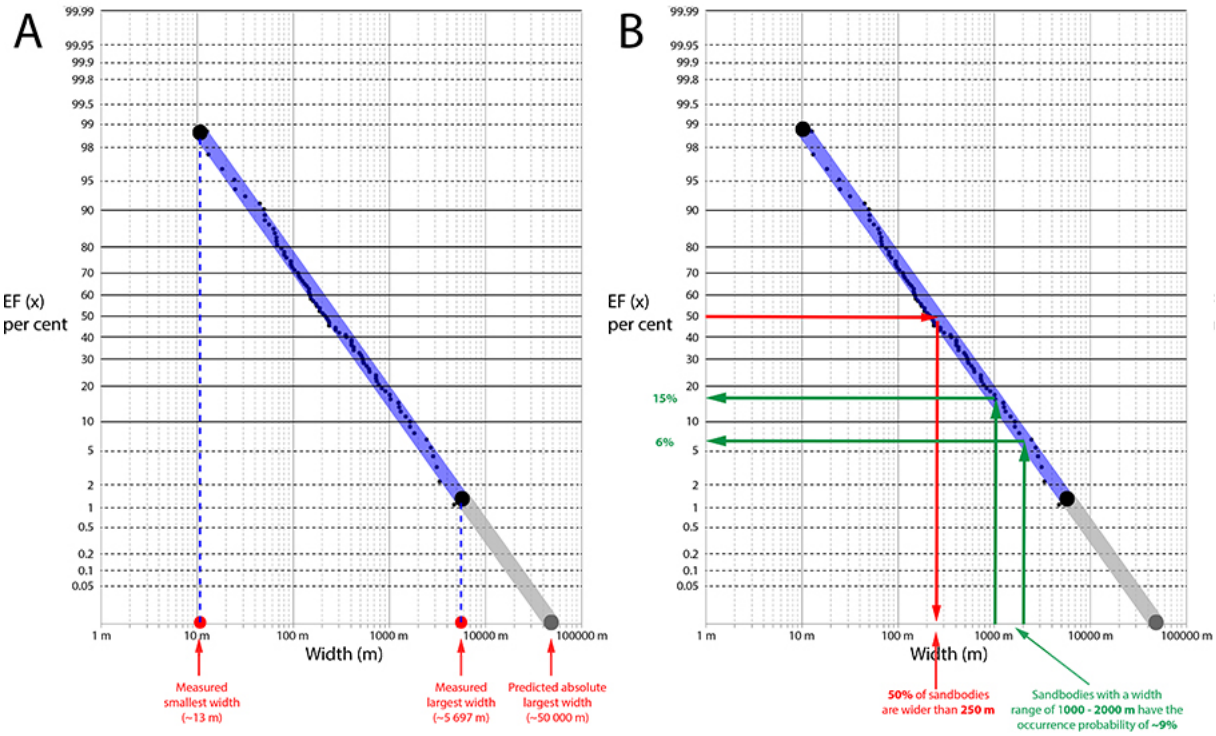

Fig.5.9. Case study of the usage of EF-plots. Here the EF plot for sandbody width from Fig. 5.7A is reproduced for interpretation.

The EF-plot of the sandbody width in the bulk dataset predicts that there is <~1.4 % probability of the occurrence of sandbodies wider than the maximum measured value of 5697 m (**Fig.5.9A**). The probability for wider sandbodies rapidly decreases until the predicted absolute largest width at ~50000 m, which is found by extending the linear line between the measured values (blue line) until it crosses the x-axis (grey line). The plot may also be used to

find the width value of a given probability EF, e.g. reading of 50% on the y-axis corresponds to 250 m on the x-axis (red line **Fig. 5.9B**), this implies that 50% of the sandbodies measured are wider than 250 m and the other 50% are narrower than 250 m. Values may also be read of the other way around, by selecting a given width value or a range between two width values on the x-axis, the probability of encountering sandbodies in this range may be read off the y-axis, e.g. the occurrence probability of sandbodies in the range of 1000 – 2000 m in the Sunnyside delta interval is predicted by the EF plot to be 9% (green lines **Fig. 5.9B).**

To analyse the statistical relationship between sandbody widths and thicknesses the data has been plotted in a scatter plot (**Fig. 5.10.**). Because it is not physically possible to have X > 0 when Z = 0 e.g. a 10 m wide channel that is 0 m deep, the dataset has been supplemented with the addition of an *n*-amount of dummy values of {Z = 0 and X = 0}. The trendline of linear correlation for the extended dataset is thereby forced to follow the physical requirement of intersecting with Z = 0 and X = 0. The trendline for the extended bulk dataset shows a strong linear correlation coefficient value r_{zx} of 0.963 with a calculated 99.95% confidence level (**Table 5.3**)

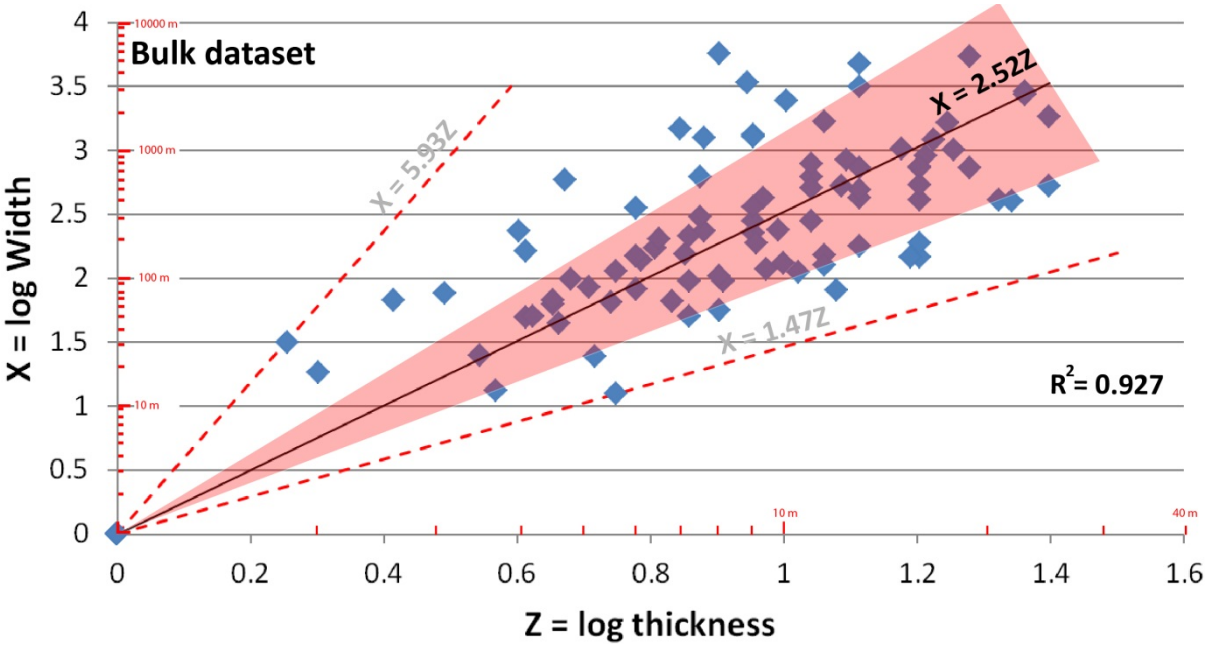

Fig. 5.10. Scatter plot of the bulk dataset showing z = logThickness vs. x = logWidth along with the corresponding trendline of linear regression (x = 2.52Z), its goodness of fit coefficient (R^2 = 0.927) and its confidence sector of ± 1 standard deviation (pink cone). Arithmetic values are shown with red tics on the inside of the axes.

The coefficient of determination (R^2) of the trendline is 0.927; this implies that 92.7% of the change in sandbody width is controlled by changes in sandbody thickness. The remaining 7.3% is controlled by other variables like variable maturity of sandbodies between avulsions.

Table 5.3. The significance of linear correlation coefficient for the bulk dataset of sandbody width vs. thickness tested using the Fisher test (test described in Chapter 3).

One-tail hypothesis tested	H_0: $\rho \leq 0$ (non-significant correlation) H_1: $\rho > 0$ (significant positive correlation)
Coefficient of determination (R^2)	0.927
Coefficient of linear correlation (r)	0.963
Trend line's goodness-of-fit ($R^2 \cdot 100\%$)	92.7%
Calculated t-value	32.66
Degrees of freedom (DF = n – 2)	84
Critical t-value for α=0.0005	3.40
Conclusion	H_0 rejected with 99.95% confidence; H_1 accepted

5.4.2 Analysis of architectural elements

In order to look for trends in the sandbody dimensions within the Sunnyside Delta interval, the bulk dataset was split up into groups reflecting depositional processes and stacking patterns ; multi-storey multilateral channel-belts (MM), multi-storey unilateral channel-belts (MU), single-storey multilateral channel-belts (SM), single-storey unilateral channel-belts (SU) and mouthbar sandbodies (MB) (see section 3.3.4 for grouping criteria).

Exceedence frequency plots were used for all the different sandbody type datasets to identify the frequency distribution of their variables; sandbody widths and thicknesses (for description of method see section 3.5.1 and case-study for their potential usage in section 5.4.1) (**Fig. 5.11-Fig. 5.15**).

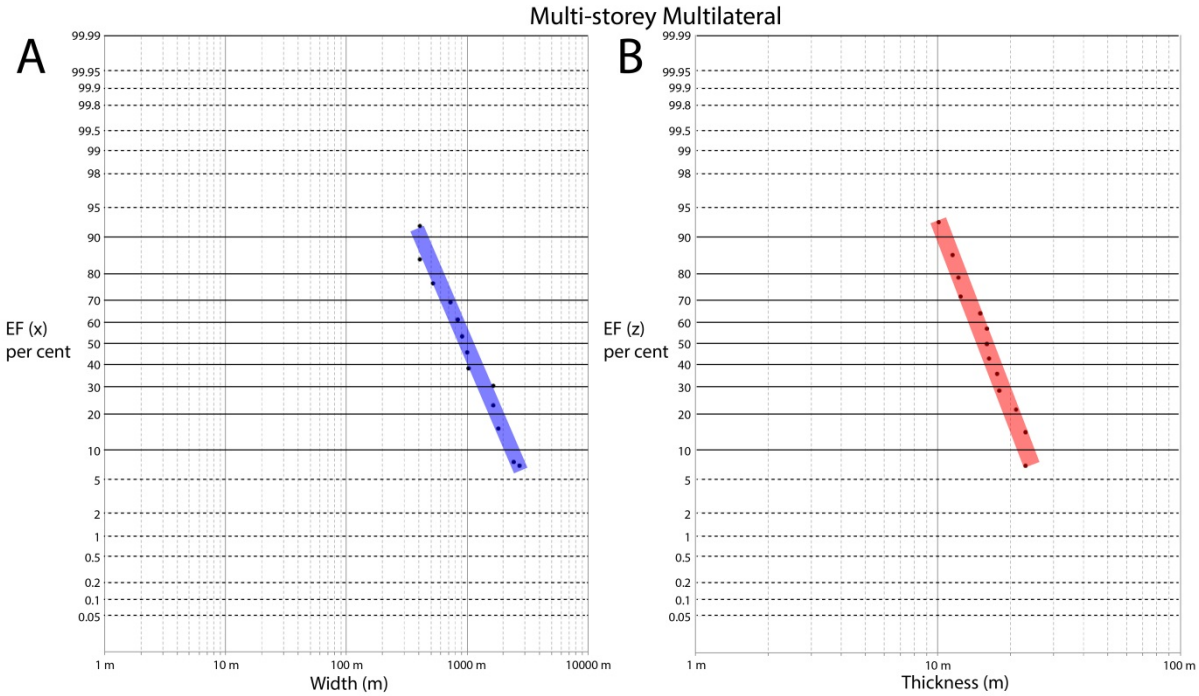

Fig.5.11. EF plots for Multi-storey multilateral (**A**) width and (**B**) thickness in log-probability scale. The plots show a linear trend indicating a lognormal distribution. Small deviations from the linear trend are attributed under sampling of sandbodies.

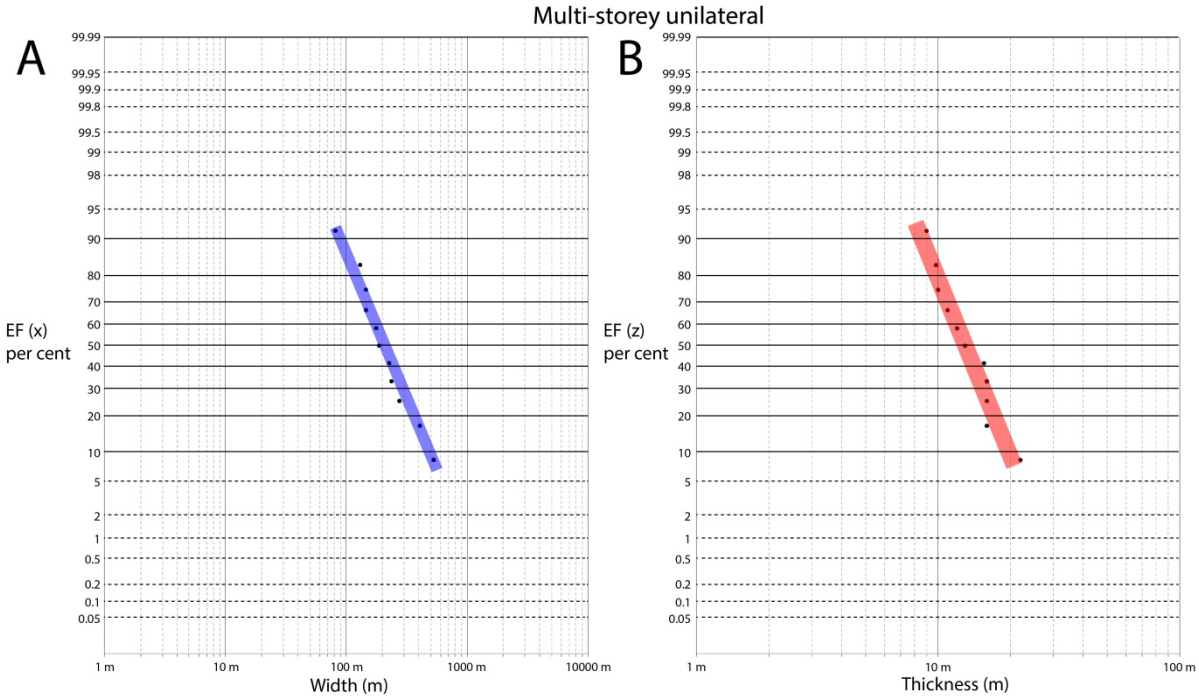

Fig.5.12. EF plots for Multi-storey unilateral (**A**) width and (**B**) thickness in log-probability scale. The plots show a linear trend indicating a lognormal distribution. Small deviations from the linear trend are attributed under sampling of sandbodies.

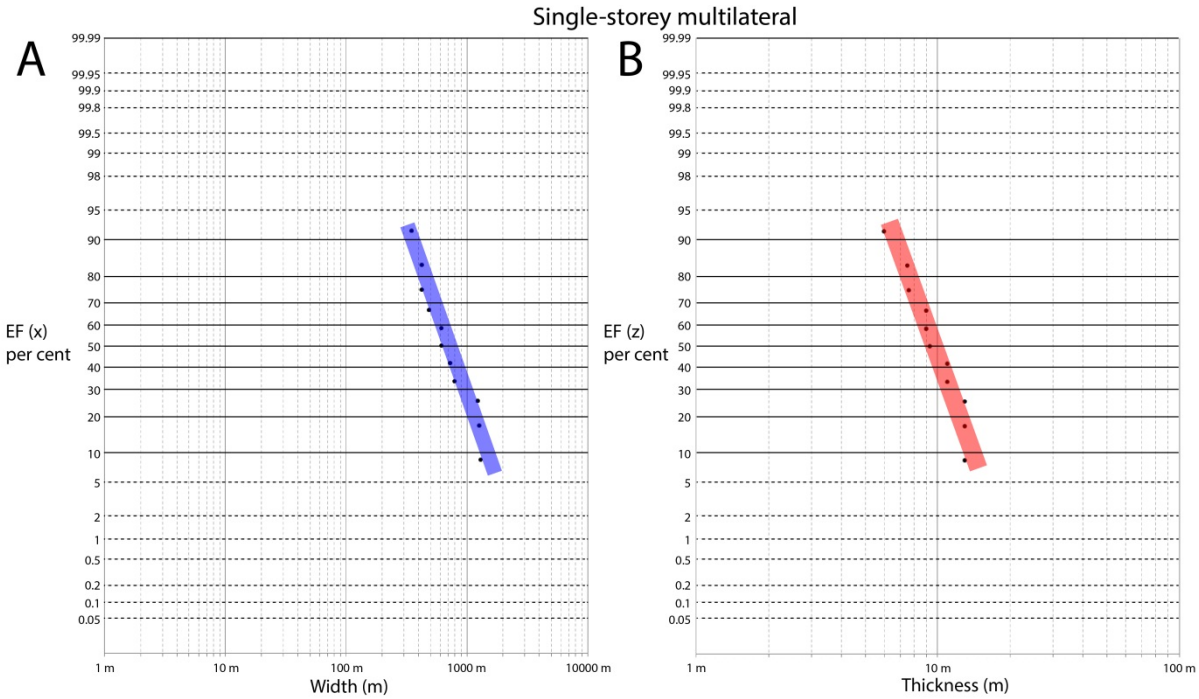

Fig.5.13. EF plots for Single-storey multilateral (**A**) width and (**B**) thickness in log-probability scale. The plots show a linear trend indicating a lognormal distribution. Small deviations from the linear trend are attributed under sampling of sandbodies.

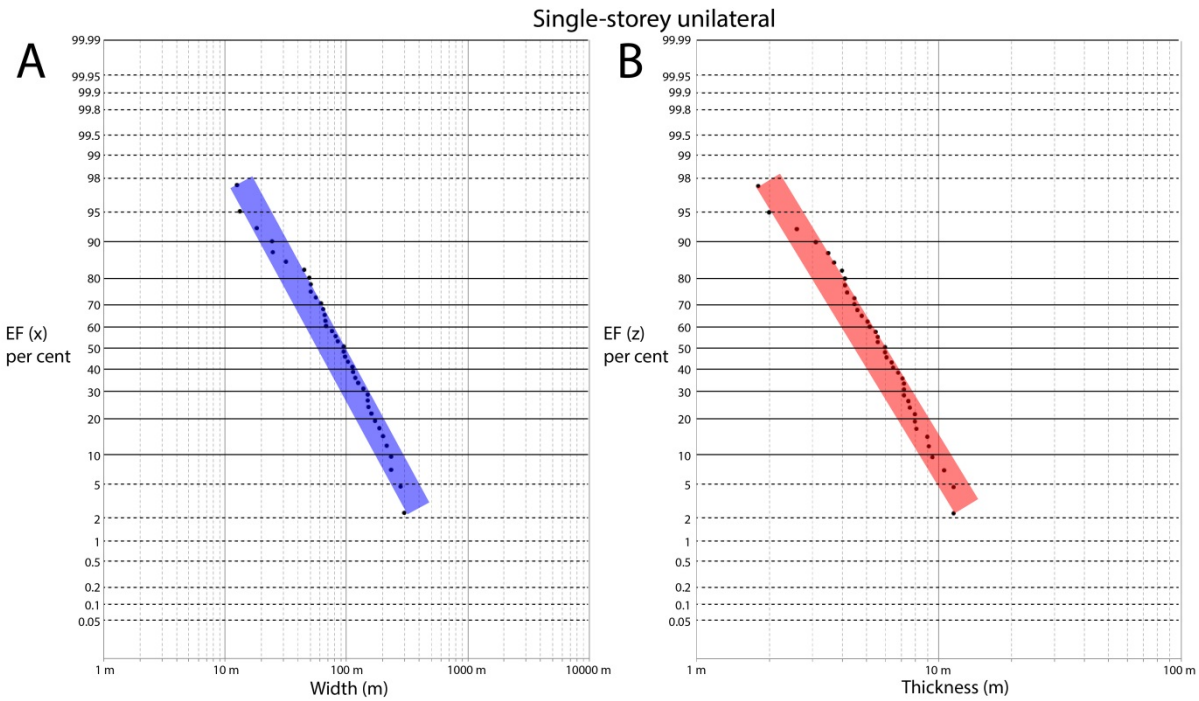

Fig.5.14. EF plots for single-storey unilateral (**A**) width and (**B**) thickness in log-probability scale. The plots show a linear trend indicating a lognormal distribution. Small deviations from the linear trend are attributed under sampling of sandbodies..

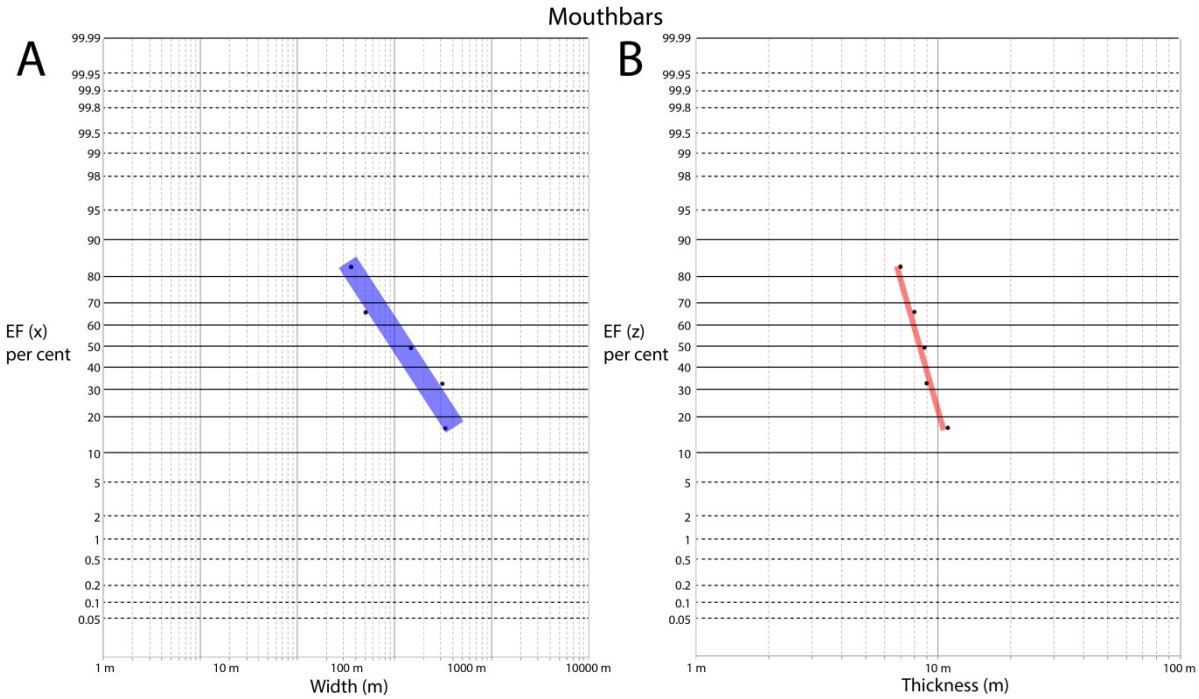

Fig.5.15. EF plots for mouthabars (**A**) width and (**B**) thickness in log-probability scale. The plots show a linear trend indicating a lognormal distribution. Small deviations from the linear trend are attributed under sampling of sandbodies. Note the narrow range of the thickness values relative to the wide range in width values.

All the exceedence frequency plots show linear trends, which indicates that they have a lognormal distribution (**Fig. 5.11 – Fig. 5.15**). Slight deviations are attributed to under sampling of the sandbody types. With the exception of the Single-storey unilateral group, the groups consists of only 6 – 14 sandbodies, which is not enough sandbodies to properly represent the true population of sandbodies within the different sandbody types of the Sunnyside Delta interval. Also for thickness plots additional scatter in the data are attributed to the maximum thickness being used to represent the non-uniform thickness of the measured sandbodies, this is especially apparent for the multi-storey multilateral thickness EF plot, where the lateral sandbody thicknesses may vary greatly (**Fig. 5.11B**). The evidence for lognormal distribution implies that the width and thickness of the data sub-sets cannot be represented by a Gaussian curve based on arithmetic statistics, therefore formulae for transformation the statistical parameters from the geometric to arithmetic are used (see equations 6-8 given in Chapter 3; Wilks (1995)).

A summary of the statistical results for the sandbody width and thickness from the individual sub-groups are given in **Table 5.4**. Of the four fluvial sandbody types the multi-storey

multilateral has the widest channel-belts (MM $\bar{x}$ = 1126 m ± 543 m) followed by single-storey multilateral (SM $\bar{x}$ = 889 m ± 426 m), the two unilateral groups have markedly narrower channel-belt widths than the two multilateral groups (MU $\bar{x}$ = 236 m ± 89 m, SU: $\bar{x}$ = 104 m ± 64 m). For thickness it is the two multi-storey groups that are the thickest (MM $\bar{z}$ = 16.6 m ± 3 m, MU $\bar{z}$ = 14.2 m ± 2.9 m) the two single-storey groups are the thinnest (SM $\bar{z}$ = 10 m ± 1.7 m, SU $\bar{z}$ = 6 m ± ~1.8 m). For the width/thickness ratio the two multi-storey groups have the highest values (MM mean x/z = ~75 ± ~34, SM mean x/z = ~90 ± ~42) while the two unilateral groups have markedly smaller and very similar values (MU mean x/z = ~16.7 ± ~5.4, SU mean x/z = ~17 ± ~8). The mouthbars measured in the Sunnyside Delta interval have the widest sandbodies of all the sandbody types, but are also the most variable (MB $\bar{x}$ = 1990 m ± 1493 m), in contrast their thicknesses are the second thinnest of all the sandbody types (MB $\bar{z}$ = 9.4 m ± ~1.3 m), only thicker than the single-storey unilateral channel-belts, the variation in the mouthbar sandbody thicknesses is however the lowest of all the sandbody types. The mouthbar width/thickness ratio is almost three times as high as the second highest value of the sandbody types, the multi-storey multilateral group, but it also has the by far greatest variability in the values (MB mean x/z = ~219 ± ~172).

Table 5.4 Statistical summary of the sandbody width and thickness for different sandbody types in the Sunnyside Delta interval. The statistical symbols are described in the introduction to section 5.4.

	Multi-storey multilateral	**Multi-storey unilateral**	**Single-storey multilateral**	**Single-storey unilateral**	**Mouthbars**
$\bar{x}$	1225.99	235.84	889.01	104.15	1989.62
s_x	542.63	89.22	426.36	63.54	1493.15
s_x^2	294451.62	7960.63	181786.26	4037.24	2229504
$\bar{z}$	16.60	14.20	10.04	6.05	9.36
s_z	2.97	2.89	1.65	1.84	1.26
s_z^2	8.83	8.40	2.73	3.39	1.58
Mean x/z	75.23	16.66	89.52	16.97	218.60
$S_{x/z}$	33.83	5.39	42.32	7.95	172.30
$S_{x/z}^2$	1144.27	29.00	1790.62	63.14	29688.44
Correlation x vs. z	0.99	0.99	0.98	0.96	0.97
$\hat{x} = f(Z)$	$\hat{x} = 2.49 \cdot Z$	$\hat{x} = 2.03 \cdot Z$	$\hat{x} = 2.89 \cdot Z$	$\hat{x} = 2.47 \cdot Z$	$\hat{x} = 3.28 \cdot Z$
n	14	12	12	41	6

All the sandbody type datasets are plotted in scatterplots supplemented with an *n*-amount of dummy values {Z = 0 and X = 0} to force the linear regression to follow the physical requirement of intersecting Z = 0 and X =0. The corresponding trend lines of the extended datasets are included in the plots together with their coefficient of determination, R^2 (**Fig. 5.16**).

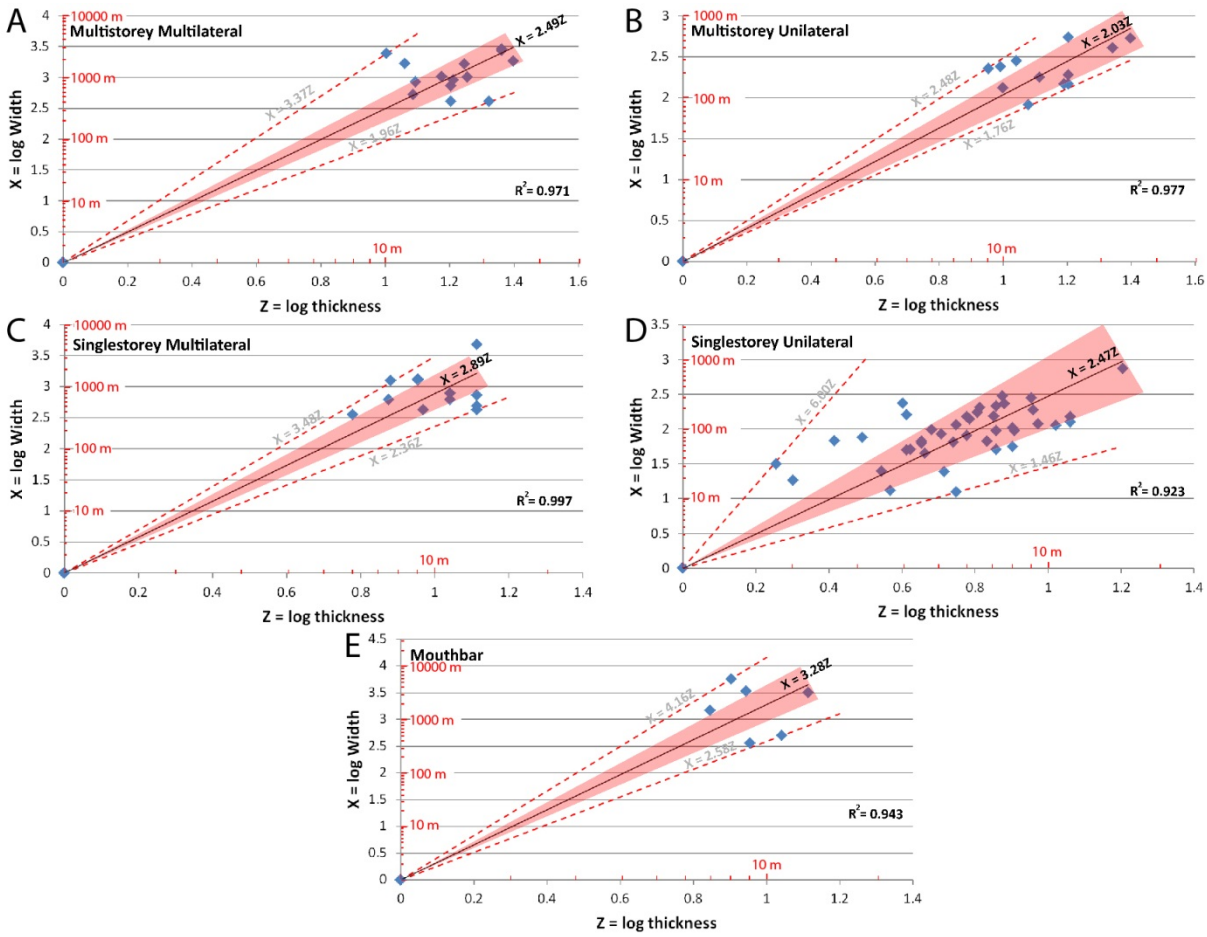

Fig.5.16. Scatter plots of the dataset sub-sets showing z = logThickness vs. x = logWidth along with the corresponding trendlines of linear regression, their goodness of fit coefficients (R^2) and their confidence sectors of ± 1 standard deviation (pink cones). Arithmetic values are shown with red tics on the inside of the axes.

The extended datasets with sandbody width and thickness values have correlation coefficient values in the range r_{zx} = 0.96 – 0.99 (**Table 5.5**). Fisher tests to test the significance of linear correlation conclude that all the fluvial sub-sets are significant within a confidence level of 99.95%, the mouthbar dataset is significant within a confidence level of 99.50%, the slightly lower confidence level is attributed the low number of measured

sandbodies within the mouthbar subset (n = 6) and the subset therefore only has a degrees of freedom value of 4.

Fischer tests to test the significance of linear correlations was done for all the sandbody type datasets and presented in **Table 5.5**. The trend lines goodness-of-fit ($R^2 \cdot 100\%$) ranges from 92.3% - 97.7%, implying that 92.3% - 97.7% of the change in sandbody widths can be controlled by changes in sandbody thickness (**Table 5.5**). The remaining 2.3% - 7.7% is attributed other controls, e.g. maturity of the channel-belts/mouthbars and/or channel avulsions upstream.

Table 5.5. The significance of linear correlation coefficients for the dataset subsets of sandbody width vs. thickness tested using the Fisher test (Test described in Chapter 3).

One-tail hypothesis tested	H_0: $\rho \leq 0$ (non-significant correlation) H_1: $\rho > 0$ (significant positive correlation)				
Dataset	**Multi-storey multilateral**	**Multi-storey unilateral**	**Single-storey multilateral**	**Single-storey unilateral**	**Mouthbars**
Coefficient of determination (R^2)	0.971	0.977	0.966	0.923	0.943
Coefficient of linear correlation (r)	0.99	0.99	0.98	0.96	0.97
Trend line's goodness-of-fit ($R^2 \cdot 100\%$)	97.1%	97.7%	96.6%	92.3%	94.3%
Calculated t-value	20.19	20.47	16.80	21.64	8.10
Degrees of freedom (DF = n – 2)	12	10	10	39	4
Critical t-value for α=0.0005	4.318	4.587	4.587	3.551	8.610
Critical t-value for α=0.005					4.604
Statistical conclusion	H_0 rejected with 99.95% confidence; H_1 accepted	H_0 rejected with 99.95% confidence; H_1 accepted	H_0 rejected with 99.95% confidence; H_1 accepted	H_0 rejected with 99.95% confidence; H_1 accepted	H_0 rejected with 99.50% confidence; H_1 accepted

Other architectural elements: Abandonment plugs

Abandonment plugs are a good indication of palaeochannel bankfull width and have therefor been measured on the Virtual Outcrop in order to give additional insight in the dimensions of the palaeo-channels depositing Sunnyside Delta sandbodies. A total of 22 abandonment plugs are interpreted on the Virtual Outcrop, of which 8 abandonment plugs are discarded from further analysis because of unexposed margins.

The same statistical analysis as presented for the bulk dataset is done for the abandonment plug dataset. For a further elaboration of the analysis, beyond what is presented below, see section 5.4.1.

Exceedence frequency plots with log-probability scale reveals a linear trend for both the thickness and width variables in the abandonment plug dataset, which indicates a lognormal distribution of the data (**Fig. 5.17**). Deviations from the linear trend is attributed under sampling; abandonment plugs are normally filled with fine grained material that easily weathers and gets covered with scree, the visible abandonment plugs in the study area are most often overlain by a more resistant sandstone or limestone sheltering it from weathering. Therefore the measured abandonment plugs are probably only a fraction of the true population within the study area.

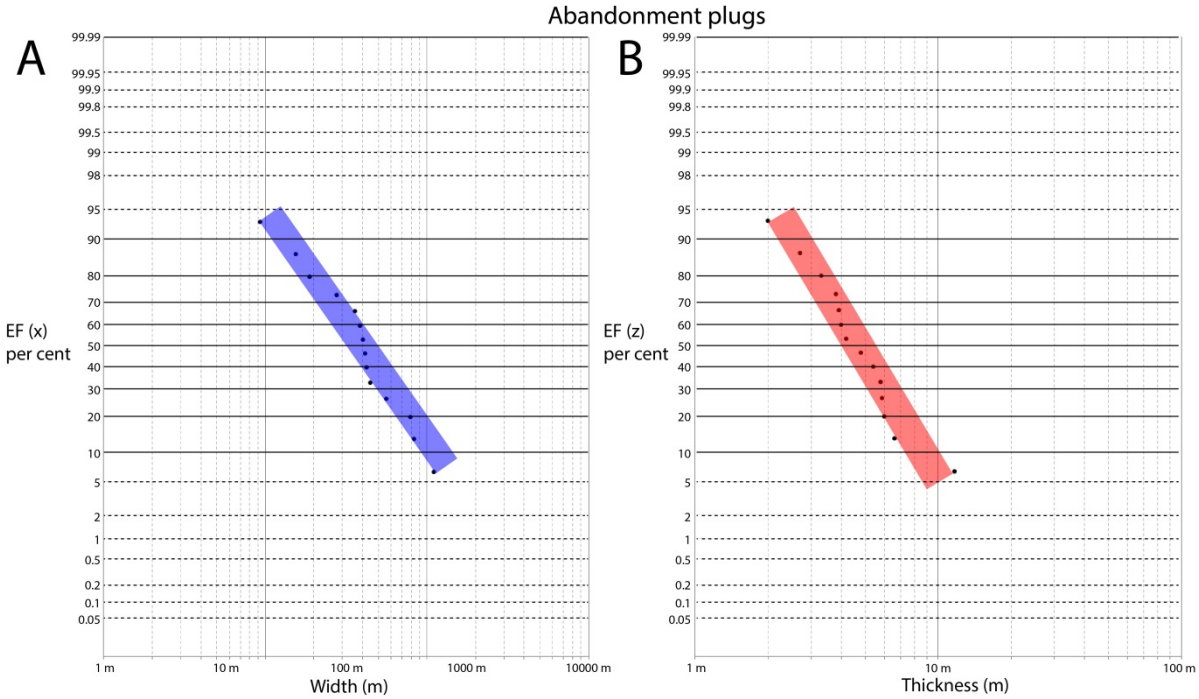

Fig. 5.17. EF plots of abandonment plug width (**A**) and thickness (**B**) in log-probability scale. Both plots show a linear trend, indicating a lognormal distribution. Slight deviations from the linear trend are most likely caused by under sampling.

The measured abandonment plug widths are in the range 9 m – 150 m, with a mean width of ~61 m ± a standard deviation of ~30 m (**Table 5.6**). Their thicknesses range between 2 - ~14 m, with a mean thickness of ~5.8 m ± a standard deviation of ~1.9 m. The ratio between width and thickness ranges between ~4 to ~19, with a mean X/Z ratio of ~10 ± a standard deviation of ~3.

Table 5.6 Statistical summary of measured abandonment plug width and thicknesses within the Sunnyside delta interval. The symbols for the statistical parameters are described in the introduction to section 5.4)

$\bar{x}$	61.06
s_x	30.33
s_x^2	919.75
$\bar{z}$	5.83
s_z	1.93
s_z^2	3.71
Mean x/z	10.30
$S_{x/z}$	3.07
$S_{x/z}^2$	9.41
Correlation x vs. z	0.97
$\hat{x} = f(Z)$	$\hat{x} = 2.2363 \cdot Z$
N	14

The extended abandonment plug dataset (supplemented with an *n*-amount of dummy values {Z=0, x=0}) thicknesses and widths are plotted against each other in a scatter plot in order to statistically examine the relationship between the two variables (**Fig. 5.18**). The trend line, based on linear regression, for the dataset has the equation X = 2.24Z, implying the abandonment plug widths generally increase ~17.3 m in width for every additional metre in thickness ($10^{2.24}$ / 10). It has a coefficient of determination R^2 of 0.932, implying that 93.4% of the abandonment plug width can be attributed the changes in thickness and the remaining 6.4% are attributed other factors.

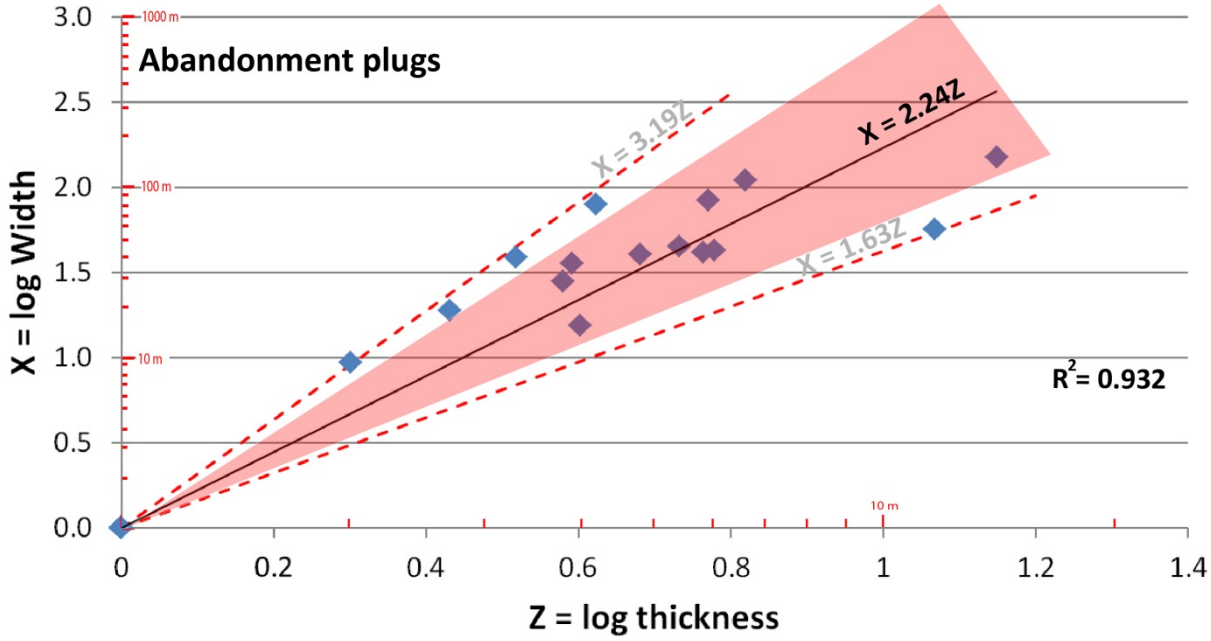

Fig. 5.18. Scatter plot of the bulk dataset showing Z = logThickness vs. X = logWidth along with the corresponding trendline of linear regression (X = 2.24Z), its goodness of fit coefficient (R^2 = 0.932) and its confidence sector of ± 1 standard deviation (pink cone). Arithmetic values are shown with red tics on the inside of the axes.

The coefficient of linear correlation of the abandonment plug dataset is r_{zx} = 0.965. The Fisher test concludes that r_{zx} is significant within a 99.95% confidence level (**Table 5.7**).

Table 5.7. The significance of linear correlation coefficient for the abandonment plugs width vs. thickness tested using the Fisher test (Test outlined in Chapter 3).

One-tail hypothesis tested	H_0: $\rho \leq 0$ (non-significant correlation) H_1: $\rho > 0$ (significant positive correlation)
Coefficient of determination (R^2)	0.932
Coefficient of linear correlation (r)	0.965
Trend line's goodness-of-fit ($R^2 \cdot 100\%$)	93.2%
Calculated t-value	12.79
Degrees of freedom (DF = n – 2)	12
Critical t-value for α=0.0005	4.318
Conclusion	H_0 rejected with 99.95% confidence; H_1 accepted

5.4.3 Datasets from individual sequences

The sequence stratigraphy of the Sunnyside Delta interval is described by Keighley et al. (2003), a description of this is given in section 2.3.3. They split the interval up into units (U1-U10) bounded by carbonate markers (M1-M11) (**Fig. 5.19**). The three type A sequences between the M11 and M8 have been split up into one group per sequence, U10 (Seq. 4A), U9 (Seq. 3A), U8 (Seq. 2A), using flooding surfaces instead of fluvial incisions as sequence boundaries, this is done for practical reasons since the carbonate markers associated with the flooding surfaces provide a much more distinct boundary than the fluvial erosion surfaces. Moore et al. (2012) also used flooding surfaces when dividing up their study interval up into parasequences bounded by flooding surfaces. The two, lower order, type B sequences below the M8 marker contain internal carbonate markers associated with flooding surfaces, and are therefore split up into several units per sequence. U7 and U6 have therefore been grouped together (Seq. 1.3B), and U5, U4 and U3 have been grouped together (Seq. 1.2B).

The same statistical analysis as presented for the bulk dataset was done for all the individual sequences, for a further elaboration of the analysis, beyond what is presented below, see section 5.4.1.

Frequency distribution histograms for both sandbody widths and thicknesses within each of the five sequences are shown in **Fig. 5.20**. A summary of the statistical results for the sandbody widths and thicknesses for each individual sequence is given in **Table 5.8**.

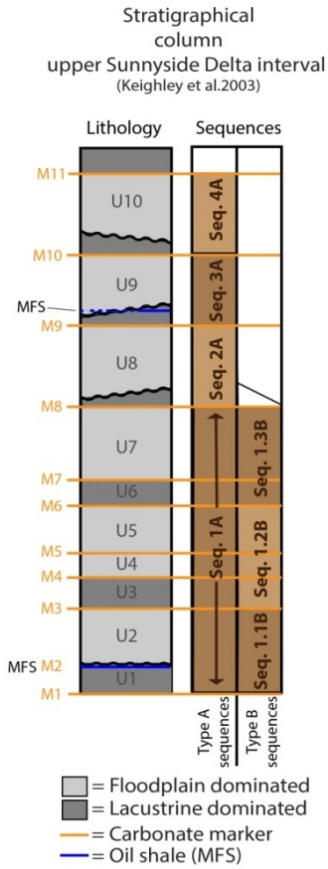

Fig. 5.19. Modified stratigraphic column of Keighley et al. (2003) using flooding surfaces instead of fluvial erosion surfaces as sequence boundaries. Keighley et al. (2003). Sequences are named by the present author. Modified from Keighley et al. (2003)

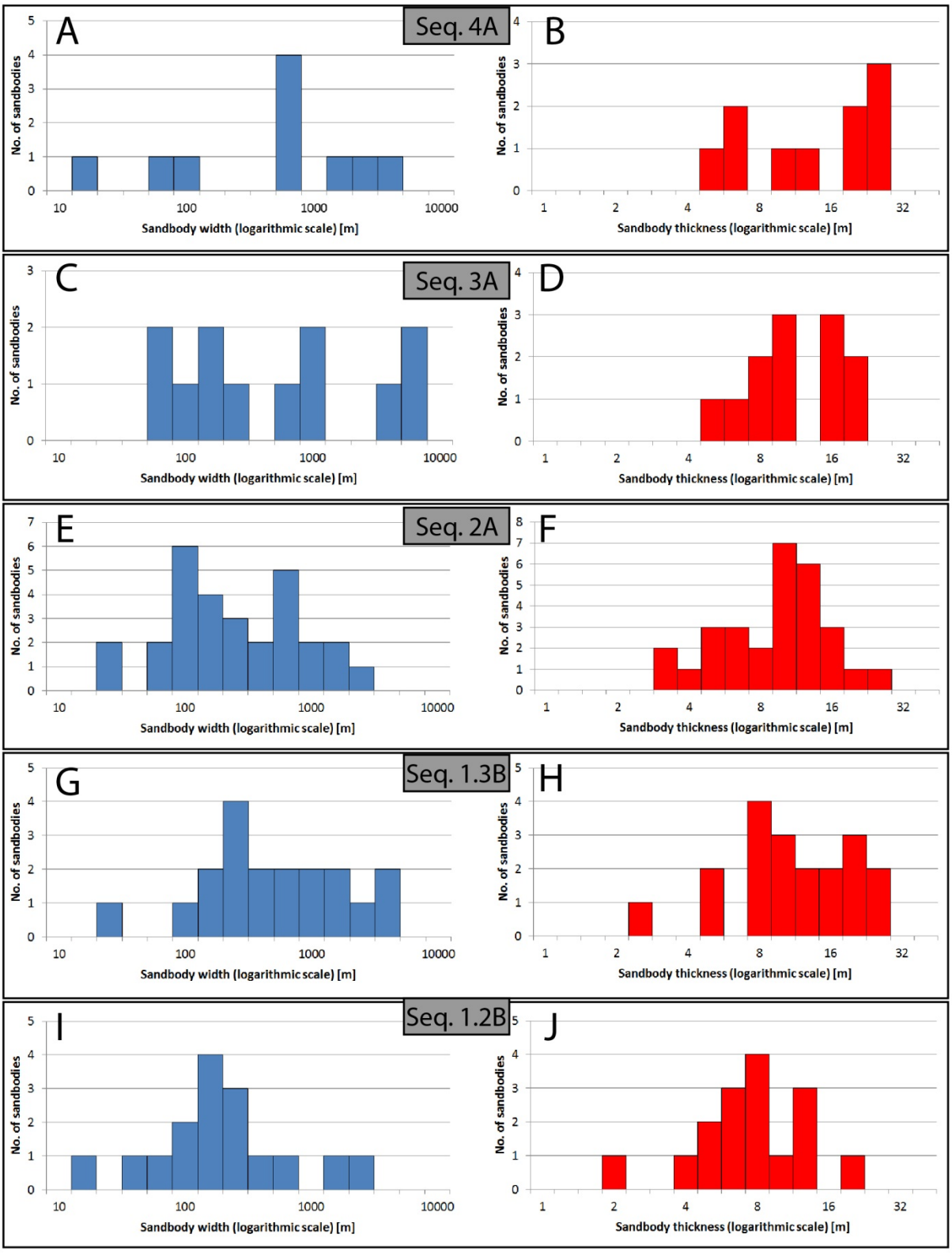

Fig. 5.20 Histograms displaying frequency distribution of sandbody width (A, C, E, G, I) and thickness (B, D, F, H, J) grouped by individual sequences observed in the upper half of the Sunnyside delta interval studied in the Nine Mile Canyon, Utah. The mean width bin for each sequence is marked with an orange circle and connected with an orange line. The mean thickness bin for each sequence is marked with a green circle and connected with a green line.

Table 5.8 Statistical summary of sandbody widths and thicknesses, within individual sequences, of the upper half of the Sunnyside delta interval cropping out in the Nine Mile Canyon. The statistical symbols are described in the introduction to section 5.4.

	Seq. 4A	**Seq. 3A**	**Seq. 2A**	**Seq. 1.3B**	**Seq. 1.2B**
$\bar{x}$	552.82	729.85	271.37	566.91	207.58
s_x	765.37	1067.84	248.66	554.35	200.22
s_x^2	585793.77	1140273.77	61833.06	307305.5	40088.08
$\bar{z}$	12.93	9.72	8.43	10.47	6.96
s_z	5.33	2.49	2.95	4.40	2.41
s_z^2	28.39	6.18	8.71	19.36	5.82
Mean x/z	34.82	71.58	30.35	50.55	29.09
$S_{x/z}$	28.16	92.74	20.52	33.96	23.28
$S_{x/z}^2$	793.21	8607.02	421.10	1153.35	541.80
Correlation x vs. z	0.99	0.94	0.96	0.97	0.94
$\hat{x} = f(Z)$	$\hat{x} = 2.33 \cdot Z$	$\hat{x} = 2.66 \cdot Z$	$\hat{x} = 2.49 \cdot Z$	$\hat{x} = 2.56 \cdot Z$	$\hat{x} =\cdot 2.56\, Z$
n	10	12	29	19	16

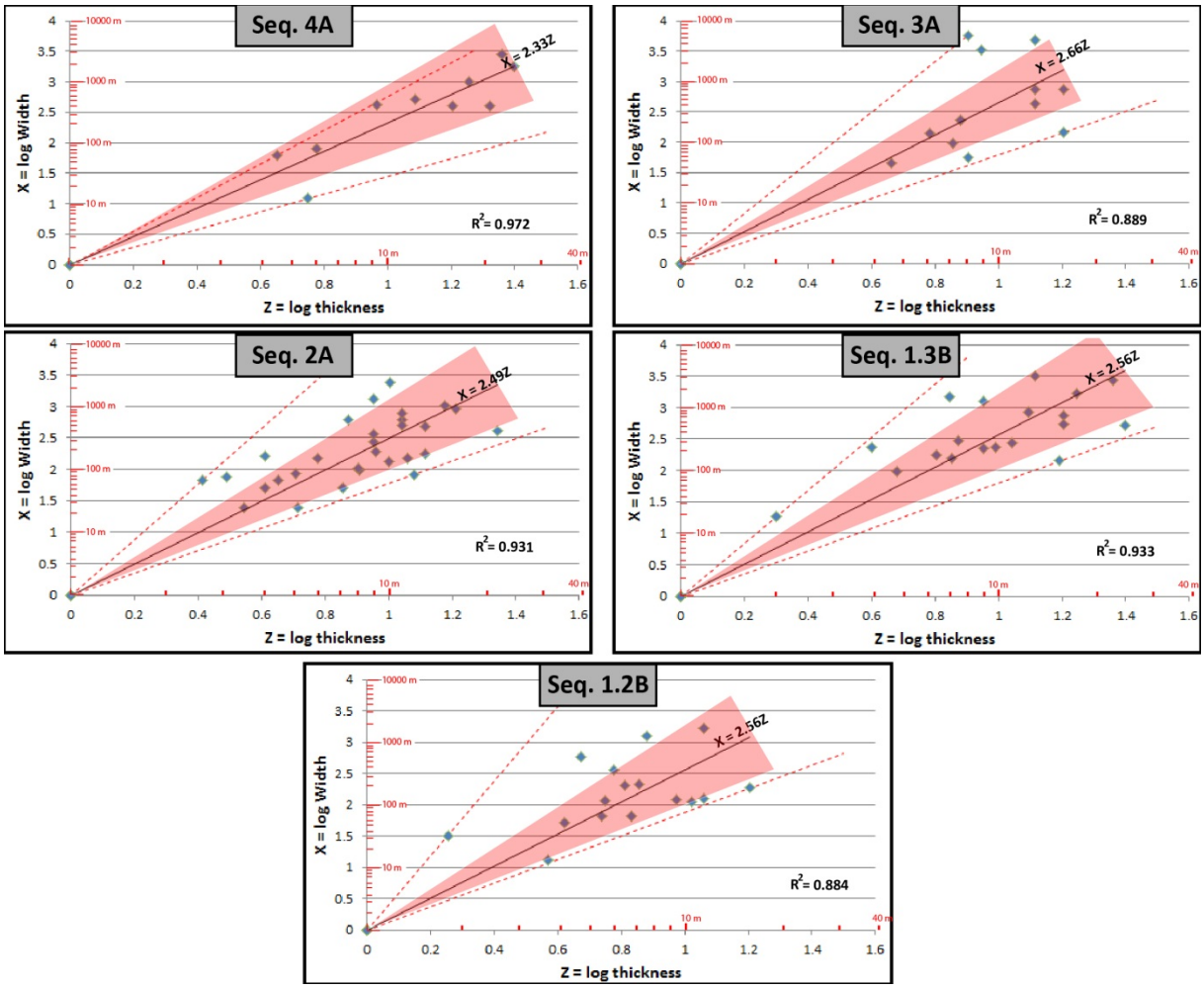

Fig. 5.21. Scatter plots of the individual sequence datasets showing z = logThickness vs. x = logWidth along with the corresponding trendlines of linear regression, their goodness of fit coefficients (R^2) and their confidence sectors of ± 1 standard deviation (pink cones). Arithmetic values are shown with red tics on the inside of the axes.

The mean width for the individual sequences range from ~208 m ± 200 m for sequence 1.2B to 730 m ± 1068 m for sequence 3A (**Table 5.8**). The mean thickness ranges from ~7 m ± ~2.4 m for sequence 1.2B to 12.9 m ± 5.3 for sequence 4A. The mean width/thickness ratio ranges from ~29-35 ± ~20-28 for the 4A, 2A and 1.2B sequences to ~72 ± ~93 for sequence 3A. An overall gentle increase in both sandbody widths and thicknesses is visually observed upwards in the succession (**Fig. 5.20**)

The trendlines (**Fig. 5.21**) for the extended individual sequence datasets (supplemented with an *n*-amount of dummy values {Z=0, X=0}) show strong linear correlations with r_{zx} ranging 0.94 – 0.99, Fisher tests conclude that all the linear correlations are significant within a 99.95% confidence level (**Table 5.9**). The coefficients of determination (R^2) range from

88.4% - 97.3%. Implying that 88.4%-97.3% of the variation in width can be attributed changes in thickness. The remaining 11.6% - 2.7% are attributed other factors.

Table 5.9. The significance of linear correlation coefficient for sandbody width vs. thickness for individual sequences, within the Sunnyside delta interval, tested using the Fisher test (Test outlined in Chapter 3).

One-tail hypothesis tested	H_0: $\rho \leq 0$ (non-significant correlation) H_1: $\rho > 0$ (significant positive correlation)				
Dataset	**Seq. 4A**	**Seq. 3A**	**Seq. 2A**	**Seq. 1.3B**	**Seq. 1.2B**
Coefficient of determination (R^2)	0.972	0.889	0.931	0.933	0.884
Coefficient of linear correlation (r)	0.99	0.94	0.96	0.97	0.94
Trend line's goodness-of-fit ($R^2 \cdot 100\%$)	97.3%	88.9%	93.1%	93.3%	88.4%
Calculated t-value	16.60	8.94	19.03	15.34	10.32
Degrees of freedom (DF = n – 2)	8	10	27	17	14
Critical t-value for α=0.0005	5.041	4.587	3.690	3.965	4.140
Statistical conclusion	In all cases: H_0 is rejected with 99.95% confidence and H_1 is accepted				

Table 5.10. Distribution of sandbody groups within individual sequences.

	Seq. 4A	**Seq. 3A**	**Seq. 2A**	**Seq. 1.3B**	**Seq. 1.2B**
Multi-storey multilateral	60%	8%	10%	16%	6%
Multi-storey unilateral	0%	8%	14%	32%	6%
Single-storey multilateral	10%	25%	17%	5%	13%
Single-storey unilateral	30%	42%	52%	37%	69%
Mouthbar	0%	17%	7%	11%	0%
Undifferentiated	0%	0%	0%	0%	6%

5.4.4 Channel-belt geometry by systems tract

Keighley et al. (2003) subdivided the sequences into systems tracts, these have been given labels by the present author for easier referencing, based on the sequence they are within (**Fig. 5.22**). By analysing the sandbody width and thickness dimensions, within different system tracts, trends related to the relative lake level and sediment supply may be revealed. The data is divided up for both the type A system tracts and the lower order type B system tracts. All the interpreted mouthbars are interpreted to be deposited during TST, and most of the fluvial deposits during LST. With the exception for the fluvial channel-belts in the U5, which are interpreted to be deposited during type B TST. Because of the scarcity of mouthbar measurements for the different TST packages (only 1-2 per TST), only the sandbodies of fluvial origin is included in this analysis.

The channel-belts are grouped into four type A system tracts, 4A LST, 3A LST, 2A LST and 1A TST. In addition the 1A TST is split up into three type B system tracts: 1.3B LST, 1.3B TST, and 1.2B TST. The 1.2B LST is discarded from the analysis because of too few measured sandbodies with margins exposed.

A statistical summary of channel-belt width and thicknesses for the individual system tracts is given in **Table 5.11.**

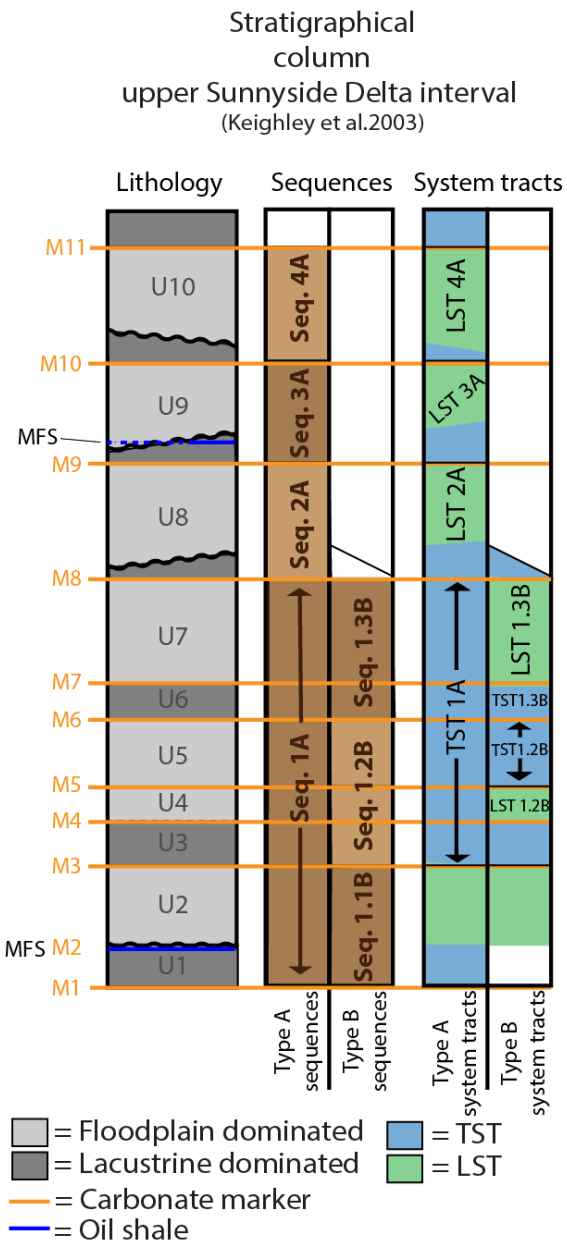

Fig. 5.22. Stratigraphic column based on Keighley et al. (2003). Sequence and systems tracts names are given by the present author. Modified from Keighley et al. (2003)

Table 5.11 Statistical summary of channel-belt widths and thicknesses, within individual system tracts, of the upper half of the Sunnyside delta interval. The statistical symbols are described in the introduction to section 5.4.

	4A LST	**3A LST**	**2A LST**	**1A TST**	**1.3B LST**	**1.3B TST**	**1.2B TST**
$\bar{x}$	552.82	380.18	259.69	310.60	533.91	283.50	145.12
s_x	765.37	405.24	244.31	312.01	557.82	123.49	114.14
s_x^2	585793.77	172422.00	59685.98	97351.66	311164.9	15248.66	13028.58
$\bar{z}$	12.93	10.00	8.32	8.85	10.47	10.79	6.86
s_z	5.33	2.78	3.00	3.73	5.39	1.92	2.41
s_z^2	28.39	7.74	8.99	13.90	29.02	3.67	5.81
Mean x/z	34.82	34.79	29.43	32.33	45.17	26.64	20.89
$S_{x/z}$	28.16	29.22	20.46	21.65	24.58	11.46	13.32
$S_{x/z}^2$	793.21	853.56	418.76	468.90	604.27	131.34	117.38
Correlation x vs. z	0.98	0.97	0.96	0.96	0.97	0.98	0.95
$\hat{x} = f(Z)$	$\hat{x} = 2.33 \cdot Z$	$\hat{x} = 2.44 \cdot Z$	$\hat{x} = 2.48 \cdot Z$	$\hat{x} = 2.48 \cdot Z$	$\hat{x} = 2.54 \cdot Z$	$\hat{x} = 2.33 \cdot Z$	$\hat{x} = 2.43 \cdot Z$
n	10	10	27	32	12	5	14

Of the four type A system tracts the 4A LST has the widest sandbodies ($\bar{x}$ = ~553 m ± ~765 m (standard deviation) followed by 3A LST ($\bar{x}$ = ~380 m ± ~405 m), the 2A LST has the thinnest sandbodies ($\bar{x}$ =~260 m ± ~244 m). The channel-belt thicknesses within the four type A system tracts rank in the same way as the widths, 4A LST having the thickest channel-belts ($\bar{z}$ = ~12.9 m ± ~5.3 m), followed by 3A LST ($\bar{z}$ = 10 m ± ~2.8 m), the 2A LST have and 1A TST have similar thicknesses ($\bar{z}$ = ~8.3-8.9 m ± ~3-3.7 m). The channel-belts mean width/thickness ratio, for the four type A system tracts, rank in the same order as the mean widths and mean thickness and are all in a relatively narrow range (mean x/y = ~29.4-~34.8 ± ~20.5-29.2).

When splitting the 1A TST, into the three type B systems tracts. The 1.3B LST mean channel-belt width and thickness shows similar mean values as the 4A LST and 3A LST (U7_LST: $\bar{x}$ = ~534 m ± ~558 m, $\bar{z}$ = ~10.5 m ± ~5.4 m). The 1.2B TST shows markedly smaller mean width and thickness values than all the other system tracts (1.2B TST: $\bar{x}$ = ~145 m ± ~144 m, $\bar{z}$ = ~6.9 m ± ~2.4 m), the 1.3B TST has narrower widths that the 4A and 3A LSTs, and slightly wider widths than 2A LST, but has half the variation in channel-belt widths relative to the 2A LST, the mean thickness is within the same range as all the 4A and 3A LSTs, and thicker than the 2A LST (1.3B TST: $\bar{x}$ = ~284 m ± ~123 m, $\bar{z}$ = ~10.8 m ± ~1.9 m). The mean

width/thickness ratios show a trend that both the type B TSTs have smaller values and also show less variability in their values (Type B TSTs: mean x/z = ~20.9-26.6 ± 11.5-13.3) than the type A LSTs (Type A LSTs: mean x/z = ~29.4-34.8 ± ~20.5-29.2). The type B LST, the 1.3B LST, shows markedly higher mean x/z values than the type A LSTs (1.3B LST: mean x/z = 45.2 ± 24.6).

Table 5.12. Distribution of fluvial channel-belt grouped within individual system tracts within the sequences of the upper half of the Sunnyside Delta interval

	4A LST	**3A LST**	**2A LST**	**1A TST**	**1.3B LST**	**1.3B TST**	**1.2B TST**
Multi-storey multilateral	60%	10%	11%	13%	17%	20%	0%
Multi-storey unilateral	0%	10%	15%	22%	25%	60%	7%
Single-storey multilateral	10%	30%	19%	9%	8%	0%	14%
Single-storey unilateral	30%	50%	56%	56%	50%	20%	79%

A scatter plot with all the extended system tracts datasets (*n*-amount of dummy values {Z=0,X=0} were added to the datasets) is shown in **Fig. 5.23**. All the corresponding trend lines show strong linear correlation between channel-belt thicknesses and widths, the coefficients of linear correlation (r_{zx}) ranges from 0.948 to 0.986, all the datasets are significant within 99.95% confidence level, except the 1.3B TST which is significant within a 99.50% confidence level (**Table 5.13**). The trend lines goodness-of-fit range from 89.8% for the 1.2B TST to 97.2% for the 4A LST.

Table 5.13. The significance of linear correlation coefficient for channel-belt width vs. thickness for individual system tracts, within the Sunnyside delta interval, tested using the Fisher test (Test described in Chapter 3).

One-tail hypothesis tested	H_0: $\rho \leq 0$ (non-significant correlation) H_1: $\rho > 0$ (significant positive correlation)						
Dataset	**4A LST**	**3A LST**	**2A LST**	**1A TST**	**1.3B LST**	**1.3B TST**	**1.2B TST**
Coefficient of determination (R^2)	0.9718	0.942	0.9248	0.9286	0.9438	0.9619	0.8983
Coefficient of linear correlation (r)	0.986	0.971	0.962	0.964	0.971	0.981	0.948
Trend line's goodness-of-fit ($R^2 \cdot 100\%$)	97.2%	94.2%	92.5%	92.9%	94.4%	96.2%	89.8%
Calculated t-value	16.60	11.40	17.53	19.75	12.96	8.70	10.30
Degrees of freedom (DF = n – 2)	8	8	25	30	10	3	12
Critical t-value for α=0.0005	5.041	5.041	3.725	6.646	4.587	12.941	4.318
Critical t-value for α=0.005						5.841	
Statistical conclusion	H_0 rejected with 99.95% confidence; H_1 accepted					H_0 rejected with 99.50% confidence; H_1 accepted	H_0 rejected with 99.95% confidence; H_1 accepted

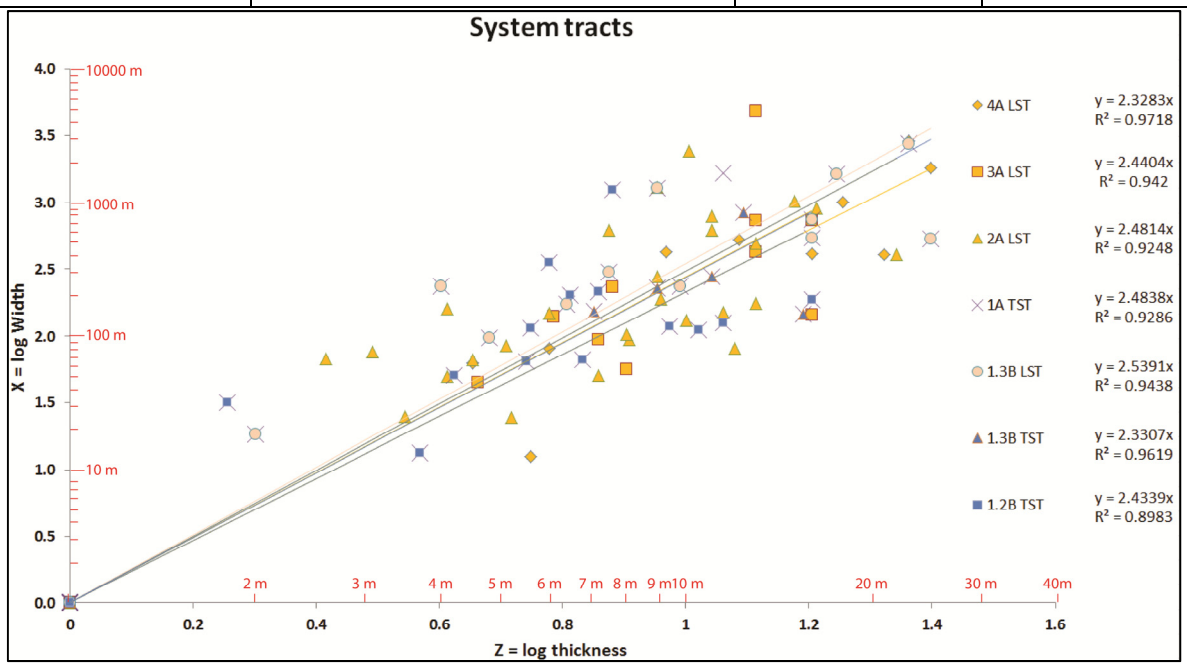

Fig. 5.23. Scatter plot of channel-belt log thickness vs. log width. The data is grouped into the individual system tracts based on the system tracts identified by Keighley et al. (2003): 4A LST, 3A LST, 2A LST, 1A TST, 1.3B LST, 1.3B TST, 1.2B TST. Type A LSTs are shown in orange colour, type A TST is shown with a cross behind the lower order type B system tracts. The type B LSTs are shown with a sandy colour and the type B TSTs are shown with blue colour.

5.4.5 Vertical variation in fluvial channel-belt dimensions

In order to recognize possible stratigraphic upward trends in the channel-belts' cross-sectional dimensions, the depth of the top of each channel-belt was measured relative to the overlying marker horizon M11. The variables considered were the width and thickness of the channel belts, their width/thickness ratio and their approximate cross-sectional area (calculated as width x thickness). A similar approach was taken by Rittersbacher et al. (2013) in a study of the Cretaceous fluvial channel deposits of the Wasatch Plateau.

The data scatter plots (**Fig. 5.24**, left-hand diagrams) appeared to be fuzzy and revealed no obvious, visually-recognizable upward trends. The four datasets were therefore averaged for 10-m stratigraphic intervals (**Fig. 5.24**, right-hand diagrams), which allowed recognition of some hypothetical trends by removal of the noise created by the range of channel sizes at any given point in the succession. Rittersbacher et al. (2013) visually interpreted similar trends, without testing their statistical significance. In order for more objective interpretations to be made, the hypothetical upward trends were statistically evaluated using the Spearman rank-correlation coefficient combined with the Fisher test of its significance (see methods in Chapter 3). A summary of the statistical evaluation is given in **Table 5.14**. Negative r_s values indicate increasing value upwards trends, positive values indicate decreasing value upwards trends. Trends that are tested to be within <85% significance level are labelled non-significant.

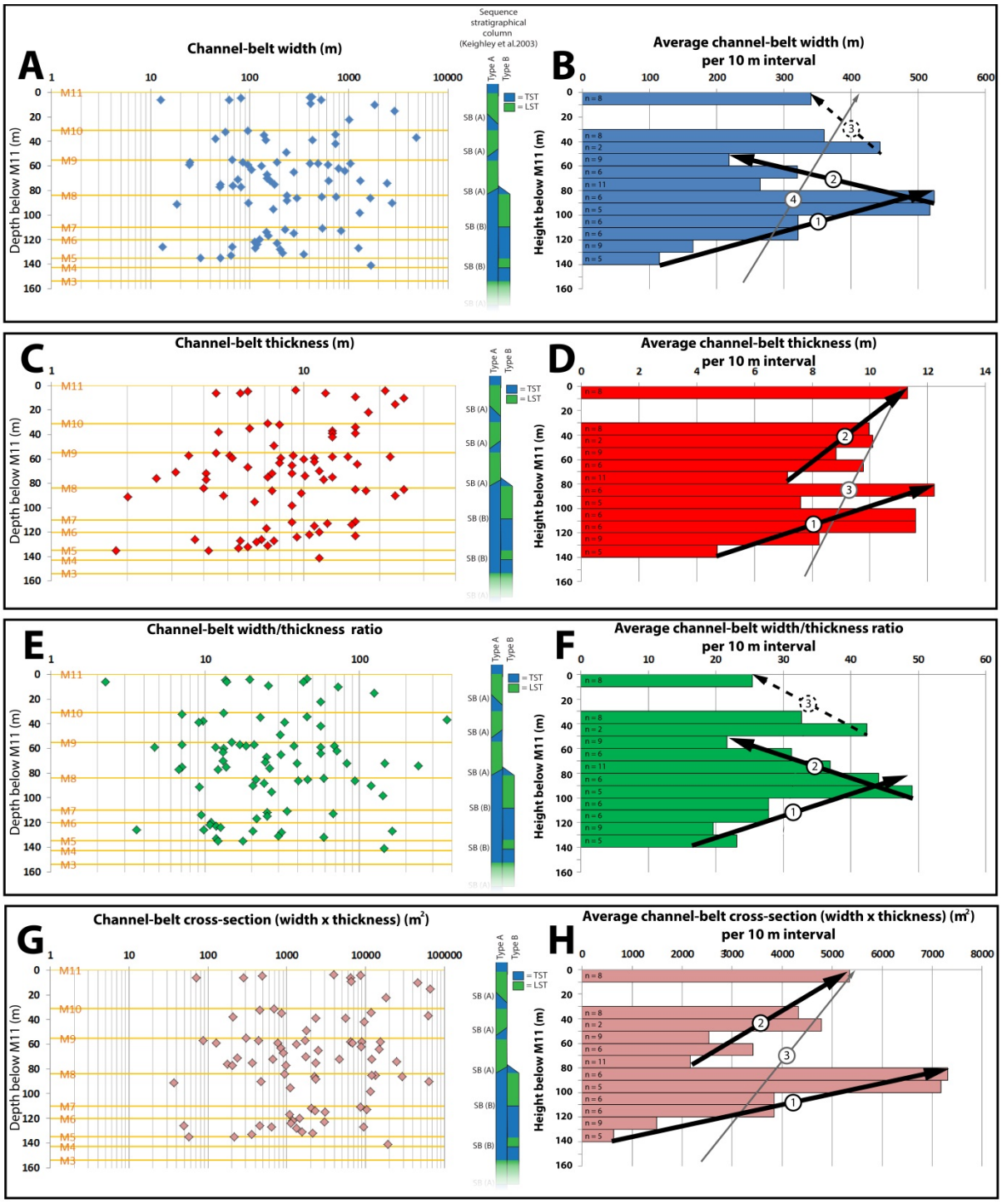

Fig. 5.24 Scatter plots showing channel-belts (**A**) width (**C**) thickness (**E**) width/thickness ratio (**G**) width x thickness relative to a local datum, the M11 marker. Bar charts showing average values for every 10 m interval, (**B**) width (**D**) thickness (**F**) width/thickness ratio (**H**) width x thickness relative to a local datum, the M11 marker. Black arrows indicate local trends, stippled arrows indicate non-significant trends, and thin grey arrows indicated trends for the entire interval. The sequence-stratigraphic column of Keighley et al. (2003) is shown between scatter plots and the corresponding bar charts.

Trends are observed for all the variables in the lowermost interval and show increasing-upwards trends from M5 marker and up to the M8 marker (**Fig. 5.24BDFH,** trends labelled 1). They range in confidence level from 95%, for the channel-belt width/thickness ratio variable, to 99.5% confidence level, for the channel-belt width variable (**Table 5.14**). Corresponding degrees of determination (R^2) range from 11.2% to 24.4%. Meaning the change in channel-belt variable values are determined in 11.2-24.4% by the channel-belt's stratigraphic position and 75.5 - 88.8 % by other factors.

Above the M8 marker there is a rapid decrease of both channel-belt thickness and width/thickness. The decrease is especially abrupt for the channel-belt cross-section area with average area dropping from ~7000 m^2 to ~2000 m^2 (**Fig. 5.24H**). While for the width and width/thickness ratio there is a more gradual decrease (**Fig. 5.24BF**, trends 2). Both the channel-belt thickness and their cross-sectional area show a new, significant increasing-upwards trend from the M8 to the M11 marker (**Fig. 5.24DH** trends 2). Although both the confidence levels of the trends and their degree of determination are significantly lower than the trends observed in the lower interval (**Fig. 5.24DH** trends 1).

In the uppermost interval there are visual decreasing-upwards trends observed in both the channel-belt width and width/thickness bar diagrams (**Fig. 5.24BF** trends 3), but Fisher tests conclude that these are not statistically significant (**Table 5.14**).

There are overall increasing-upwards trends for the channel-belt width, thickness and cross-sectional area (**Fig. 5.24B** trend 4, **DH** trends 3). The width and cross-sectional trends have similar confidence levels (85% and 90%), while the thickness trend has a notably higher confidence of 97.5% and a degree of determination (R^2) of 5.2%. There are no significant overall trends for the width/thickness ratio (**Table 5.14**).

The implication of these observations is discussed in the following chapter.

Table 5.14. Statistical evaluation of visually-recognized stratigraphic trends in channel-belt cross-sectional dimensions **(Fig. 5.24)**.

VARIABLE changing with stratigraphic height	**Visual assessment of stratigraphic trends**			**Statistical evaluation of the hypothetical trends**		
	Suspected upward trend	**Depth interval** relative to MM11	**Hypothesis**	**Spearman rank-correlation coefficient**	**Result of the Fisher test**	**Degree of determination (R^2)**
Channel-belt width (Fig. 5.19A-B)	Trend 1 in Fig. 5.19B	140–80 m	Increasing-upwards trend	r_s = -0.4935	Trend significant at 99.5% confidence level	24.4%
	Trend 2 in Fig. 5.19B	90–50 m	Decreasing-upwards trend	r_s = 0.2034	Trend significant at 85% confidence level	4.1%
	Trend 3 in Fig. 5.19B	50–0 m	Decreasing-upwards trend	r_s = 0.1256	Non-significant trend	---
	Trend 4 in Fig. 5.19B	Total interval	Increasing-upwards trend	r_s = -0.1219	Trend significant at 85% confidence level	1.5%
Channel-belt thickness (Fig. 5.19C-D)	Trend 1 in Fig. 5.19D	140–80 m	Increasing-upwards trend	r_s =-0.4286	Trend significant at 97.5% confidence level	18.4%
	Trend 2 in Fig. 5.19D	80–0 m	Increasing-upwards trend	r_s =-0.2583	Trend significant at 95% confidence level	6.67%
	Trend 3 in Fig. 5.19D	Total interval	Increasing-upwards trend	r_s = -0.2278	Trend significant at 97.5% confidence level	5.2%
Channel-belt width/thickness ratio (Fig. 5.19E-F)	Trend 1 in Fig. 5.19F	140–80 m	Increasing-upwards trend	r_s = -0.3343	Trend significant at 95% confidence level	11.2%
	Trend 2 in Fig. 5.19F	100–50 m	Decreasing-upwards trend	r_s = 0.2420	Trend significant at 90% confidence level	5.9%
	Trend 3 in Fig. 5.19F	50–0 m	Decreasing-upwards trend	r_s = 0.0959	Non-significant trend	---
		Total interval	Increasing-upwards trend	r_s = -0.0691	Non-significant trend	---
Channel-belt cross-section area (Fig. 5.19G-H)	Trend 1 in Fig. 5.19H	140–80 m	Increasing-upwards trend	r_s = -0.4712	Trend significant at 99.5% confidence level	22.2%
	Trend 2 in Fig. 5.19H	80–0 m	Increasing-upwards trend	r_s = -0.1522	Trend significant at 85% confidence level	2.3%
	Trend 3 in Fig. 5.19H	Total interval	Increasing-upwards trend	r_s = -0.1538	Trend significant at 90% confidence level	2.4%

5.4.6 Variation in sandbody dimensions in strike direction

Inside the study area there is a visually observed trend towards more amalgamated sandbodies towards the east. This trend was also observed by Remy (1991). In order to test the presence of lateral trends in the sandbodies cross-sectional dimensions in a depositional strike direction, a reference datum was set at Gate Canyon, which is the western most point of the Virtual Outcrop. The distance from each individual sandbody to this reference was measured by calculating the difference between the longitudal position of the middle of each sandbody and the longitudal position of Gate Canyon.

The variables considered were the width and thickness of the channel belts, their width/thickness ratio and their approximate cross-sectional area (calculated as width x thickness). Some visually recognizable trends may be seen on the scatter plots (**Fig. 5.25ABEF**), but they appear fuzzy and therefore the datasets were averaged for 500 m longitudal intervals to better identify visually hypothetical trends (**Fig. 5.25CDGH**).

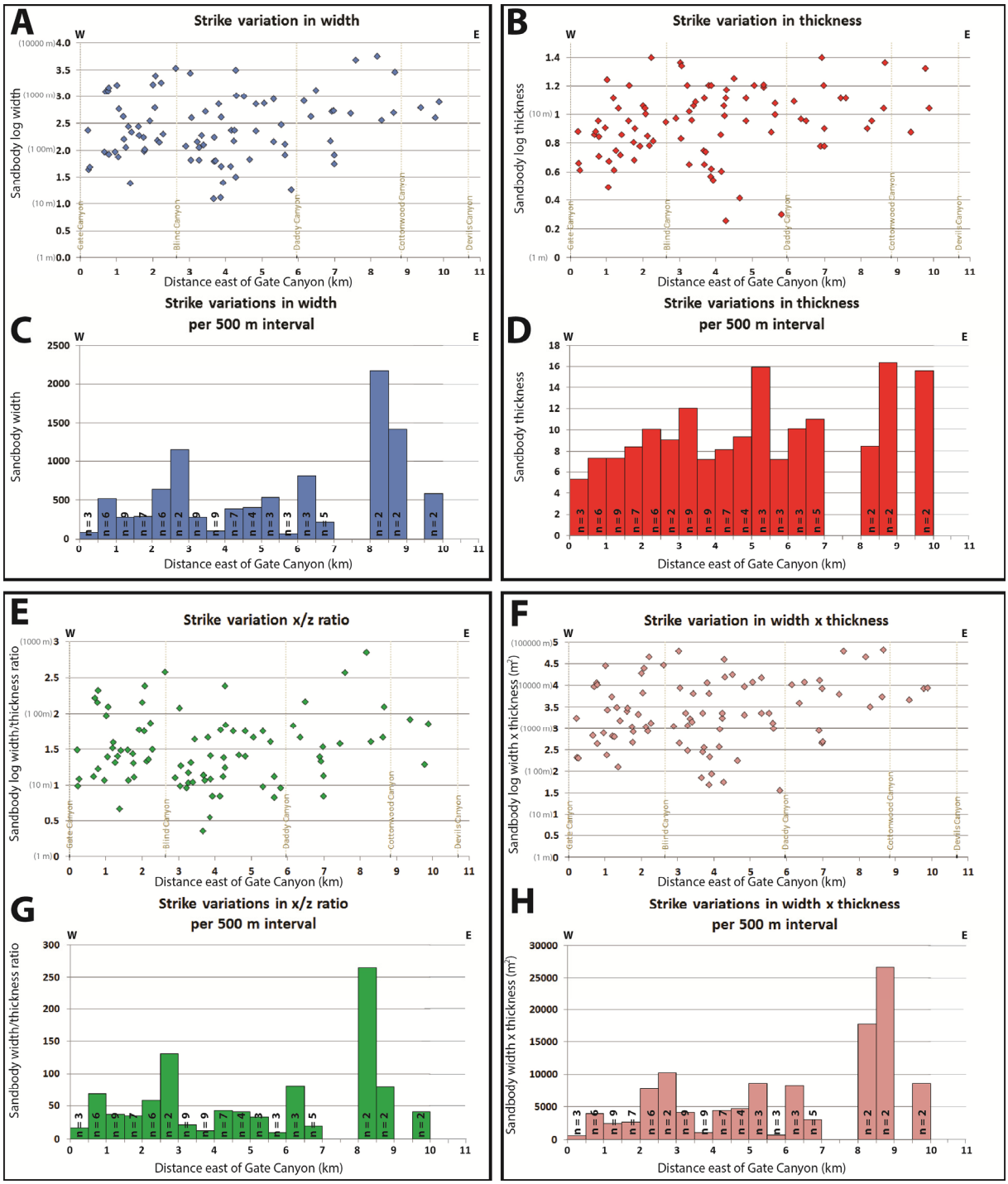

Fig. 5.25. Scatterplots showing variations sandbody dimensions in the depositional strike direction of the Sunnyside Delta interval in the Nine Mile Canyon, between Gate Canyon and Devil Canyon. Along with associated histograms showing average values for each 500 m interval. (**AC**) Width (**BD**) Thickness (**EG**) Width/thickness ratio (**FH**) Cross-sectional area of the sandbodies

The sandbody width plots shows that the widest sandbodies are located in the eastern part of the study area. It also shows two smaller peaks ~2 – ~3 km and ~5 – ~6 km east of Gate Canyon (**Fig. 5.25C**).

Thicknesses generally increase eastwards with the highest values centred around 9 km east of Gate Canyon. Also has minor peaks ~3 km and ~5 km east of Gate Canyon (**Fig. 5.25D**).

The width/thickness and width x thickness plots also show the largest values in the east of the study area, with minor peaks located around ~2 - ~3 km and ~5 - ~6 km west of Gate Canyon (**Fig. 5.25GH**).

Some of the above mentioned trends may be attributed that the lower sequences of the interval pass into the subsurface eastwards in the study area (**Fig. 5.26**).

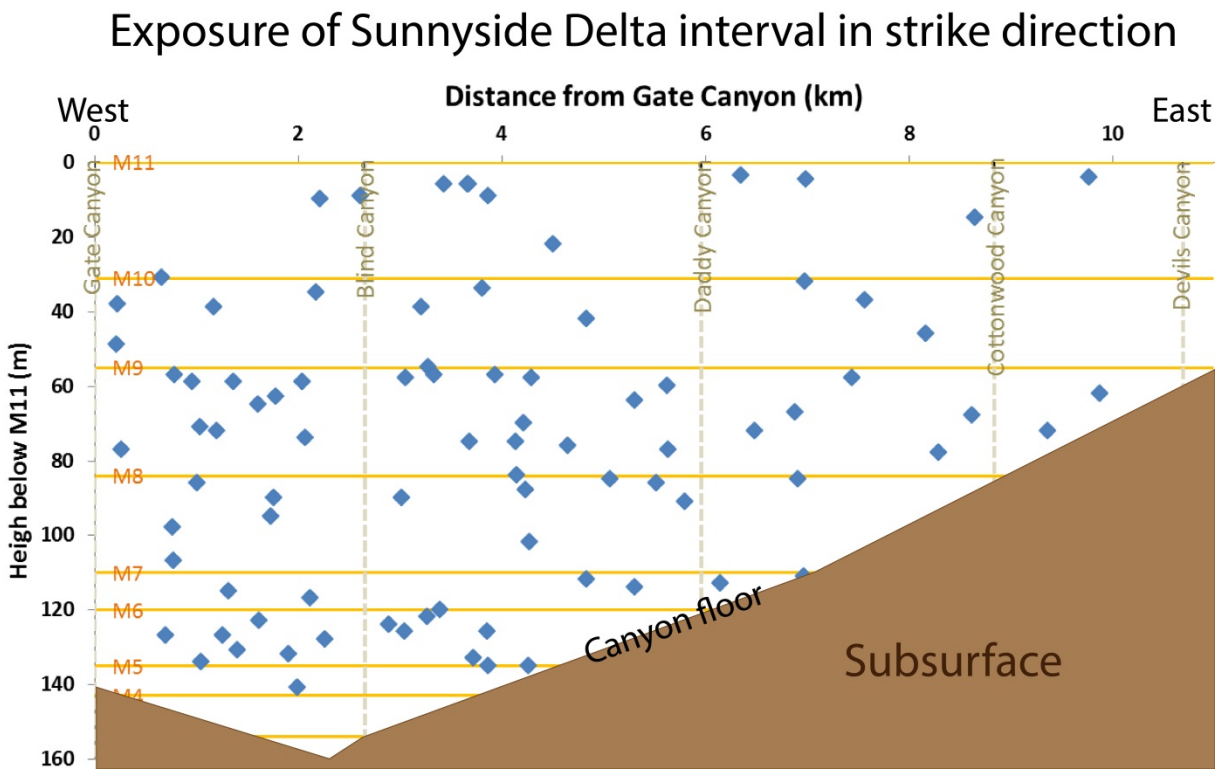

Fig. 5.26. Exposure of the Sunnyside Delta interval in the Nine Mile Canyon between the junction of Gate Canyon in the west and Devils Canyon in the East. Blue dots are location of measured sandbodies (with exposed margins) in height below M11 and distance from Gate Canyon. The Sunnyside Delta interval is gently dipping down into the subsurface in the eastward direction.

6 Discussion

6.1 Delta Morphology

Keighley (2013) argued that the Sunnyside Delta was most likely a wave dominated delta based on the presence of the carbonate ooid grainstone that originated in high energy lacustrine shorefaces. This study agrees that the presence of ooid grainstones has implications for understanding the delta morphology. These are deposited at times of clastic sediment starvation, either when increased accommodation space has shifted the shoreline landward or when a major delta avulsion has shifted the delta laterally. Their presence indicates high wave energy, but does not necessarily mean it was sufficient enough to be the controlling factor of delta morphology.

In the current study the Sunnyside Delta is interpreted as a more fluvial dominated delta with some wave influence, similarly as Moore et al. (2012) and Schomacker et al. (2010). This is interpretation is based on the absence of well-developed siliciclastic shoreface deposits in the Sunnyside Delta interval as opposed to the syndepositional wave dominated delta described by Taylor and Ritts (2004) near Raven Ridge in the NE Uinta Basin, which had a well-developed siliciclastic shorefaces. The presence of large mouthbars with palaeocurrents towards the south, away from Lake Uinta, also points towards “bird foot” morphology of the delta. The coexistence of wave dominated deltas on the lake’s northern shore and fluvial dominated deltas on the lake’s southern shore is attributed the different depositional gradients on the two margins, steep in the north and gentle in the south. The southern shore favoured development of fluvially dominated deltas for two reasons: (1) Wave energy was attenuated as it passed over the shallow lake bed; (2) the shallow lake gradient limited accommodation. Even though the sediment flux was greater on the northern margin than on the southern this allowed deltas on the southern margin to prograde into the lake faster than their northern counter-parts, limiting wave reworking. A similar coexistent relationship is found in the modern Lake Turkana (see section 4.5).

6.2 Spatial Pattern of Channel Direction and Sinuosity

The collected palaeocurrents indicate a mean direction of the sandbodies in the Sunnyside Delta interval is towards 005° (N). This is consistent with previous research that states the Sunnyside Delta was building northwards from the east-west trending southern shoreline of Lake Uinta (Remy, 1991). The palaeocurrents show a distributive pattern, which may indicate deposition in a distributive fluvial system (DFS) *sensu* Weissmann et al. (2010). Roux's (1992) method for calculating channel sinuosity suggests an average sinuosity in the interval of 1.87, which indicates mature meandering channels and therefore a very low gradient. Although the number of data points was limited and more field work is required to collect a more representative amount of palaeocurrent data for each of the individual units. Large differences in sinuosity were observed between channels, e.g. in the U5 interval the channels look generally quite straight, isolated in a floodplain matrix. Channels generally decrease in sinuosity downstream in the lower part of a DFS system, therefore these channels may reflect channels deposited in a distal location on a DFS, while the more sinuous channels represents deposition in a more proximal setting.

6.3 Sandbody Geometry

6.3.1 Bulk dataset

The sandbodies of the Sunnyside Delta interval have a mean thickness of ~9 m, with a relatively low standard deviation (~3.5 m), the mean width is ~392 m with a high standard deviation (~445 m). The high standard deviation within the widths is attributed to three main factors; (1) the variable maturity of the sandbodies when they are abandoned by avulsion, (2) variable rate of aggradation (3) the bulk dataset is a mixture of sandbodies deposited by different mechanisms. The last factor was investigated further by grouping the bulk-dataset up into sub-groups (section 5.4.2), this significantly reduced the standard deviation of the width relative to the mean width from the bulk datasets 113% to 44% – 75% for the sub-groups. The three factors above are estimated to account for 7.3% of the "noise" in the bulk data set (1 - R^2 x 100), and between 2.3 – 7.3% for the sub-groups.

6.3.2. Sandbody types

For the sandbody type datasets the relative dimensions between the types were; multi-storey channel-belts were generally thicker and wider than single-storey channel-belts and multilateral channel-belts wider and thicker than unilateral channel-belts. It is interesting to note how similar the width/thickness ratios are between the two unilateral groups (16.7-17) and the two multilateral groups (75.2-89.5).

Multi-storey multilateral channel belts -- Multi-storey multilateral channel belts are believed to have formed during periods of long lasting lake still-stand that has followed a period of lake level fall (LST). The relatively low standard deviation of channel-belt width relative to the channel-belt mean width (44%) reflects the channel belts having been able to evolve into a mature state where channel-belt width increases at a lower rate than for sub-mature channel-belts (**Fig. 5.1**). The high width and thickness also reflects proximal deposition on a DFS system, where channel-belts are generally wider and thicker.

Multi-storey unilateral channel-belts -- The low standard deviation of the channel-belts width relative to the channel-belt mean width (38%) to the multi-storey unilateral channel-belts suggests that they have been subjected to some degree of lateral confinement. During periods of lake level fall, rivers may have cut small incisions, which if followed by a period of lake level rise is first filled by multi-storey unilateral channel-belts and then capped by deposits with a progressively lakeward shift in facies. This theory is strengthened with observations in the U6 interval where a multi-storey unilateral channel-belt is overlain by mouthbar deposits (**Fig. 6.1**).

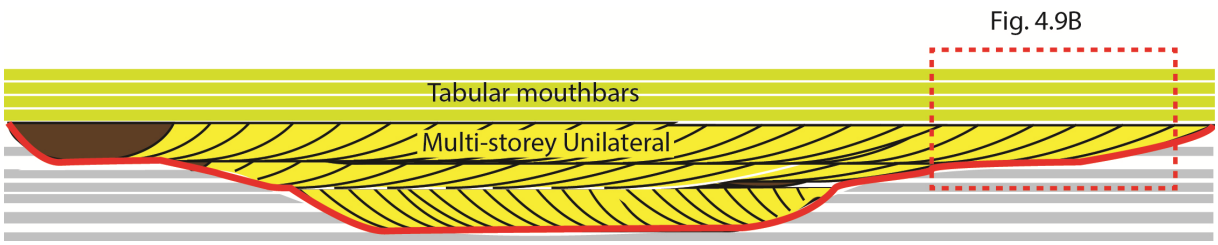

Fig. 6.1. Multi-storey unilateral channel-belt. Laterally confined by incision, caused by short lived lake level fall. Overlaid by tabular mouthbars as observed in the U6 interval in **Fig. 4.9B**.

Single-storey multilateral channel belts -- Unconfined channel-belts that form during lake level still-stand. Channel-belts are relatively mature.

Single-storey unilateral channel belts -- Channel-belts that have formed during lake level rise. Not allowing the channel to migrate laterally for a longer period of time and therefore being sub-mature.

The relatively high standard deviation (61%) may be attributed low maturity of the channel-belts. During early stages of channel-belt formation the channel-belts expand at a higher pace than mature channel-belts.

The lowest coefficient of determination of the sub-datasets belongs to the single-storey unilateral channel-belts; this may be attributed to some extent of a mixture of proverbial apples and oranges – the single-storey unilateral group hosts both non-laterally migrating sand filled channel scours and laterally migrating channel-belts (**Fig. 6.2**). By segregating these sandbodies the coefficient of determination would most likely increase.

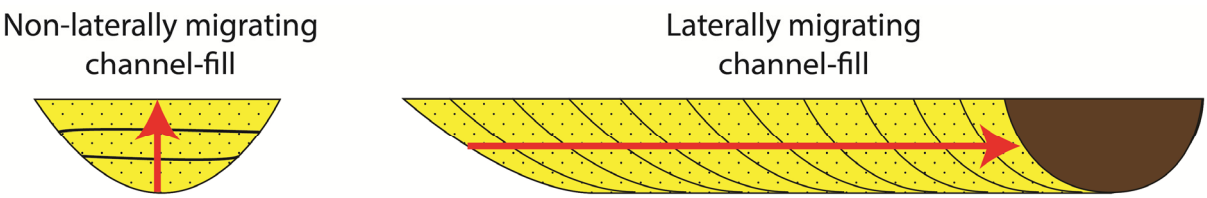

Fig. 6.2. Variety of sandbodies within the single-storey unilateral group.

Mouthbar sandbodies -- The measured mouthbars have the widest mean width of all the sub-groups, almost 2000 m. They have a markedly higher width/thickness ratio of ~220. This is because the thickness of mouthbars is dependent upon the depth of the lake water, rather than the feeder-channel incision, although the later may depend on the former. The mouthbar width will depend more on the time of progradation than on the feeder-channel depth or width.

6.3.3 Palaeo-channel dimensions

The measured abandonment plugs gives dimensions on palaeo-channel bankfull width. Their thickness also gives dimensions on the depth of the palaeo-channels, although this is a minimum width, since there most often is some degree of channel-fill before total abandonment and deposition of the abandonment plug (**Fig. 6.3**). The mean value of single-storey channel-belts are therefore used as an approximated palaeo-depth (~6.8 m). Channel parameters are estimated from the bankfull depth and width with the use of the equations

from Williams (1986) and Collinson (1978) given in **Table. 5.1 (Table 6.1**). The estimated mean bankfull width (282 m) is 4.6 times greater than the measured bankfull width from the abandonment plugs (61 m), and well outside the standard deviation range given by Williams (1986). Hence the estimated values are not believed to be representative for the Sunnyside Delta interval or the measured abandonment plug widths are not representative for the palaeo-channels of the interval.

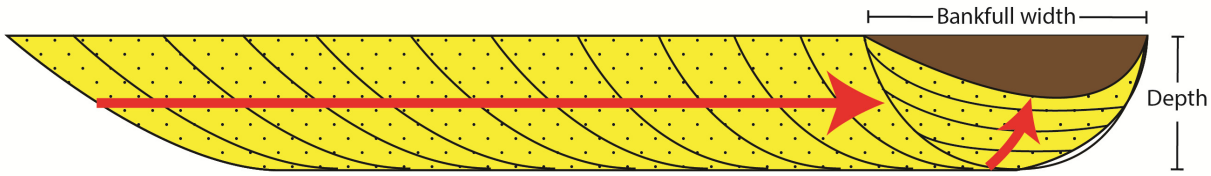

Fig. 6.3. Abandonment plug thickness gives only a minimum bankfull depth of the palaeo-channel, since channel abandonment may be gradual. Arrows indicate sediment accretion direction.

Table 6.1. Estimation of meandering-river channel-belt dimensions. Using formulae from (Williams, 1986) and (Collinson, 1978) given in **Table 5.1**.

Reference no.	Parameter	Value	Unit
1	Meander wavelength, Lm	4422	m
2	Along-channel bend length, Lb	2948	m
3	Mean bankfull channel width, Wc	282	m
4	Meander-belt width, Wm	1530	m
5	Channel-bend radius of curvature, Rb	774	m
6	Channel sinuosity, S	3.37	m
7	Mean annual discharge, Q	850	ft/sec

The narrower and less sinuous channel-belts observed relative to the estimated values from Williams (1986) may be explained by the distributive fluvial system concept, were channels generally decrease in sinuosity and size downstream (Weissmann et al., 2010).

6.3.4 Exceedence frequency plots

The exceedence frequency (EF) plots have proven to be more useful than probability density curves in revealing the distribution-type of the datasets and displaying the de-cumulative probability density of the variables. All measured sandbody dimensions have revealed lognormal distributions, meaning they cannot be represented by Gaussian formulae for the

statistical parameters; mean, standard deviation and variance, as is commonly done. Instead special formulae (Wilks, 1995) have to be used to transform the geometric statistical parameters into arithmetic values. The supplements of an *n*-amount of dummy values {X=0, Z=0} has proven successful in creating more realistic trend lines by forcing the linear regression through the physically requirement; width = 0 when thickness = 0 and vice versa.

6.4 Stratigraphic Trends

6.4.1 Vertical datum

Grouping the channel-belts into 10 m bins vertically is a useful way to consider vertical trends and reduce the impact of the natural range of channel body dimensions at any given time slice (Rittersbacher et al., 2013). Visual examination of the data suggest two higher order cycles within the study interval, with channels getting progressively larger up to 100 m below the datum, then smaller to around 60 m below the datum and then larger again (**Fig. 5.24**).

Rittersbacher et al. (2013) used an upward increase in channel dimensions to define progradation of a DFS, while Cain and Mountney (2009) used similar changes in dimensions to recognise a retrogradational DFS where there is a downstream decrease in fluvial discharge, channel width and depth, sinuousity, and an increase in channel bifurcation.

Following these criteria the lower interval, up to the M8 marker may document a progradational DFS system (**Fig. 5.24**, right hand diagrams, trends labelled 1). This is based on observations of increase in both: width, thickness, width/thickness ratio and channel-belt cross sectional area (width x thickness). There is insufficient palaeocurrent data to fully calculate sinuosity for the different vertical intervals, but visually there seems to be a trend from fairly straight channels in the U5 interval and increase upwards to the more sinuous channel-belts of the U7 interval. This is in contrast with the stratigraphic interpretation of Keighley et al. (2003), in which the interval is interpreted as a type A transgressive systems tract. In the present study it is instead re-interpreted as a lowstand systems tract.

In the U8 interval the cross-sectional area of the channel-belts (width x thickness) suggests a rapid flooding and retreat of the distributary fluvial system around the M8 carbonate

marker, before an onset of a new stage of delta progradation (**Fig. 5.24H**, trend 2). This interpretation is however not consistent with the presence of the thin oil shale layer (Facies Los) underlying the M9 carbonate marker, which marks a maximum flood surface. Alternatively it may document a retrogradational distributive fluvial system, based on the progressively decrease in width/thickness ratio upwards (**Fig. 5.24F**, trend 2). The latter interpretation is supported by the maximum flooding surface underlying the M9 carbonate marker, and is therefore favoured. This interpretation implies another re-interpretation of Keighley et al. (2003) systems tract; the U8 interval originally attributed to a LST is re-interpreted as a TST.

From the maximum flooding surface (M9) and up to the top of the interval (M11), there are no significant trends for the widths and width/thickness ratio, while the channel-belt thicknesses show a thickening trend. Observations from the Virtual Outcrop show that the U9 interval has the highest presence of mouthbar sandbodies of all the intervals, while the sandbodies of the U10 interval are interpreted as purely fluvial (**Table 5.10**). Based on this upwards landward shift in facies, the interval is interpreted to have formed during a further phase of progradation of the Sunnyside Delta.

All the describe trends above are significant within an 85% confidence level. The increasing trend up to the M8 marker has the highest degree of determination (R^2 = 24.4% for the channel-belt width trend), the trends above the M8 marker have significantly lower degrees of detmination (R^2). The deviations from perfect trends (R^2 = 100%) is attributed the variable maturity of the channel-belts between avulsion.

The large variation of channel-belt width and thickness stratigraphically demonstrates the importance of understanding the sequence stratigraphical framework when predicting channel-belt dimensions distribution in e.g. a reservoir model.

6.4.2 Sequences

Since the results found when investigating the vertical variation of channel-belt dimensions (section 5.4.5) show evidence of higher order sequences than the ones described by Keighley et al. (2003) this supports the interpretations of Moore et al. (2012) that the sequences are better described as upward shoaling parasequences, bounded by flooding surfaces (Van

Wagoner, 1988). These new higher order sequences, here conveniently labelled seq. X and seq. Y, are bounded by the first fluvial incision surface above a maximum flooding surface, interpreted to be a correlative conformity surface down-dip of an unconformity.

The suggested re-interpreted parasequences 1.2B and 1.3B forms a progradational parasequence set, 2A a retrogradational parasequence, 3A and 4A a progradational parasequence set (**Fig. 6.4**).

6.4.3 System tracts

All the systems tracts of Keighley et al. (2003) except the TST 1A systems tract, are re-interpreted as lower order, parasequence, systems tracts (**Fig. 6.4**). By re-interpreting the sandbodies of the U8 interval to be mainly deposited during a TST interval a clear trend for channel-belt dimensions relative to systems tracts is found; all mean width values from TST dominated intervals are in the range ~145 m - ~310 m with corresponding mean thicknesses in the range ~6.9 m - ~10.8 m and width/thickness ratios between ~20 and ~29.4, while the mean channel-belt width values from LST dominated intervals are in the range ~380 m - ~552 m with mean thickness values in the range ~10 m - ~12.9 m and width/thickness ratios between ~34.8 and ~45.

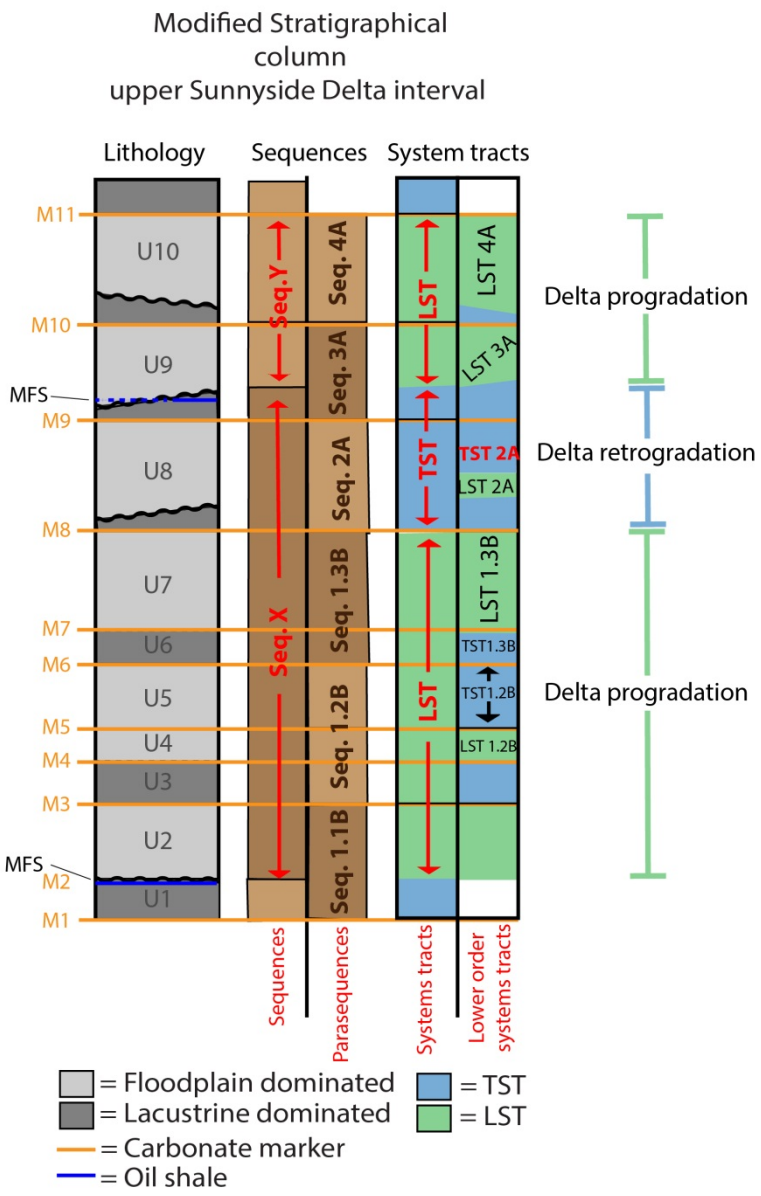

Fig. 6.4. Modified stratigraphic column based on channel-belt stratigraphical trends. Red text indicates suggested changes.

6.5 Horizontal Variability

When plotting sandbody cross-sectional dimensions versus the east-west trending depositional strike direction, several visually recognizable trends are found (**Fig. 5.25**). By using the same concepts used in section 6.4.1, where increasing sandbody width, thickness, width/thickness and width x thickness values reflect moving from a distal setting on a distributive fluvial system to a more proximal setting, the trends may reveal the lateral position of the Sunnyside Delta.

One obvious trend is found in the interval between Gate Canyon (0 km) and Blind Canyon (~2.5 km). In this range there is an increase in both width, thickness, width/thickness ratio and width x thickness. This trend may also be seen visually in the Virtual Outcrop (**Fig. 6.5**), where the three uppermost, newly re-interpreted, parasequences pass from massive sandbodies in the east, near Blind Canyon, to isolated small channels in the west, towards Gate Canyon. East of Blind Canyon there is a decrease in both sandbody widths and thicknesses (**Fig. 5.25**). These observations point towards to a local depaxis of a distributive fluvial system located in area around Blind Canyon, during the time of deposition of the U8, U9 and U10 intervals.

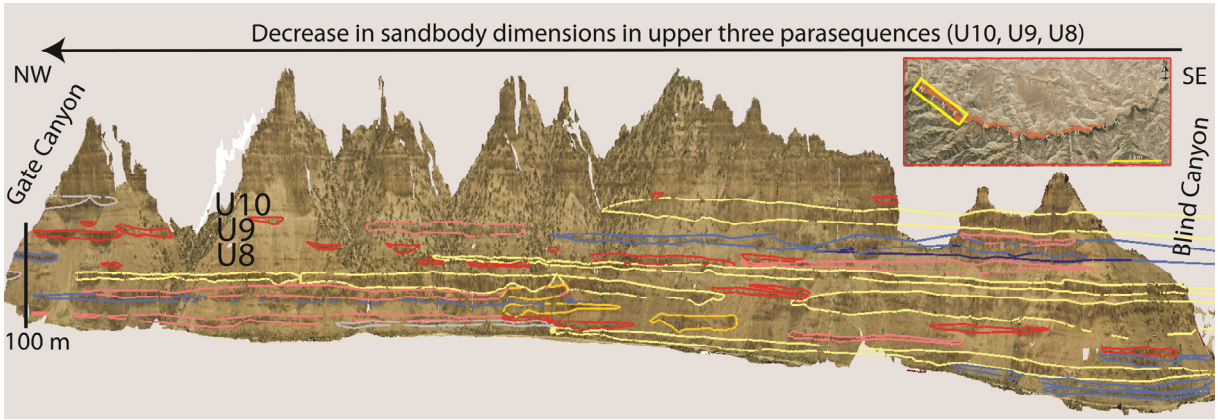

Fig. 6.5. Snapshot of Virtual Outcrop between Gate Canyon and Blind Canyon, showing sandbodies in the uppermost thre parasequences passing from massive sandbodies in the west to small isolated sandbodies in the west. Location is shown in yellow rectangle in embedded map. Exaggerated vertical scale (3x). Outlines of interpreted sandbodies are shown, with colour coding after sandbody types; red = SU, pink = SM, orange = MU, yellow = MM, blue = MB, and grey = undifferentiatied.

There seems also to be an overall increase, across the entire study area, in both sandbody width and thickness eastwards, which matches the observations from the outcrop that the sandbodies get increasingly more amalgamated eastwards. However some of this trend may reflect the stratigraphically upwards increasing trend in sandbody dimensions, since the lower stratigraphical units gradually dip into the subsurface eastwards (**Fig. 5.26**), it may also reflect that the location of the main depaxis of the Sunnyside Delta was located east of the present study area.

7. Conclusions

- Conventional sedimentological logging has allowed distinction of a wide range of sedimentary facies representing various modes of sediment deposition and 12 sub-associations of spatially and genetically related facies representing specific morphodynamic elements of the Green River Formation in the Uinta Basin, including previously unrecognized channel bank-collapse deposits. They jointly form five main facies associations representing particular depositional palaeo-environments, such as an open-water lacustrine system, a lacustrine shoreface system, a deltaic mouthbar system, a fluvial channel-belt system and an alluvial delta-plain system.
- On the basis of the recognised facies associations and their spatial organization, the studied stratigraphic interval is interpreted to have recorded the depositional history of an arid to semi-arid lacustrine deltaic system, building out into a large shallow-water lake. The low gradient delta topography allowed the delta to rapidly prograde at a higher pace than it could be reworked by waves, resulting in a “bird foot” morphology of the delta. High fluctuations in lake level combined with a low gradient of the delta caused frequent and extensive flooding of the delta, during which shallow lacustrine carbonate grainstones were deposited as stratigraphic marker horizons.
- The sandbodies of the Sunnyside Delta interval have a mean width of ~390 m, a mean thickness of ~9 m, and a mean width/thickness ratio of ~39. The width variance and thereby also the width/thickness ratio variance are both high. This is attributed to three main causes (1) the variable maturity level of the channel-sinuosity development at the stage of channel avulsion (2) the variable rate of channel aggradation (3) a mixture of sandbodies deposited by different mechanisms. The role of the last factor was investigated further by dividing the bulk data-set according to the sandbody type: multi-storey multilateral channel-belts, multi-storey unilateral channel-belts, single-storey-multilateral channel-belts, single-storey unilateral

channel-belts and mouthbar sandbodies. This grouping significantly reduced the variance in both sandbody width and thickness.

- The mean palaeo-channel bankfull width estimated from 14 measured abandonment plug widths is ~61 m, and the mean bankfull palaeo-channel depth has been estimated from 49 measured single-storey channel-belts is ~6.8 m.
- Exceedence frequency plots have proven to be a robust tool for both revealing distribution type of a dataset and for estimating sandbody width based on known sandbody thicknesses.
- Statistical analysis of sandbody width and thickness data reveals that both variables have a log-normal distribution. The main implication of this is that the variables basic statistical parameters; mean, standard deviation and variance cannot be obtained using conventional Gaussian formulae, instead special formulae have to be used to transfer the logarithmic statistical parameters into arithmetic values. Many studies of sandbody geometry are based on Gaussian statistics and their conclusions are therefore questionable.
- Most if not all previous studies on sandbody width/thickness ratios have trendlines that when extrapolated to not cross the physical required point of width = 0 then thickness = 0 or vice versa. The supplement of *n*-amount of dummy values {width = 0, thickness = 0}, as shown in this study, forces the linear regression line through this physical requirement and results in a more realistic trendline.
- An analysis of stratigraphic variations in channel-belt width, thickness, width/thickness ratio and width x thickness area in Sunnyside Delta interval has revealed two progradational phases of a distributive fluvial system and separated by a retrogradational phase.
- Based on the interpreted progradational and retrogradational intervals, two higher order sequences are inferred, which supports the suggested re-interpretation of the sequences of Keighley et al. (2003) as parasequences, as suggested by Moore et al. (2012), forming two progradational parasequence sets and one retrogradational parasequence.

- The U8 interval of Keighley et al. (2003), originally attributed to a lowstand systems tract, is re-interpreted as a transgressive systems tract. In the present interpretation, there is a distinct trend towards narrower and thinner channel-belts within transgressive systems tracts, and wider and thicker channel-belts within lowstand systems tracts.
- Analysis of the sandbody dimensions along the depositional strike direction has revealed an overall eastward increase in sandbody dimensions within the studied stratigraphic interval, which suggests the location of a main distributive fluvial system's depaxis to the east of the present study area. Smaller scale variability in sandbody dimensions in the depositional strike direction has also revealed a local depocenter in the area around the junction between the Nine Mile Canyon and the Blind Canyon.

References

Bellian, J., Kerans, C., and Jennette, D., 2005, Digital outcrop models: applications of terrestrial scanning lidar technology in stratigraphic modeling: Journal of Sedimentary Research, v. 75, p. 166-176.

Bradley, W. H., 1931, Origin and microfossils of the oil shale of the Green River Formation of Colorado and Utah: USGS Numbered Series, v. 168, p. 58.

Bridge, J. S. J., 2003, Rivers and Floodplains : Forms, Processes, and Sedimentary Record, Oxford, Blackwell Publishing Company, 491 p.:

Buckley, S. J., Howell, J., Enge, H., and Kurz, T., 2008, Terrestrial laser scanning in geology: data acquisition, processing and accuracy considerations: Journal of the Geological Society, v. 165, p. 625-638.

Cain, S. A., and Mountney, N. P., 2009, Spatial and temporal evolution of a terminal fluvial fan system: the Permian Organ Rock Formation, South-east Utah, USA: Sedimentology, v. 56, p. 1774-1800.

Collinson, J., 1977, Vertical sequence and sand body shape in alluvial sequences: Fluvial Sedimentology, v. 5, p. 577-586.

Collinson, J. D., 1978, Alluvial sediments, in Reading, H.G., ed., Sedimentary Environments and Facies, Oxford, Blackwell Science Ltd., 60 p.:

Davies, D. K., Williams, B. P., and Vessell, R. K., 1993, Dimensions and quality of reservoirs originating in low and high sinuosity channel systems, Lower Cretaceous Travis Peak Formation, East Texas, USA: Geological Society, London, Special Publications, v. 73, p. 95-121.

Davis, J. C., 2002, Statistics and Data Analysis in Geology, New York, John Wiley & Sons, 656 p.:

Dickinson, W. R., Klute, M. A., Hayes, M. J., Janecke, S. U., Lundin, E. R., McKITTRICK, M. A., and Olivares, M. D., 1988, Paleogeographic and paleotectonic setting of Laramide sedimentary basins in the central Rocky Mountain region: Geological Society of America Bulletin, v. 100, p. 1023-1039.

Dickinson, W. R., and Snyder, W. S., 1978, Plate tectonics of the Laramide orogeny: Geological Society of America Memoir, v. 151, p. 355-366.

Drummond, C. N., and Wilkinson, B. H., 1996, Stratal thickness frequencies and the prevalence of orderedness in stratigraphic sequences: Journal of Geology, v. 104, p. 1-18.

English, J. M., and Johnston, S. T., 2004, The Laramide Orogeny: what were the driving forces?: International Geology Review, v. 46, p. 833-838.

Fabuel-Perez, I., Hodgetts, D., and Redfern, J., 2009, A new approach for outcrop characterization and geostatistical analysis of a low-sinuosity fluvial-dominated succession using digital outcrop models: Upper Triassic Oukaimeden Sandstone Formation, central High Atlas, Morocco: AAPG bulletin, v. 93, p. 795-827.

Fielding, C. R., 1987, An application of statistical modelling to the prediction of hydrocarbon recovery factors in fluvial reservoir sequences: SEPM special publication, v. 39, p. 321-327.

Fielding, C. R., and Crane, R. C., 1987, An application of statistical modelling to the prediction of hydrocarbon recovery factors in fluvial reservoir sequences: The Society of Economic Paleontologists and Mineralogists, v. SP39, p. 321-327.

Fielding, C. R., Trueman, J. D., and Alexander, J., 2005, Sharp-based, flood-dominated mouth bar sands from the Burdekin River Delta of northeastern Australia: extending the spectrum of mouth-bar facies, geometry, and stacking patterns: Journal of Sedimentary Research, v. 75, p. 55-66.

Fouch, T. D., 1975, Lithofacies and related hydrocarbon accumulations in Tertiary strata of the western and central Uinta Basin, Utah: Rocky Mountain Association of Geologists - 1975 Symposium, p. 163 - 173.

Ghinassi, M., Nemec, W., Aldinucci, M., Nehyba, S., Özaksoy, V., and Fidolini, F., 2014, Plan-form evolution of ancient meandering rivers reconstructed from longitudinal outcrop sections: Sedimentology, v. 61, p. 952-977.

Ghosh, P., 2000, Estimation of channel sinuosity from paleocurrent data: a method using fractal geometry: Journal of Sedimentary Research, v. 70, p. 449-455.

Haack, B., 1996, Monitoring wetland changes with remote sensing: an East African example: Environmental Management, v. 20, p. 411-419.

Jacob, A., 1969, Delta facies of the Green River Formation (Eocene), Carbon and Duchesne Counties, Utah: Ph.D. dissertation, University of Colorado, Boulder.

Janocko, M., Nemec, W., Henriksen, S., and Warchoł, M., 2013, The diversity of deep-water sinuous channel belts and slope valley-fill complexes: Marine and Petroleum Geology, v. 41, p. 7-34.

Johnson, T. C., and Malala, J. O., 2009, Lake Turkana and its link to the Nile, The Nile: Houten, Springer, p. 287-304.

Keighley, D., Flint, S., Howell, J., Andersson, D., Collins, S., Moscariello, A., and Stone, G., 2002, Surface and Subsurface Correlation of the Green River Formation in Central Nine Mile Canyon, SW Uinta Basin, Carbon and Duchesne Counties, East-Central Utah, : Utah Geological Survey MP, v. 2, p. 65.

Keighley, D., Flint, S., Howell, J., and Moscariello, A., 2003, Sequence stratigraphy in lacustrine basins: a model for part of the Green River Formation (Eocene), southwest Uinta Basin, Utah, USA: Journal of Sedimentary Research, v. 73, p. 987-1006.

Keighley, D. a. F., Stephen, Faceis Re-Interpretation of Sunnyside Delta Sandstone in Nine Mile Canyon, Uinta Basin, Utah: the Perils of Model-Driven Geology, *in* Proceedings AAPG Rocky Mountain Section 62nd Annual Meeting, Salt Lake City, Utah, September 22-24, 2013.

Keighley, D. G., and Flint, S. S., 2008, Fluvial Sandbody Geometry and Connectivity in the Middle Green River Formation, Nine Mile Canyon, Southwestern Uinta Basin: Hydrocarbon Systems and Production in the Uinta Basin, Utah, 2008, v. 37, p. 101-119.

Keogh, K. J., Martinius, A. W., and Osland, R., 2007, The development of fluvial stochastic modelling in the Norwegian oil industry: A historical review, subsurface implementation and future directions: Sedimentary Geology, v. 202, p. 249-268.

Le Roux, J., 1992a, Determining the channel sinuosity of ancient fluvial systems from paleocurrent data: Journal of Sedimentary Research, v. 62, p. 283-291.

Le Roux, J. P., 1992b, Determining the channel sinuosity of ancient fluvial systems from paleocurrent data: Journal of Sedimentary Petrology, v. 62, p. 283-291.

Lorenz, J. C., Heinze, D. M., Clark, J. A., and Searls, C. A., 1985, Determination of widths of meander-belt sandstone reservoirs from vertical downhole data, Mesaverde Group, Piceance Creek Basin, Colorado: AAPG Bulletin, v. 69, p. 710-721.

Miall, A. D. A., 1978, Fluvial sedimentology, Calgary, Canadian Society of Petroleum Geologists, 859 p.:

Middleton, G. V., Plotnick, R. E., and Rubin, D. M., 1995, Nonlinear dynamics and fractals, new numerical techniques for sedimentary data: SEPM Short course No.36 Lecture Notes, Society for Sedimentary Geology, tulsa, p.174.

Moore, J., Taylor, A., Johnson, C., Ritts, B. D., and Archer, R., 2012, Facies Analysis, Reservoir Characterization, and LIDAR Modeling of an Eocene Lacustrine Delta, Green River Formation, Southwest Uinta Basin, Utah: Lacustrine sandstone reservoirs and hydrocarbon systems: AAPG Memoir, v. 95, p. 183-208.

Morgan, C. D., 2002, Reservoir Characterization of the Lower Green River Formation, Southwest Uinta Basin, Utah: Utah Geological Survey (US).

Nemec, W., 1990, Aspects of sediment movement on steep delta slopes: Spec. Publs int. Ass. Sediment., v. 10, p. 29-73.

Nemec, W., 2005, Geostatistics: Course GEOV301 Lecture Notes: University of Bergen.

Reading, H., 1996, Sedimentary Environments; Processes, Facies and Stratigraphy, Oxford, UK, Blackwell Science.

Remy, R. R., 1991, Analysis of lacustrine deltaic sedimentation in the Green River Formation, southern Uinta Basin, Utah (abstract only).

Remy, R. R., 1992, Stratigraphy of the Eocene part of the Green River Formation in the south-central part of the Uinta Basin, Utah: Ph.D. dissertation, Louisiana State university and Agricultural and Mechanical College, p. 394.

Rittersbacher, A., Buckley, S. J., Howell, J. A., Hampson, G. J., and Vallet, J., 2013, Fluvial facies and virtual outcrop geology: a novel approach to empirical understanding of fluvial architecture [PhD, 185 p.

Ryder, R. T., Fouch, T. D., and Elison, J. H., 1976, Early Tertiary sedimentation in the western Uinta basin, Utah: Geological Society of America Bulletin, v. 87, p. 496-512.

Schomacker, E. R., Kjemperud, A. V., Nystuen, J. P., and Jahren, J. S., 2010, Recognition and significance of sharp-based mouth-bar deposits in the Eocene Green River Formation, Uinta Basin, Utah: Sedimentology, v. 57, p. 1069-1087.

Shukla, U., Singh, I., Srivastava, P., and Singh, D., 1999, Paleocurrent patterns in braid-bar and point-bar deposits: examples from the Ganga River, India: Journal of Sedimentary Research, v. 69, p. 992-1002.

Taylor, A., and Ritts, B., 2004, Mesoscale heterogeneity of fluvial-lacustrine reservoir analogues: examples from the Eocene Green River Formation and Colton Formations, Uinta Basin, Utah, USA: Journal of Petroleum Geology, v. 27, p. 3-26.

Tye, R. S., 2004, Geomorphology: An approach to determining subsurface reservoir dimensions: AAPG Bulletin, v. 88, p. 1123-1147.

Vallet, J., and Skaloud, J., 2004, Development and experiences with a fully-digital handheld mapping system operated from a helicopter: The International Archives of the Photogrammetry, Remote Sensing and Spatial Information Sciences, Istanbul, v. 35, p. 6.

Van Wagoner, J., 1988, An overview of the fundamentals of sequence stratigraphy and key definitions: Society of Economic Palaeontologists and Mineralogists Special Publication, v. 2, p. 39-45.

Weissmann, G., Hartley, A., Nichols, G., Scuderi, L., Olson, M., Buehler, H., and Banteah, R., 2010, Fluvial form in modern continental sedimentary basins: Distributive fluvial systems: Geology, v. 38, p. 39-42.

Wilks, D. S., 1995, Statistical Methods in Atmospheric Sciences: An Introduction, San Diego, Academic Press, 315 p.:

Williams, G. P., 1986, River meanders and channel size: Journal of Hydrology, v. 88, p. 147-164.

Zervas, D., Nichols, G. J., Hall, R., Smyth, H. R., Lüthje, C., and Murtagh, F., 2009, SedLog: A shareware program for drawing graphic logs and log data manipulation: Computers & Geosciences, v. 35, p. 2151-2159.

Appendix

Sedimentary logs

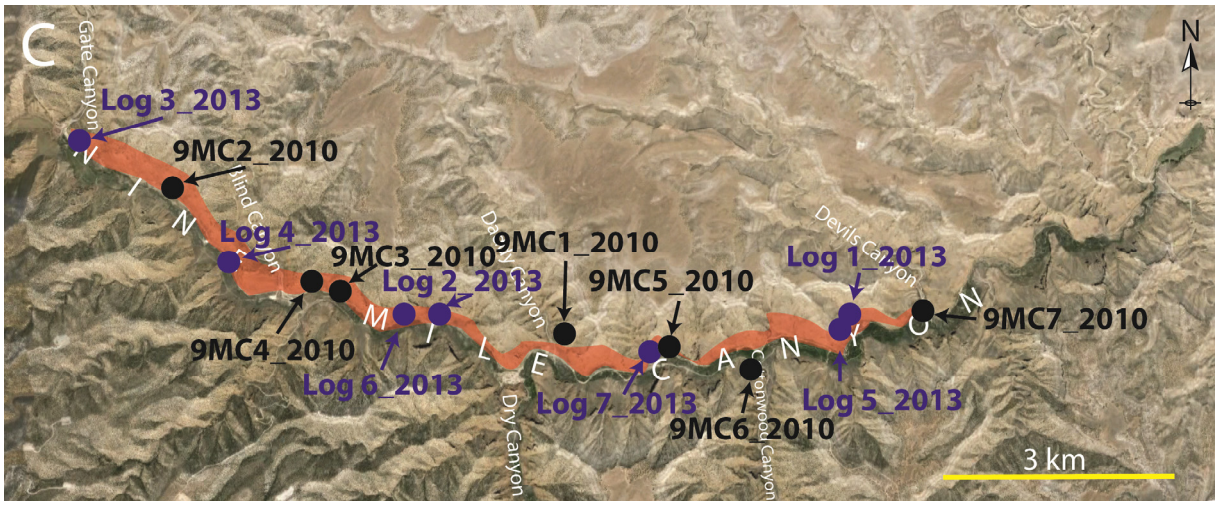

Fig. A.1. Location of logs in the study area.

Table A.1. Summary of the log coordinates and lengths.

Log name	Start coordinates	End coordinates	Length	Logging route
Log 1_2013	0575212 W 4404631 N	0575190 W 4404735 N	52.5 m	**Fig. A.2.A**
Log 2_2013	0570118 W 4404717 N	570043 W 4404807 N	98 m	**Fig. A.2.B**
Log 3_2013	0565458 W 4406845 N	565481 W 4406958 N	74 m	**Fig. A.2.C**
Log 4_2013	0567457 W 4405263 M	567523 W 4405397 N	60 m	**Fig. A.2.D**
Log 5_2013	0575030 W 4404452 N	574965 W 4404433 N	35 m	**Fig. A.2.E**
Log 6_2013	0569491 W 4404750 N	569876 W 4404737 N	85 m	**Fig. A.2.F**
Log 7_2013	572662 W 4404308 N	572620 W 4404303 N	26.5 m	**Fig. A.2.G**
9MC1 2010	N/A	N/A	158 m	**Fig. A.3.A**
9MC2 2010	566775 W 4406147 N	566849 W 4406206 N	62 m	**Fig. A.3.B**
9MC3 2010	568780 W 4404956 N	568740 W 4404984 N	18.5 m	**Fig. A.3.C**
9MC4 2010	568457 W 4405038 N	568487 W 4405096 N	34.5 m	**Fig. A.3.D**
9MC5 2010	572980 W 4404287 N	572999 W 4404517 N	50 m	**Fig. A.3.E**
9MC6 2010	574066 W 4404063 N	574015 W 4404032 N	35.5 m	**Fig. A.3.F**
9MC7 2010	575957 W 4404793 N	575945 W 4404827 N	36 m	**Fig. A.3.G**

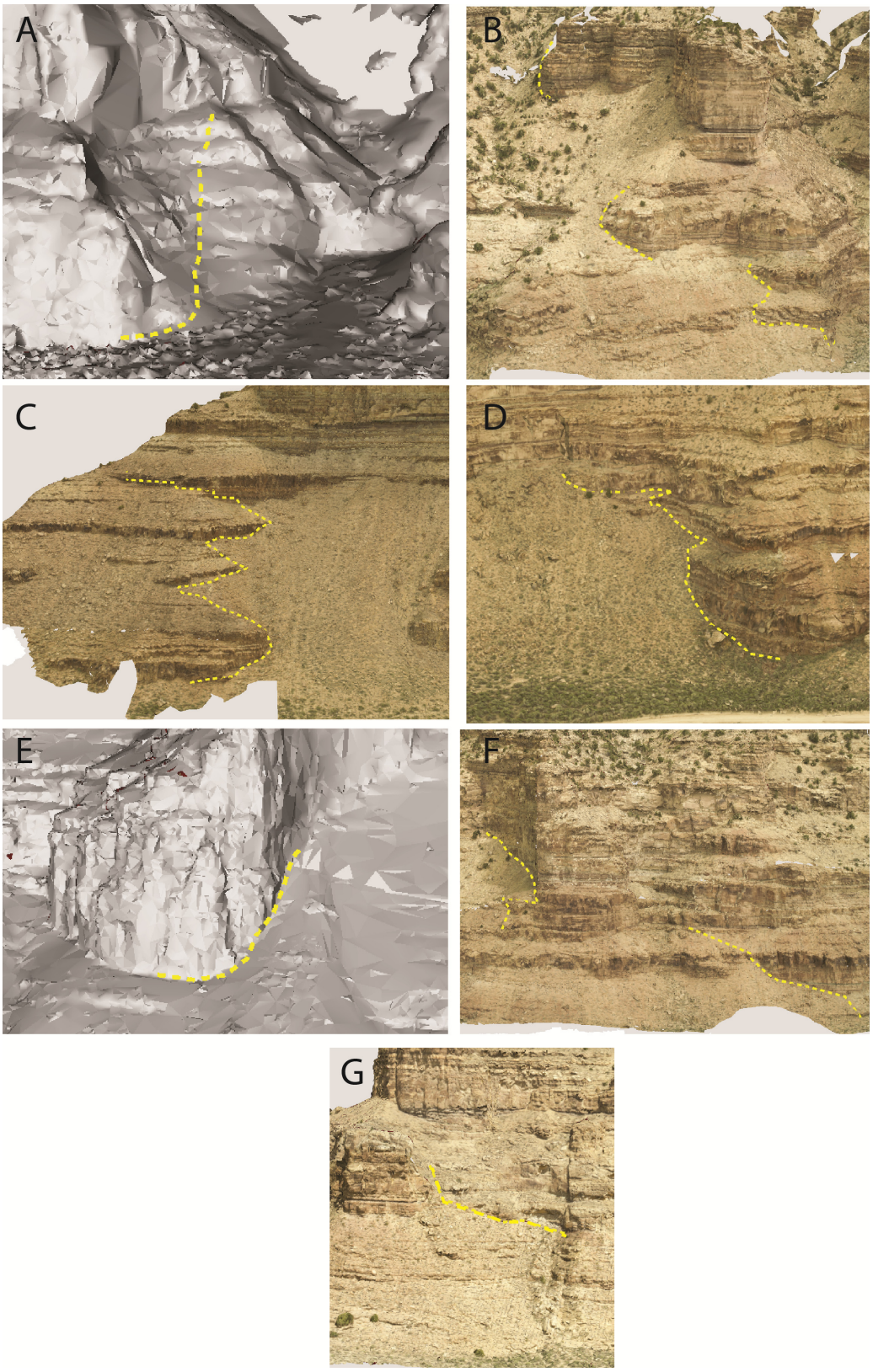

Fig. A.2 Logging routes anno 2013 traced onto the Virtual Outcrop. See log length in **Table A.1** for scale. (**A**) Log 1 2013 (**B**) Log 2 2013 (**C**) log 3 2013 (**D**) Log 4 2013 (**E**) log 5 2013 (**F**) log 6 2013 (**G**) log 7 2013

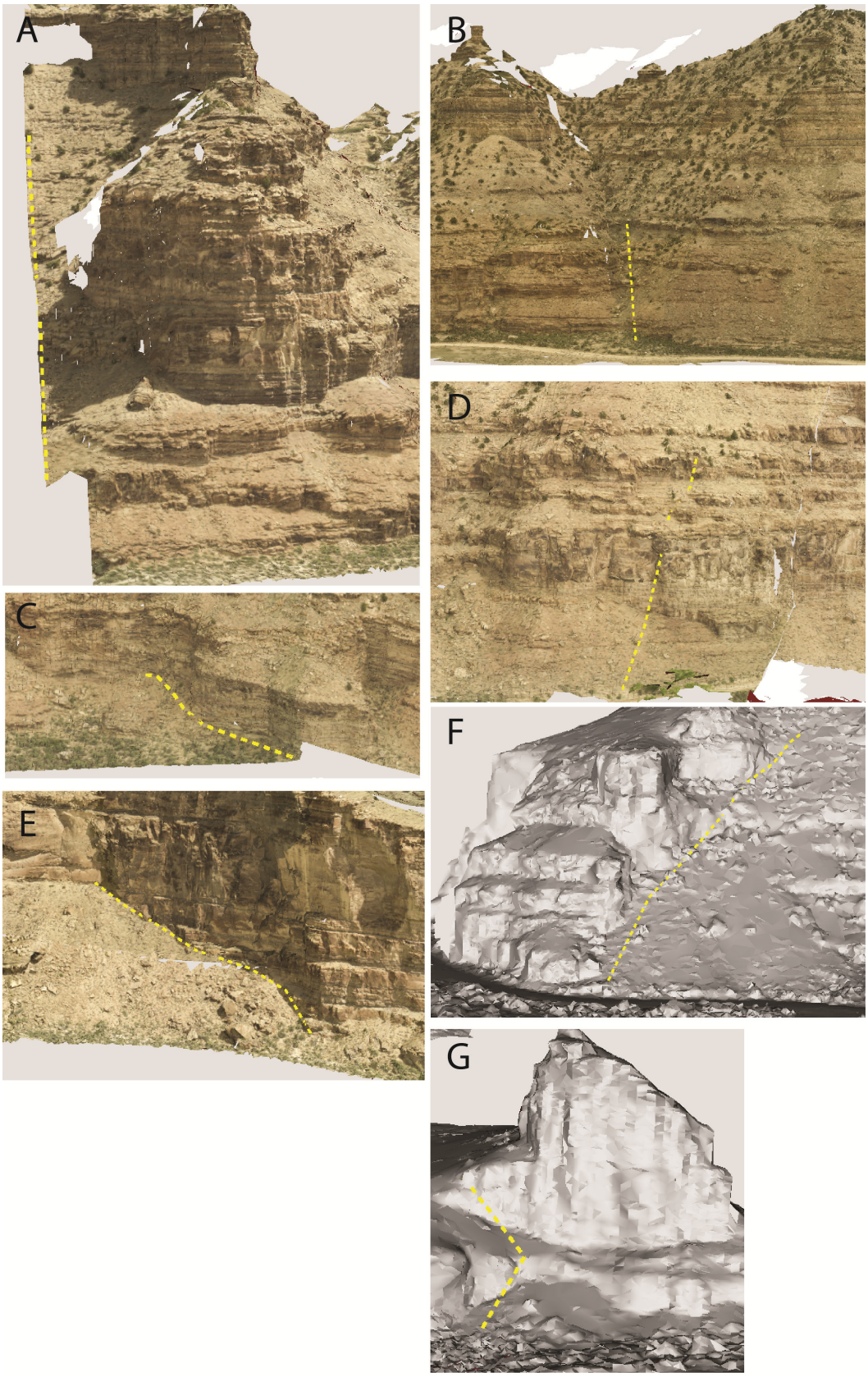

Fig. A.3 Rittersbacher's logging routes anno 2010 traced onto the Virtual Outcrop. Based on log coordinates. See log length in **Table A.1** for scale. (**A**) 9MC1 2010 (**B**) 9MC2 2010 (**C**) 9MC3 2010 (**D**) 9MC4 2010 (**E**) 9MC5 2010 (**F**) 9MC6 2010 (**G**) 9MC7 2010

Legend

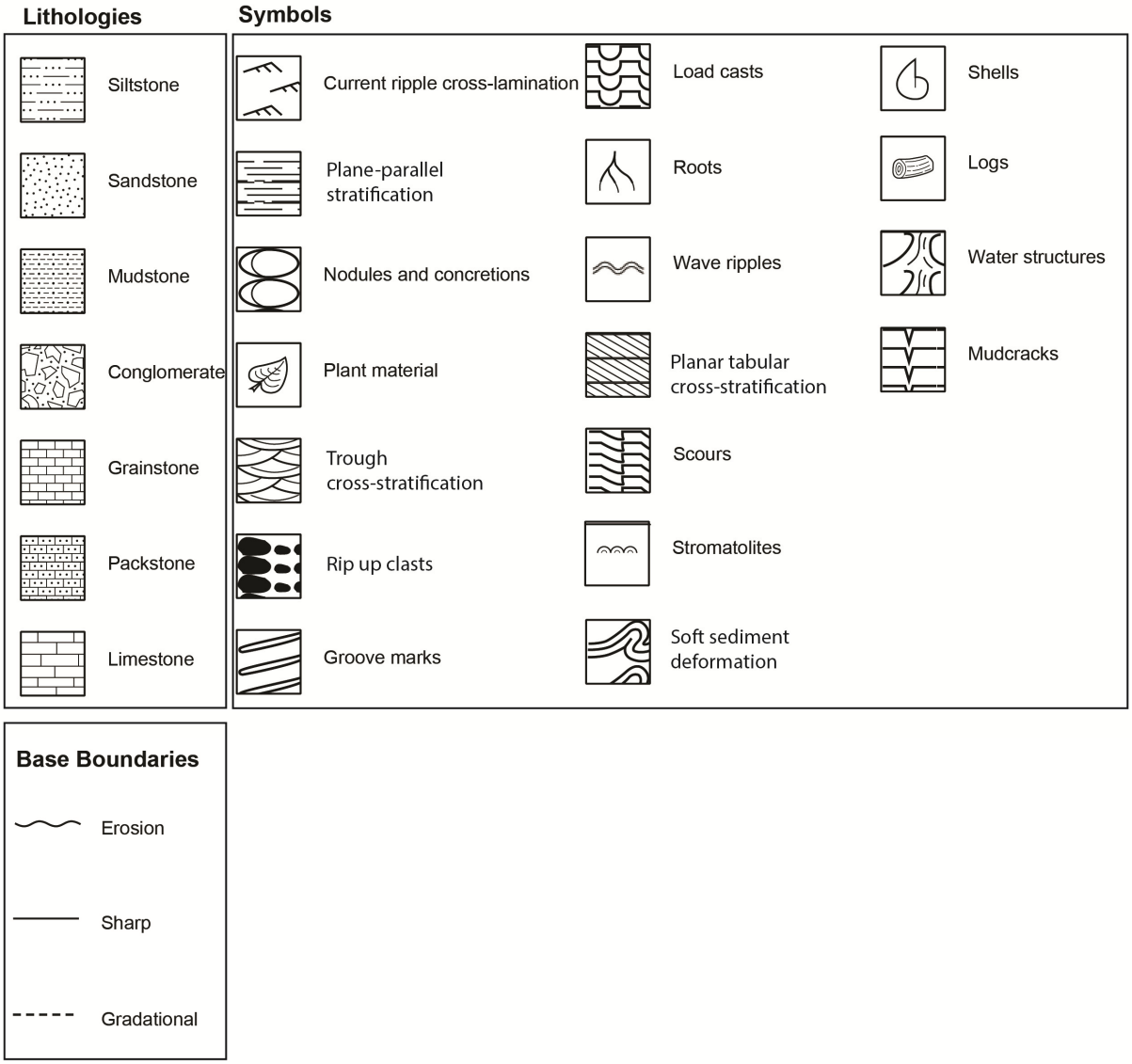
Lithologies
Siltstone
Sandstone
Mudstone
Conglomerate
Grainstone
Packstone
Limestone
Symbols
Current ripple cross-lamination
Plane-parallel stratification
Nodules and concretions
Plant material
Trough cross-stratification
Rip up clasts
Groove marks
Load casts
Roots
Wave ripples
Planar tabular cross-stratification
Scours
Stromatolites
Soft sediment deformation
Shells
Logs
Water structures
Mudcracks
Base Boundaries
Erosion
Sharp
Gradational

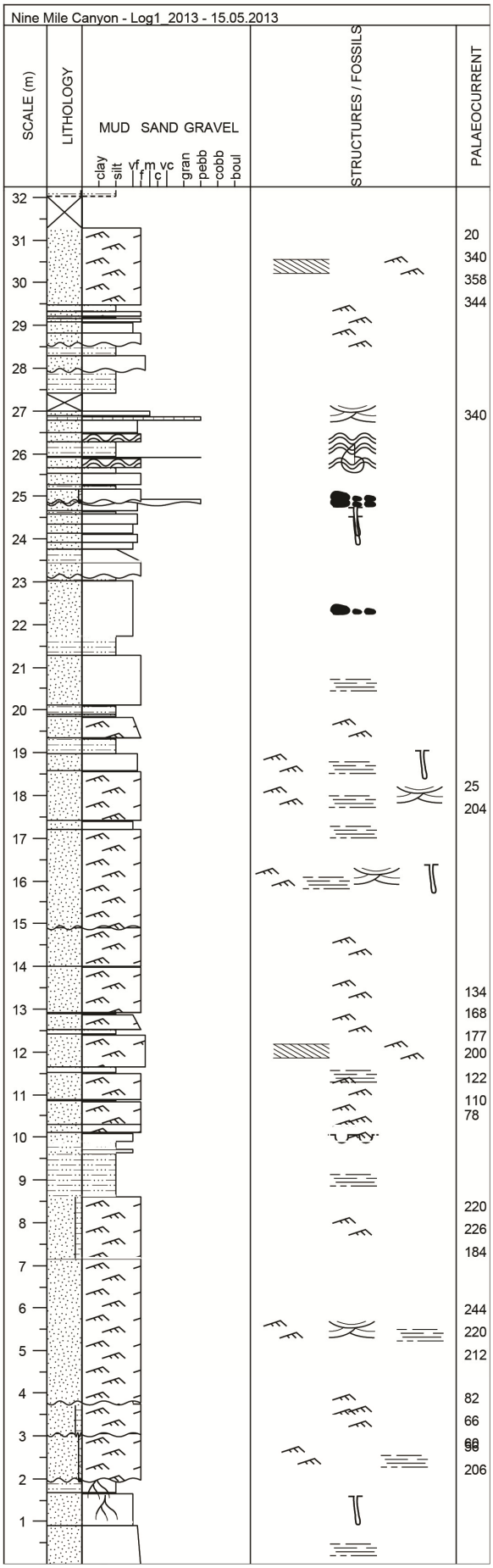
Nine Mile Canyon - Log1_2013 - 15.05.2013
SCALE (m)
LITHOLOGY
MUD SAND GRAVEL
clay silt vf f m c vc gran pebb cobb boul
STRUCTURES / FOSSILS
PALAEOCURRENT
32 31 30 29 28 27 26 25 24 23 22 21 20 19 18 17 16 15 14 13 12 11 10 9 8 7 6 5 4 3 2 1
20 340 358 344 340 25 204 134 168 177 200 122 110 78 220 226 184 244 220 212 82 66 206

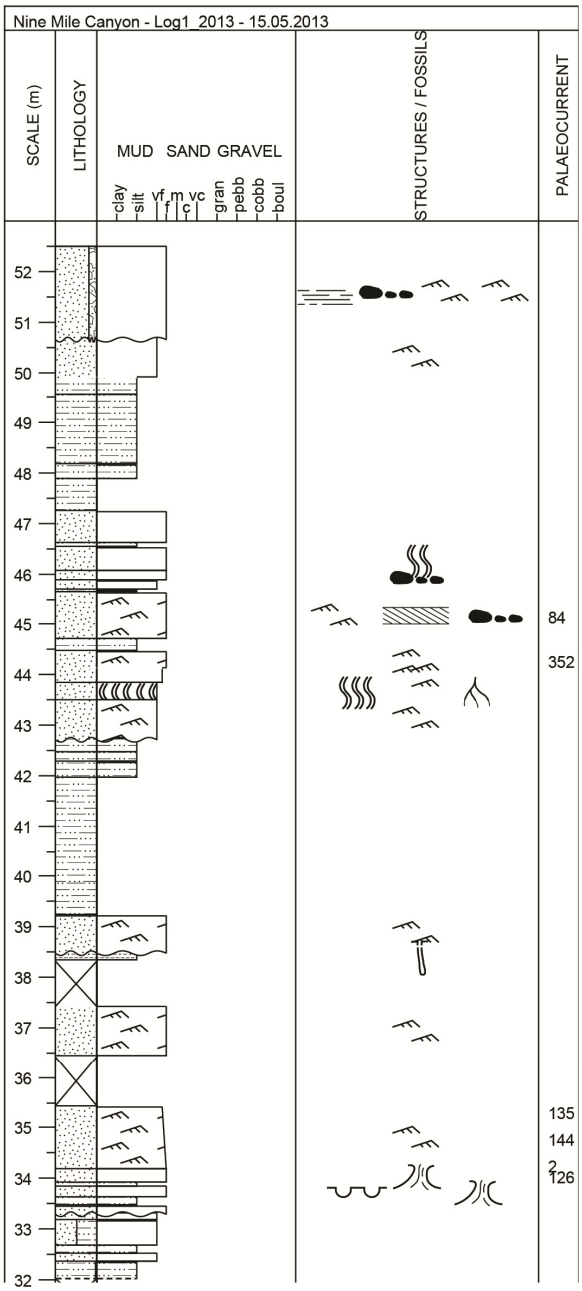
Nine Mile Canyon - Log1_2013 - 15.05.2013
SCALE (m)
LITHOLOGY
MUD SAND GRAVEL
clay silt vf f m c vc gran pebb cobb boul
STRUCTURES / FOSSILS
PALAEOCURRENT
52 51 50 49 48 47 46 45 44 43 42 41 40 39 38 37 36 35 34 33 32
84 352 135 144 126

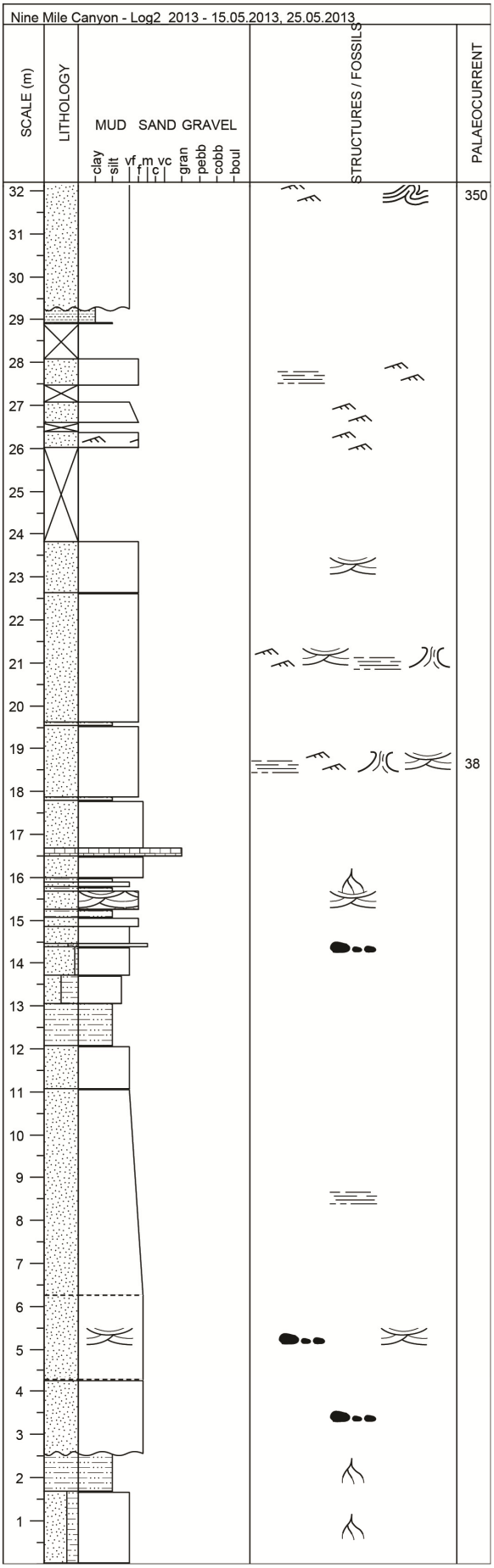
Nine Mile Canyon - Log2 2013 - 15.05.2013, 25.05.2013
SCALE (m)
LITHOLOGY
MUD SAND GRAVEL
clay silt vf f m c vc gran pebb cobb boul
STRUCTURES / FOSSILS
PALAEOCURRENT
350
38

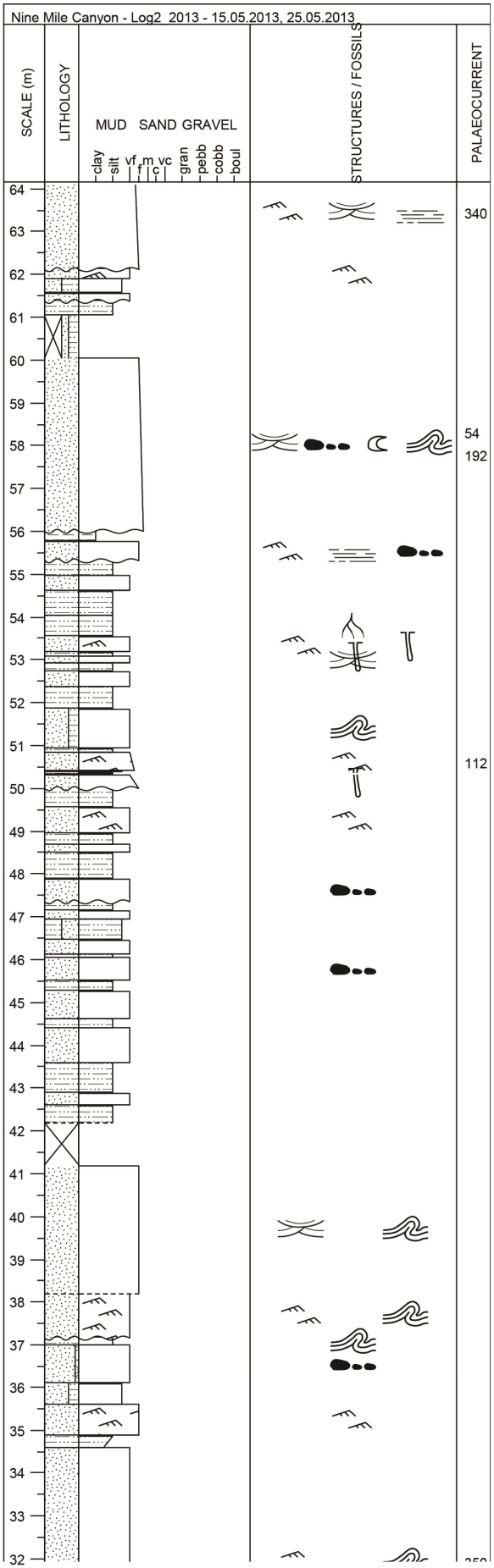
Nine Mile Canyon - Log2 2013 - 15.05.2013, 25.05.2013
SCALE (m)
LITHOLOGY
MUD SAND GRAVEL
clay silt vf f m c vc gran pebb cobb boul
STRUCTURES / FOSSILS
PALAEOCURRENT
340
54
192
112

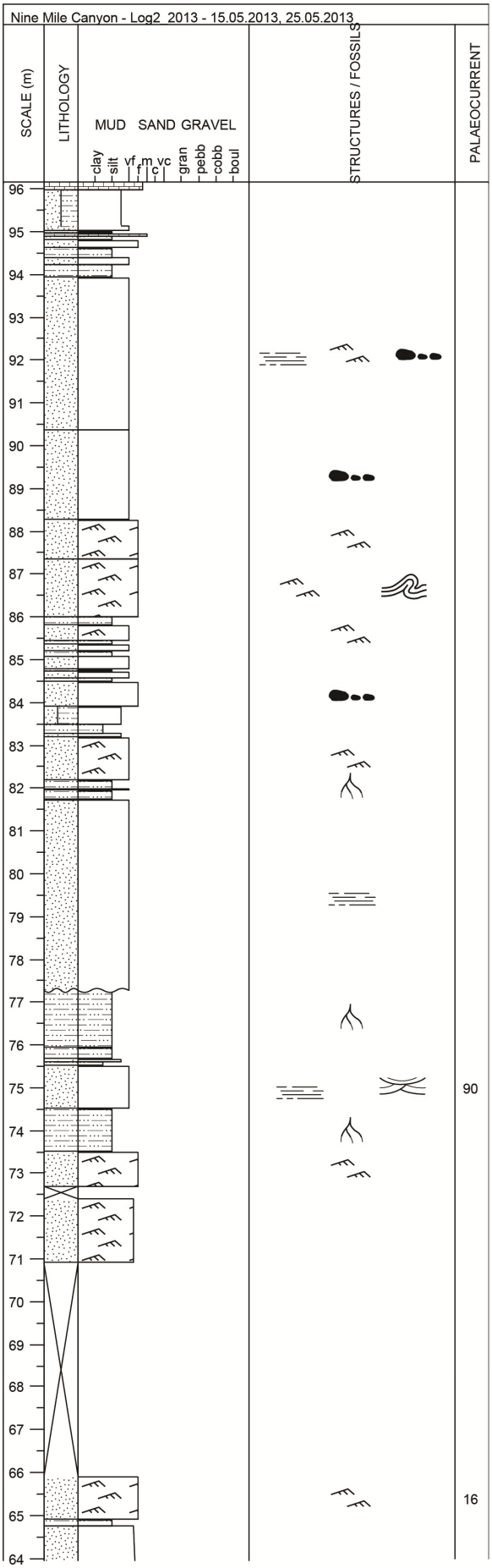
Nine Mile Canyon - Log2 2013 - 15.05.2013, 25.05.2013
SCALE (m)
LITHOLOGY
MUD SAND GRAVEL
clay silt vf f m c vc gran pebb cobb boul
STRUCTURES / FOSSILS
PALAEOCURRENT
96
95
94
93
92
91
90
89
88
87
86
85
84
83
82
81
80
79
78
77
76
75
74
73
72
71
70
69
68
67
66
65
64
90
16

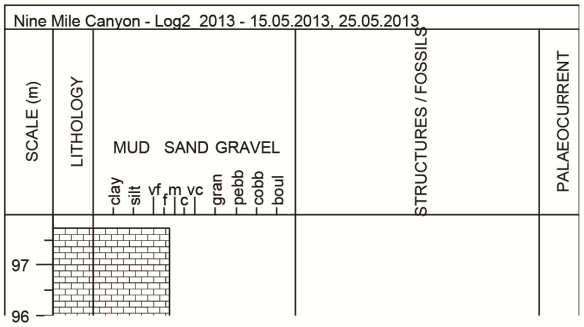
Nine Mile Canyon - Log2 2013 - 15.05.2013, 25.05.2013
SCALE (m)
LITHOLOGY
MUD SAND GRAVEL
clay silt vf f m c vc gran pebb cobb boul
STRUCTURES / FOSSILS
PALAEOCURRENT
97
96

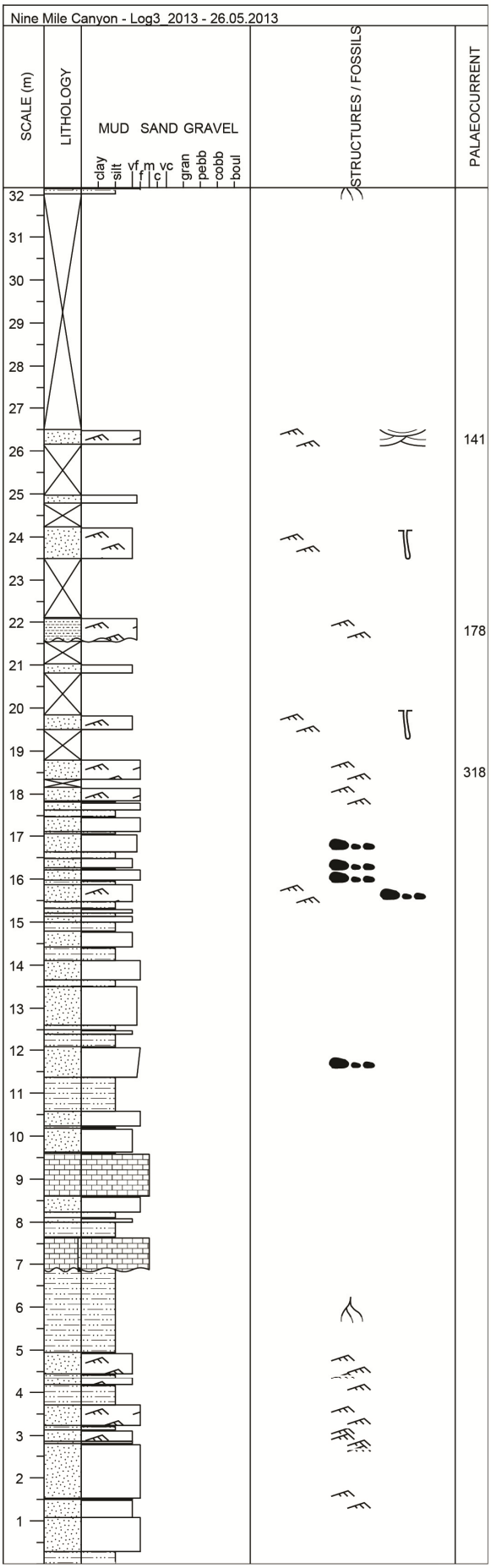
Nine Mile Canyon - Log3_2013 - 26.05.2013
SCALE (m)
LITHOLOGY
MUD SAND GRAVEL
clay silt vf f m c vc gran pebb cobb boul
STRUCTURES / FOSSILS
PALAEOCURRENT
141
178
318

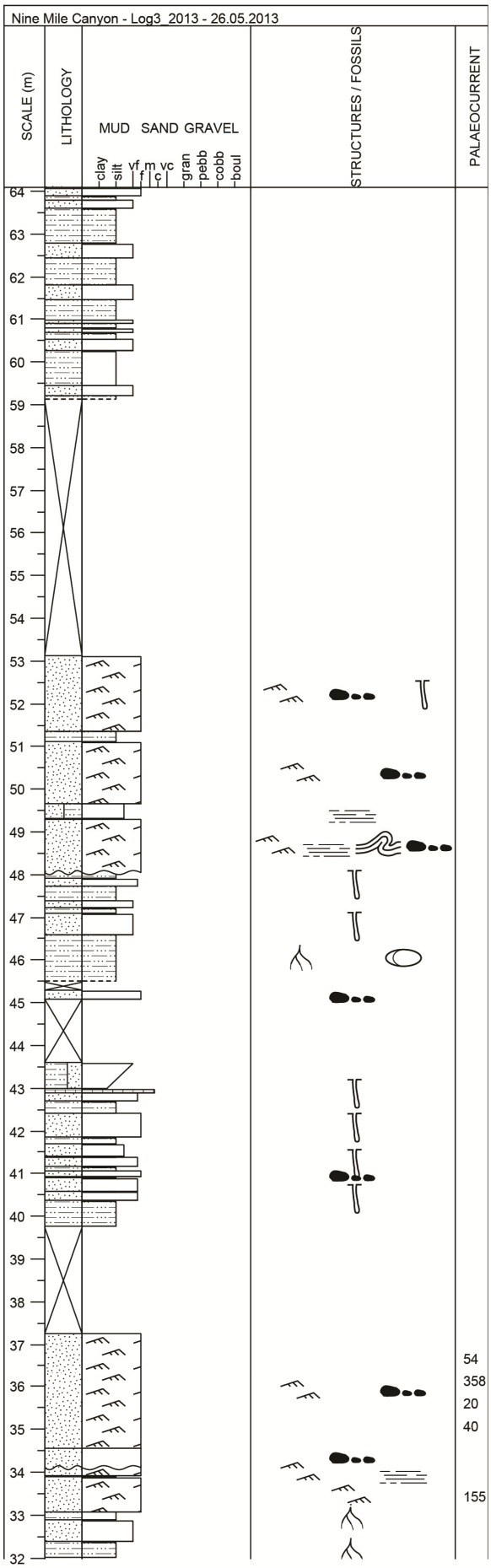
Nine Mile Canyon - Log3_2013 - 26.05.2013
SCALE (m)
LITHOLOGY
MUD SAND GRAVEL
clay silt vf f m c vc gran pebb cobb boul
STRUCTURES / FOSSILS
PALAEOCURRENT
54
358
20
40
155

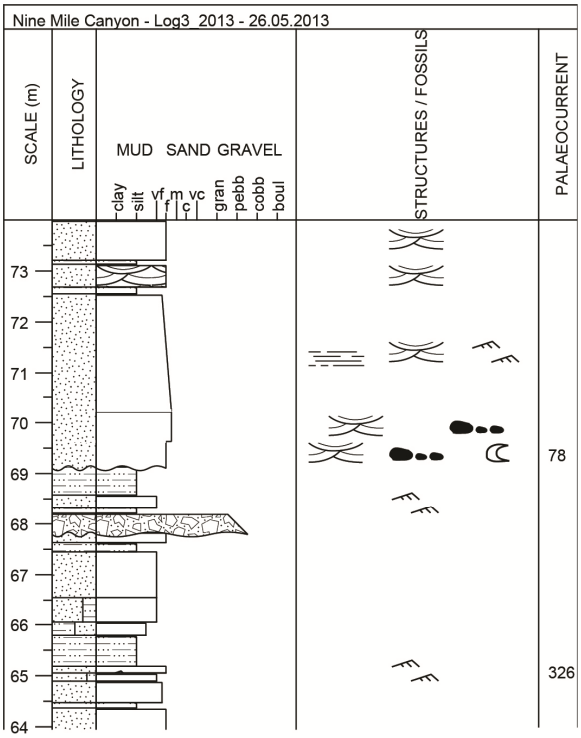
Nine Mile Canyon - Log3_2013 - 26.05.2013
SCALE (m)
LITHOLOGY
MUD SAND GRAVEL
clay
silt
vf
f
m
c
vc
gran
pebb
cobb
boul
STRUCTURES / FOSSILS
PALAEOCURRENT
73
72
71
70
69
68
67
66
65
64
78
326

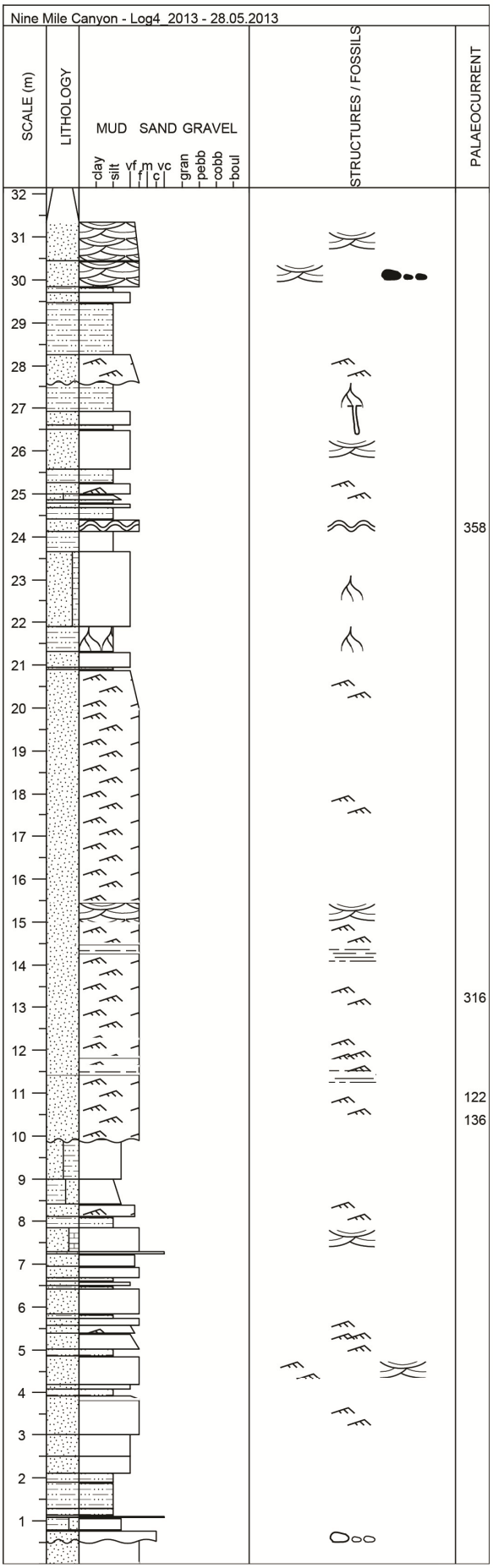
Nine Mile Canyon - Log4_2013 - 28.05.2013
SCALE (m)
LITHOLOGY
MUD SAND GRAVEL
clay silt vf f m c vc gran pebb cobb boul
STRUCTURES / FOSSILS
PALAEOCURRENT
358
316
122
136

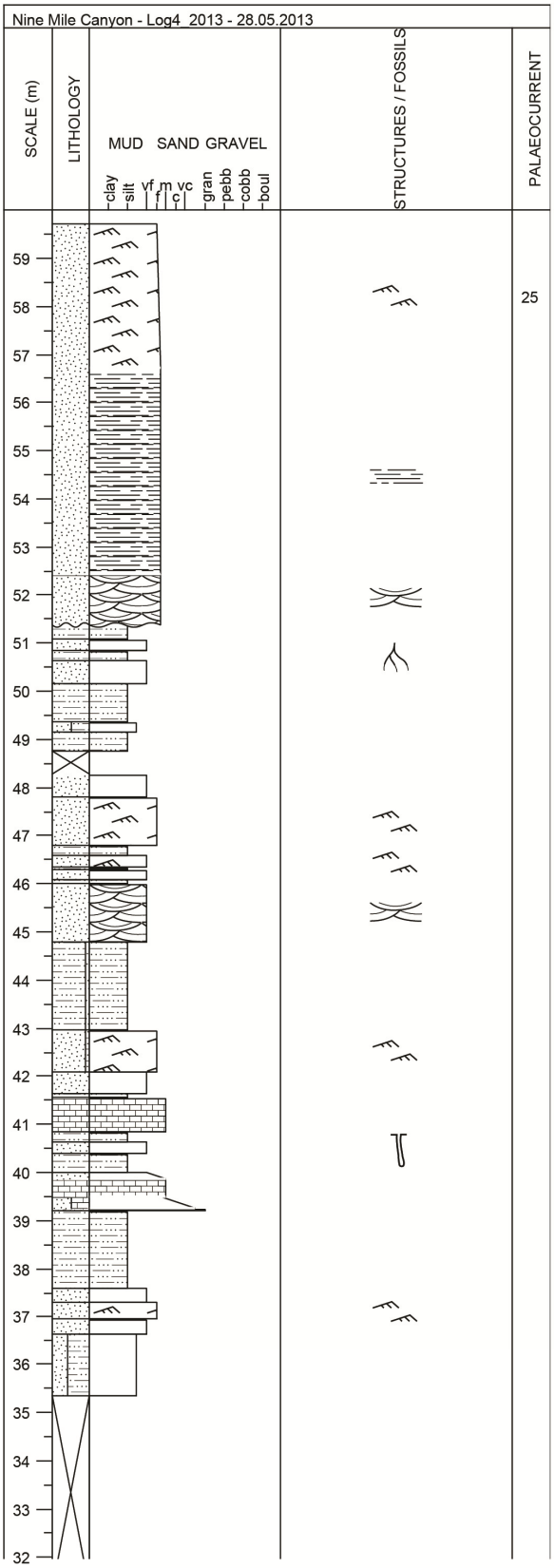
Nine Mile Canyon - Log4_2013 - 28.05.2013
SCALE (m)
LITHOLOGY
MUD SAND GRAVEL
clay silt vf f m c vc gran pebb cobb boul
STRUCTURES / FOSSILS
PALAEOCURRENT
25

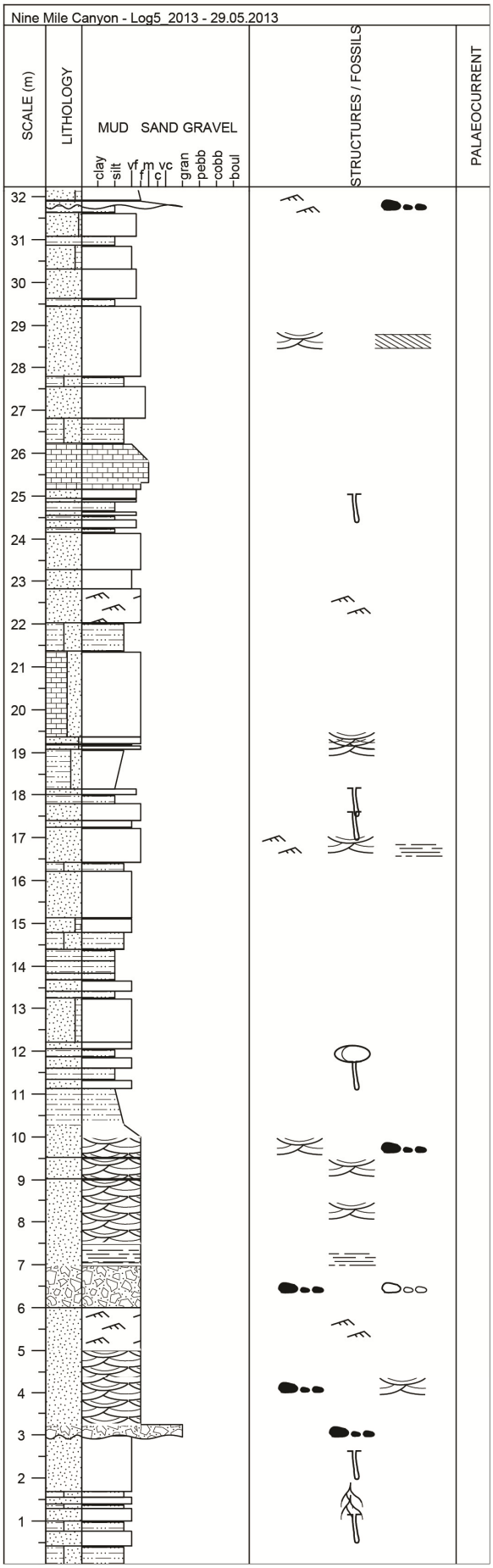
Nine Mile Canyon - Log5_2013 - 29.05.2013
SCALE (m)
LITHOLOGY
MUD SAND GRAVEL
clay silt vf f m c vc gran pebb cobb boul
STRUCTURES / FOSSILS
PALAEOCURRENT
32 31 30 29 28 27 26 25 24 23 22 21 20 19 18 17 16 15 14 13 12 11 10 9 8 7 6 5 4 3 2 1

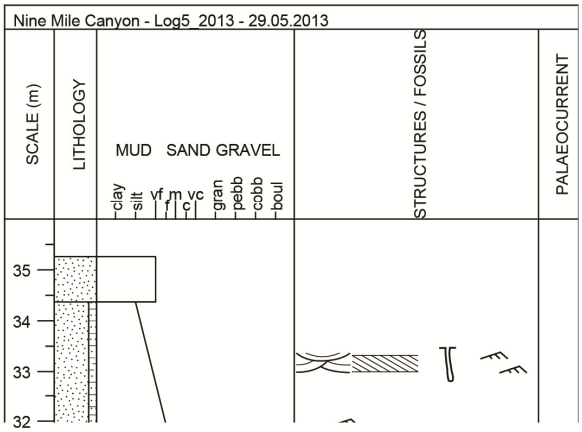
Nine Mile Canyon - Log5_2013 - 29.05.2013
SCALE (m)
LITHOLOGY
MUD SAND GRAVEL
clay silt vf f m c vc gran pebb cobb boul
STRUCTURES / FOSSILS
PALAEOCURRENT
35 34 33 32

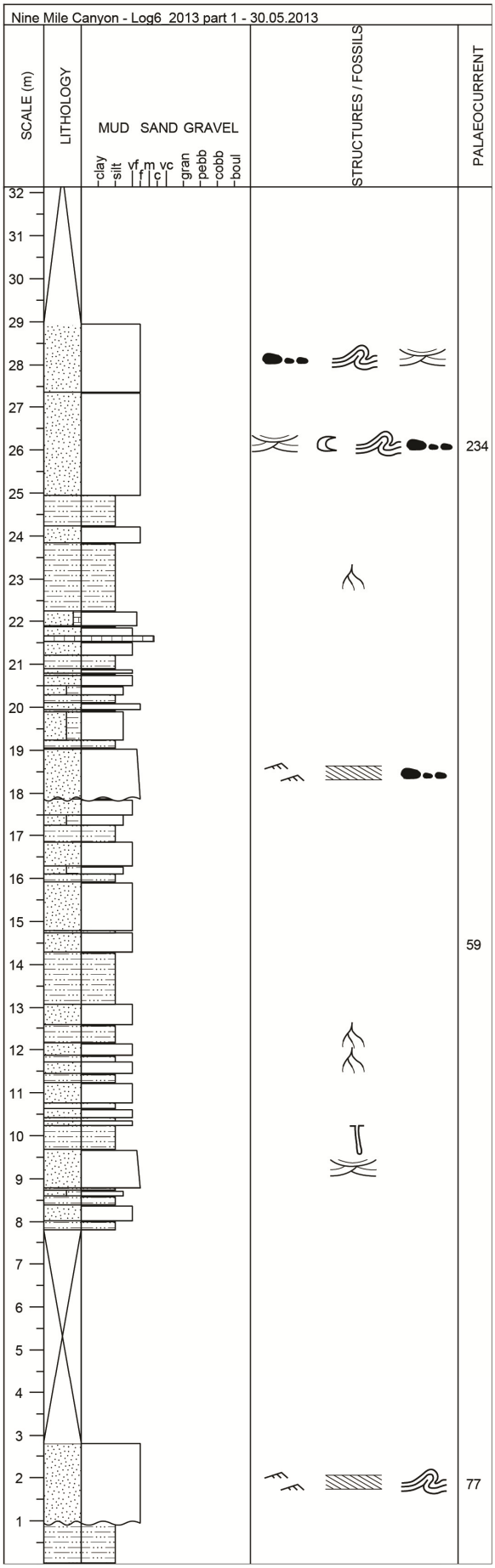
Nine Mile Canyon - Log6 2013 part 1 - 30.05.2013
SCALE (m)
LITHOLOGY
MUD SAND GRAVEL
clay silt vf f m c vc gran pebb cobb boul
STRUCTURES / FOSSILS
PALAEOCURRENT
234
59
77

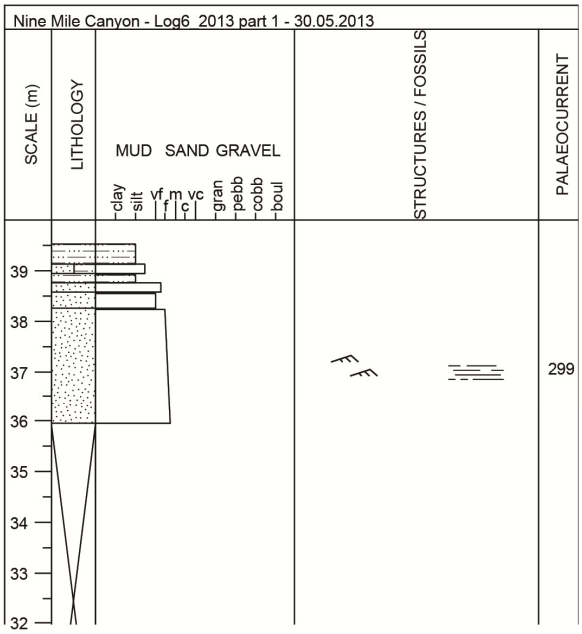
Nine Mile Canyon - Log6 2013 part 1 - 30.05.2013
SCALE (m)
LITHOLOGY
MUD SAND GRAVEL
clay silt vf f m c vc gran pebb cobb boul
STRUCTURES / FOSSILS
PALAEOCURRENT
299

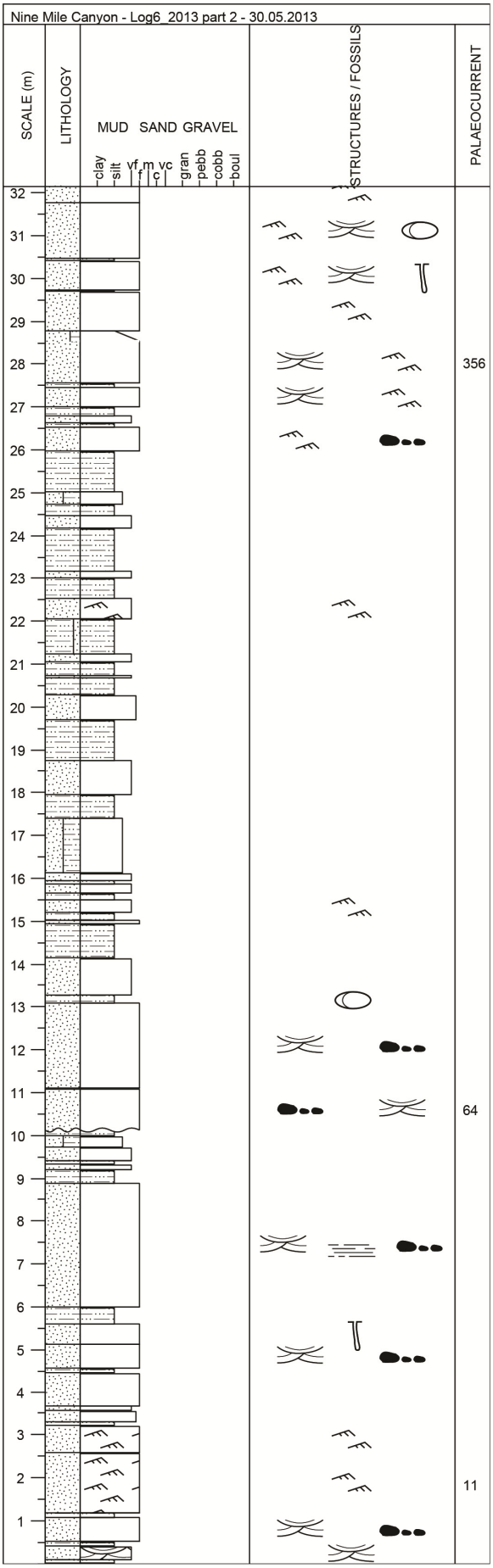
Nine Mile Canyon - Log6_2013 part 2 - 30.05.2013
SCALE (m)
LITHOLOGY
MUD SAND GRAVEL
clay silt vf f m c vc gran pebb cobb boul
STRUCTURES / FOSSILS
PALAEOCURRENT
356
64
11

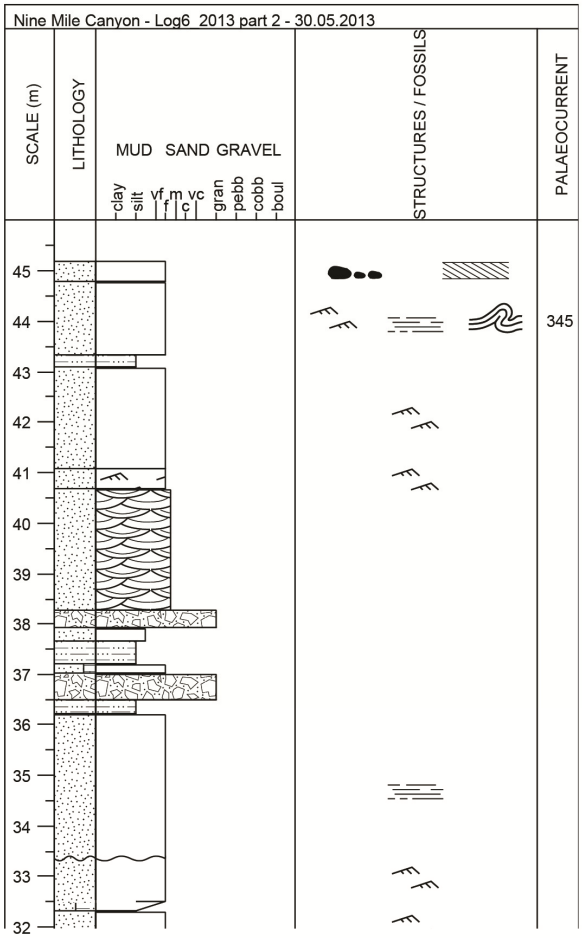
Nine Mile Canyon - Log6_2013 part 2 - 30.05.2013
SCALE (m)
LITHOLOGY
MUD SAND GRAVEL
clay silt vf f m c vc gran pebb cobb boul
STRUCTURES / FOSSILS
PALAEOCURRENT
345

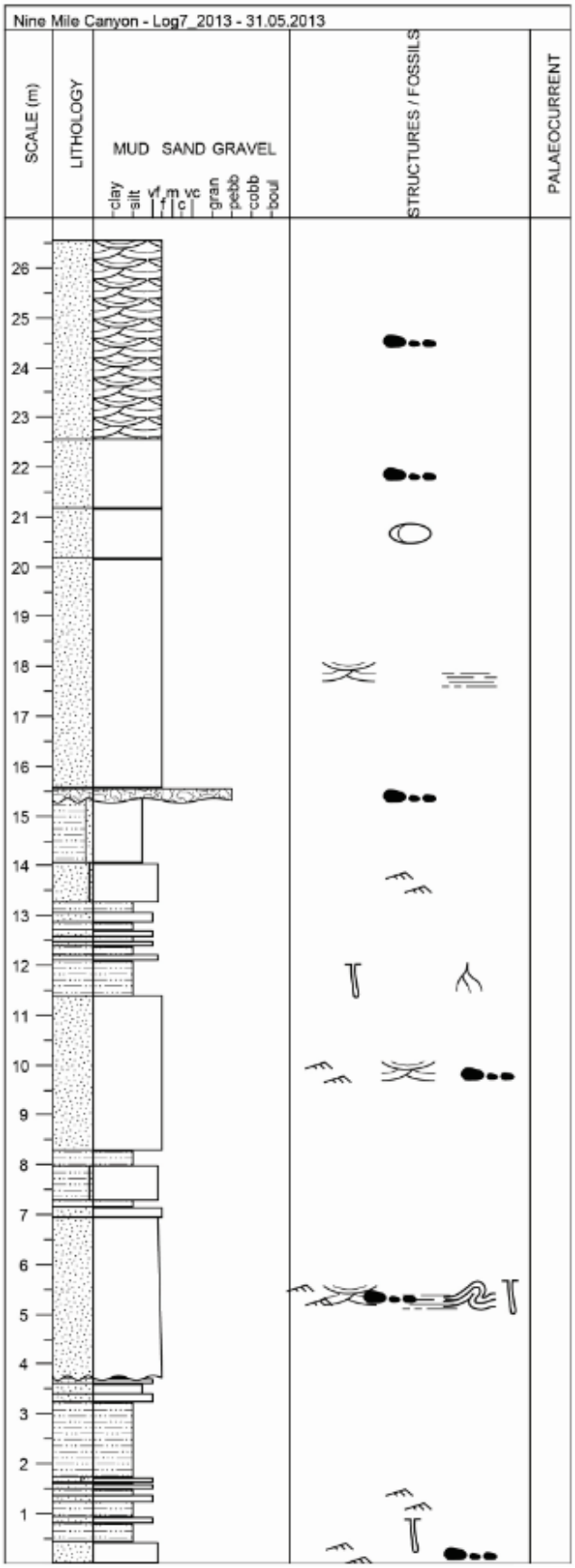
Nine Mile Canyon - Log7_2013 - 31.05.2013
SCALE (m)
LITHOLOGY
MUD SAND GRAVEL
clay
silt
vf
f
m
c
vc
gran
pebb
cobb
boul
STRUCTURES / FOSSILS
PALAEOCURRENT
26
25
24
23
22
21
20
19
18
17
16
15
14
13
12
11
10
9
8
7
6
5
4
3
2
1

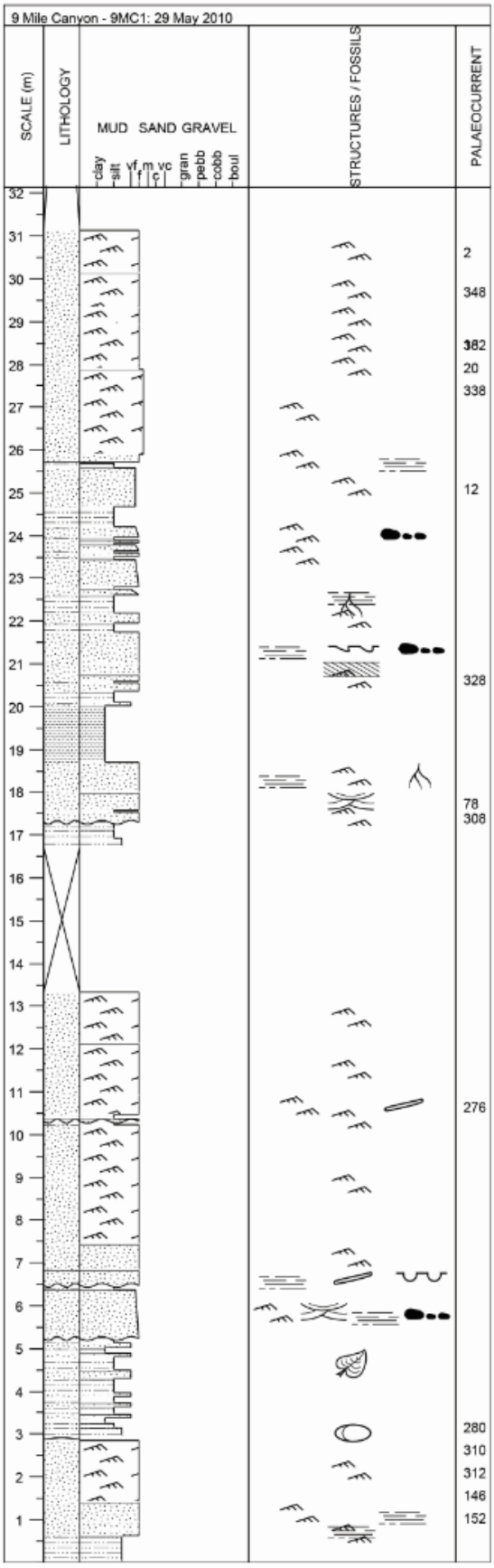
9 Mile Canyon - 9MC1: 29 May 2010
SCALE (m)
LITHOLOGY
MUD SAND GRAVEL
clay silt vf f m c vc gran pebb cobb boul
STRUCTURES / FOSSILS
PALAEOCURRENT
2
348
182
20
338
12
328
78
308
276
280
310
312
146
152

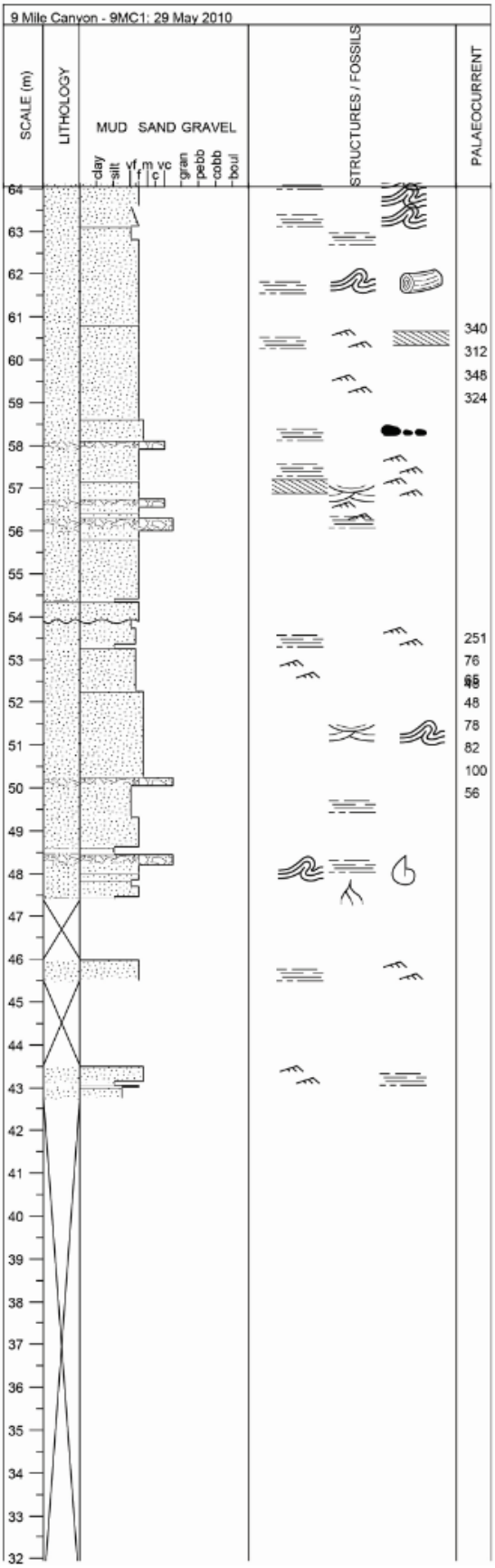
9 Mile Canyon - 9MC1: 29 May 2010
SCALE (m)
LITHOLOGY
MUD SAND GRAVEL
clay silt vf f m c vc gran pebb cobb boul
STRUCTURES / FOSSILS
PALAEOCURRENT
340
312
348
324
251
76
48
78
82
100
56

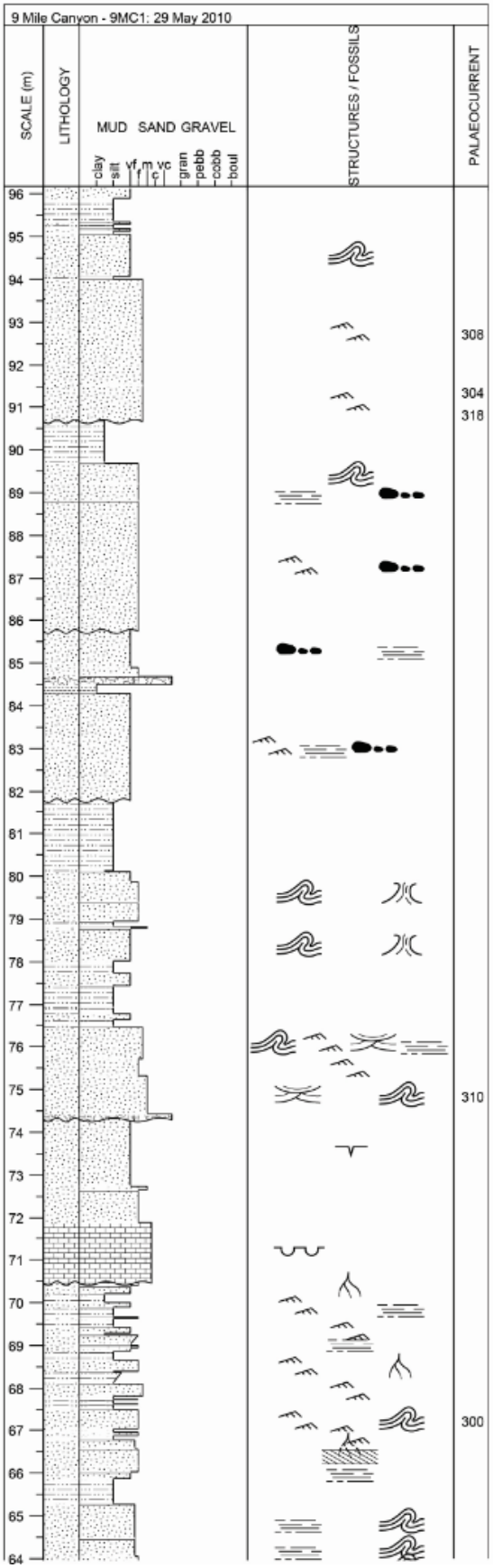
9 Mile Canyon - 9MC1: 29 May 2010
SCALE (m)
LITHOLOGY
MUD SAND GRAVEL
clay silt vf f m c vc gran pebb cobb boul
STRUCTURES / FOSSILS
PALAEOCURRENT
308
304
318
310
300

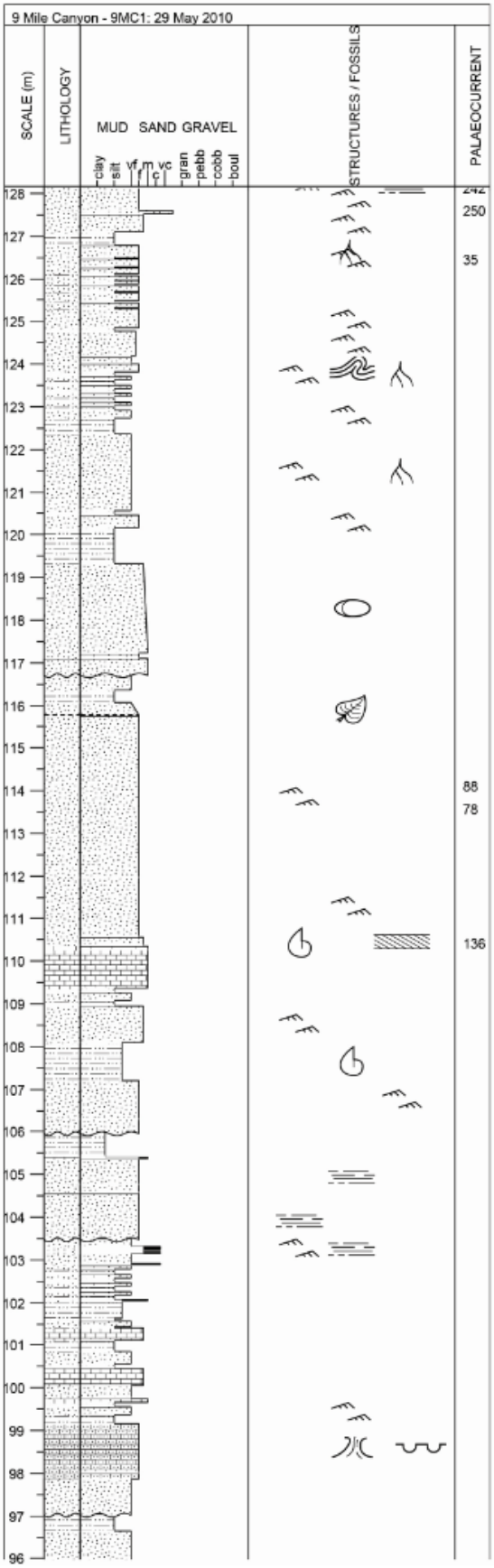
9 Mile Canyon - 9MC1: 29 May 2010
SCALE (m)
LITHOLOGY
MUD SAND GRAVEL
clay silt vf f m c vc gran pebb cobb boul
STRUCTURES / FOSSILS
PALAEOCURRENT
250
35
88
78
136

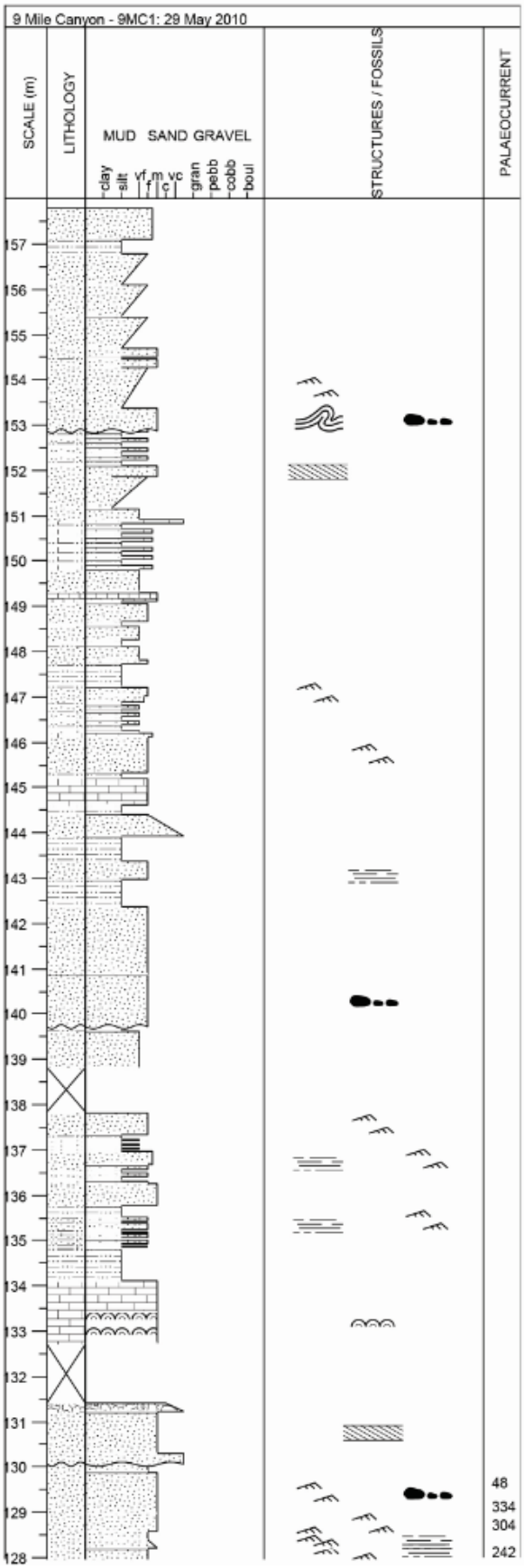
9 Mile Canyon - 9MC1: 29 May 2010
SCALE (m)
LITHOLOGY
MUD SAND GRAVEL
clay
silt
vf
f
m
c
vc
gran
pebb
cobb
boul
STRUCTURES / FOSSILS
PALAEOCURRENT
157
156
155
154
153
152
151
150
149
148
147
146
145
144
143
142
141
140
139
138
137
136
135
134
133
132
131
130
129
128
48
334
304
242

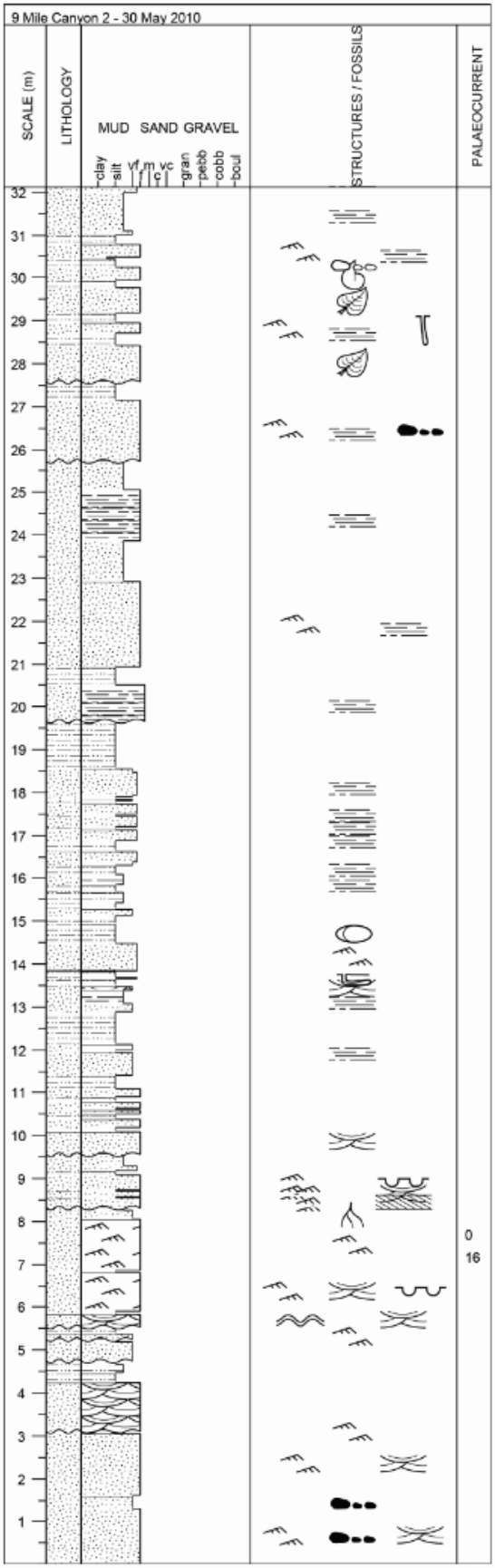
9 Mile Canyon 2 - 30 May 2010
SCALE (m)
LITHOLOGY
MUD SAND GRAVEL
clay silt vf f m c vc gran pebb cobb boul
STRUCTURES / FOSSILS
PALAEOCURRENT
0
16

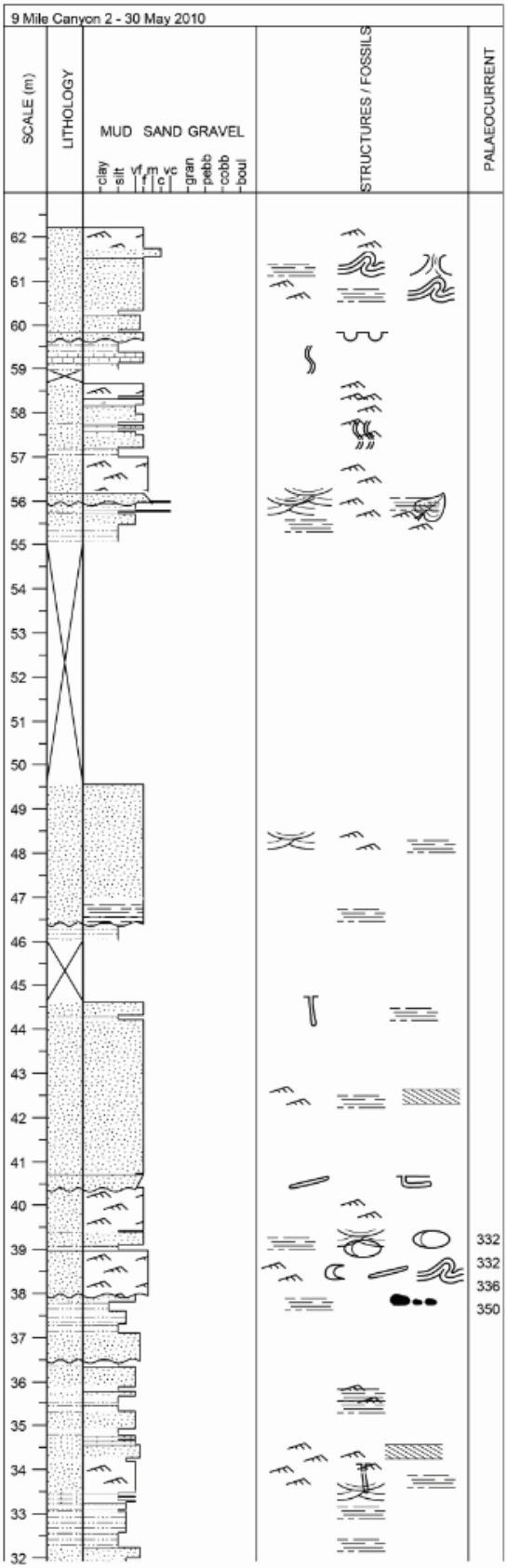
9 Mile Canyon 2 - 30 May 2010
SCALE (m)
LITHOLOGY
MUD SAND GRAVEL
clay silt vf f m c vc gran pebb cobb boul
STRUCTURES / FOSSILS
PALAEOCURRENT
332
332
336
350

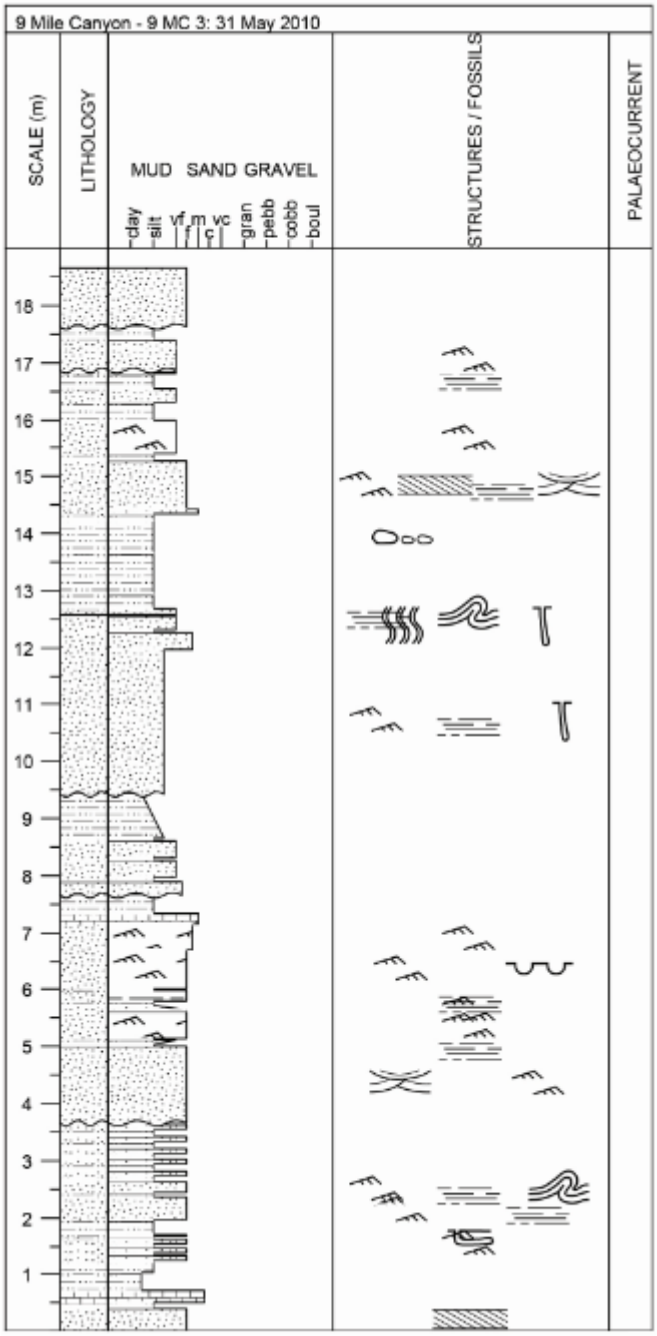
9 Mile Canyon - 9 MC 3: 31 May 2010
SCALE (m)
LITHOLOGY
MUD SAND GRAVEL
clay
silt
vf
f
m
c
vc
gran
pebb
cobb
boul
STRUCTURES / FOSSILS
PALAEOCURRENT
18
17
16
15
14
13
12
11
10
9
8
7
6
5
4
3
2
1

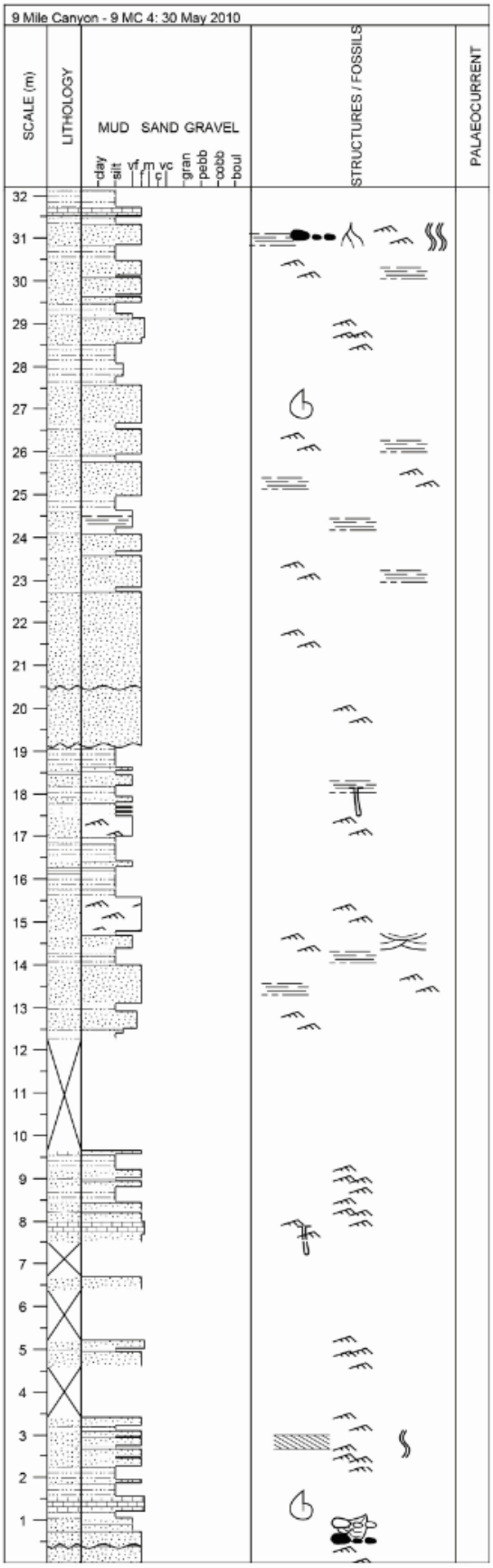
9 Mile Canyon - 9 MC 4: 30 May 2010
SCALE (m)
LITHOLOGY
MUD SAND GRAVEL
clay
silt
vf
f
m
c
vc
gran
pebb
cobb
boul
STRUCTURES / FOSSILS
PALAEOCURRENT
32
31
30
29
28
27
26
25
24
23
22
21
20
19
18
17
16
15
14
13
12
11
10
9
8
7
6
5
4
3
2
1

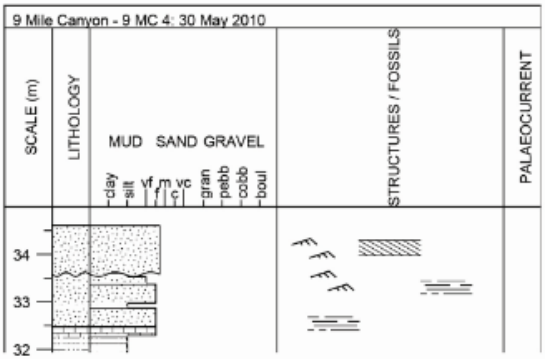
9 Mile Canyon - 9 MC 4: 30 May 2010
SCALE (m)
LITHOLOGY
MUD SAND GRAVEL
clay
silt
vf
f
m
c
vc
gran
pebb
cobb
boul
STRUCTURES / FOSSILS
PALAEOCURRENT
34
33
32

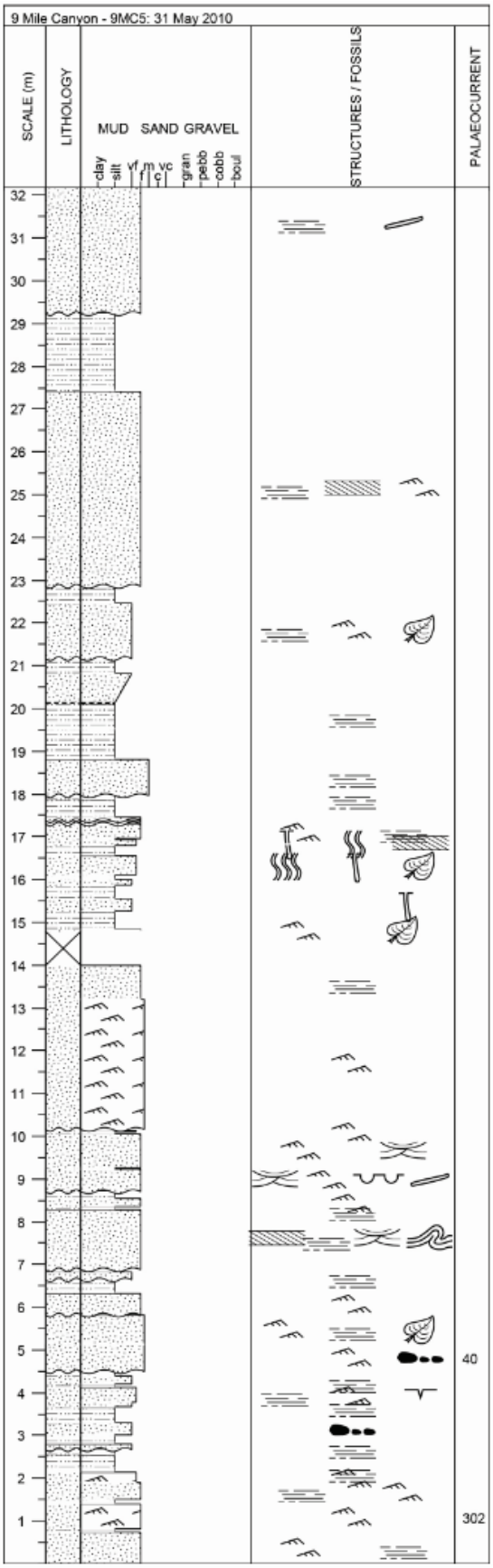
9 Mile Canyon - 9MC5: 31 May 2010
SCALE (m)
LITHOLOGY
MUD SAND GRAVEL
clay silt vf f m c vc gran pebb cobb boul
STRUCTURES / FOSSILS
PALAEOCURRENT
40
302

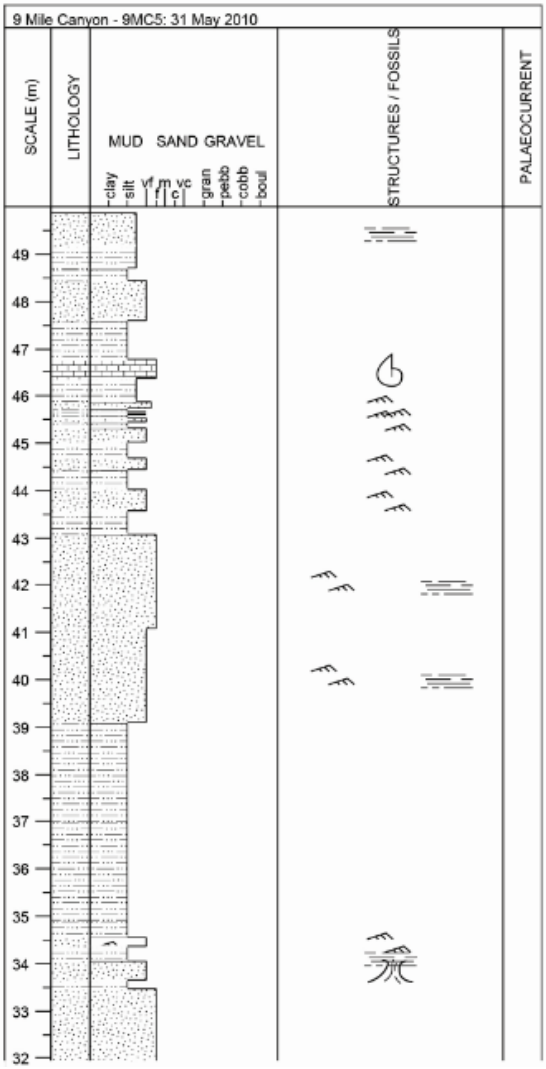
9 Mile Canyon - 9MC5: 31 May 2010
SCALE (m)
LITHOLOGY
MUD SAND GRAVEL
clay silt vf f m c vc gran pebb cobb boul
STRUCTURES / FOSSILS
PALAEOCURRENT

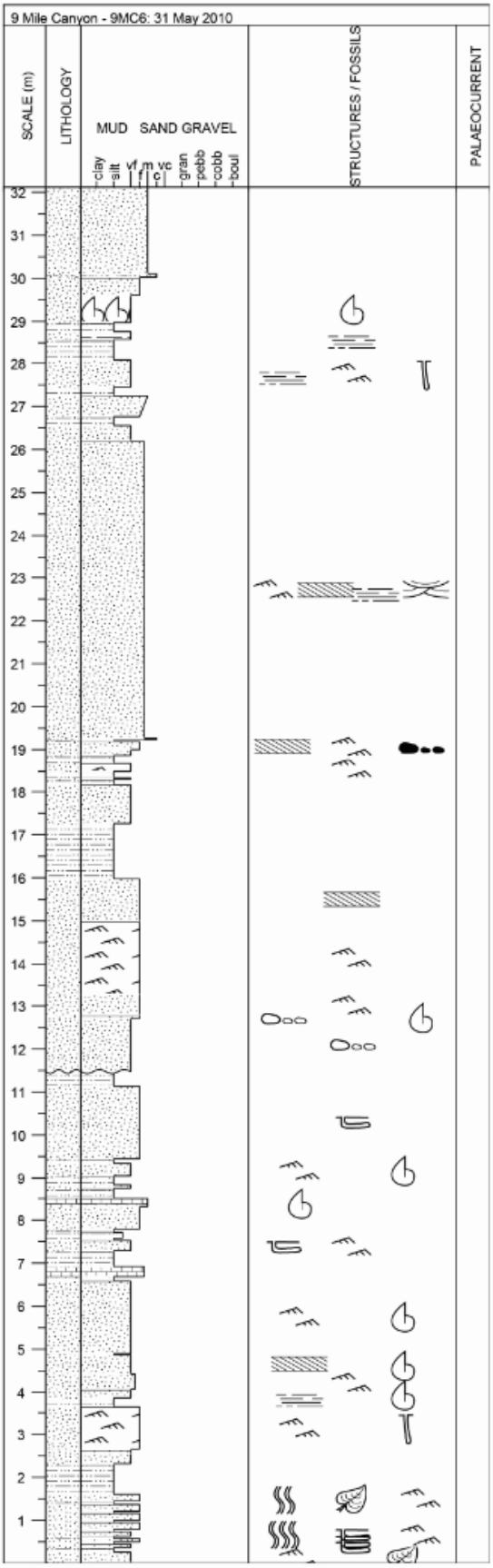
9 Mile Canyon - 9MC6: 31 May 2010
SCALE (m)
LITHOLOGY
MUD SAND GRAVEL
clay silt vf f m c vc gran pebb cobb boul
STRUCTURES / FOSSILS
PALAEOCURRENT
32 31 30 29 28 27 26 25 24 23 22 21 20 19 18 17 16 15 14 13 12 11 10 9 8 7 6 5 4 3 2 1

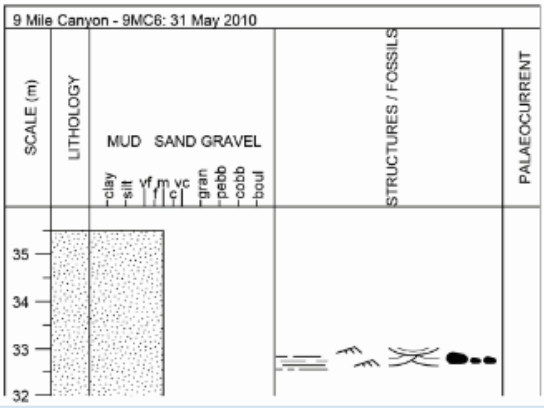
9 Mile Canyon - 9MC6: 31 May 2010
SCALE (m)
LITHOLOGY
MUD SAND GRAVEL
clay silt vf f m c vc gran pebb cobb boul
STRUCTURES / FOSSILS
PALAEOCURRENT
35 34 33 32

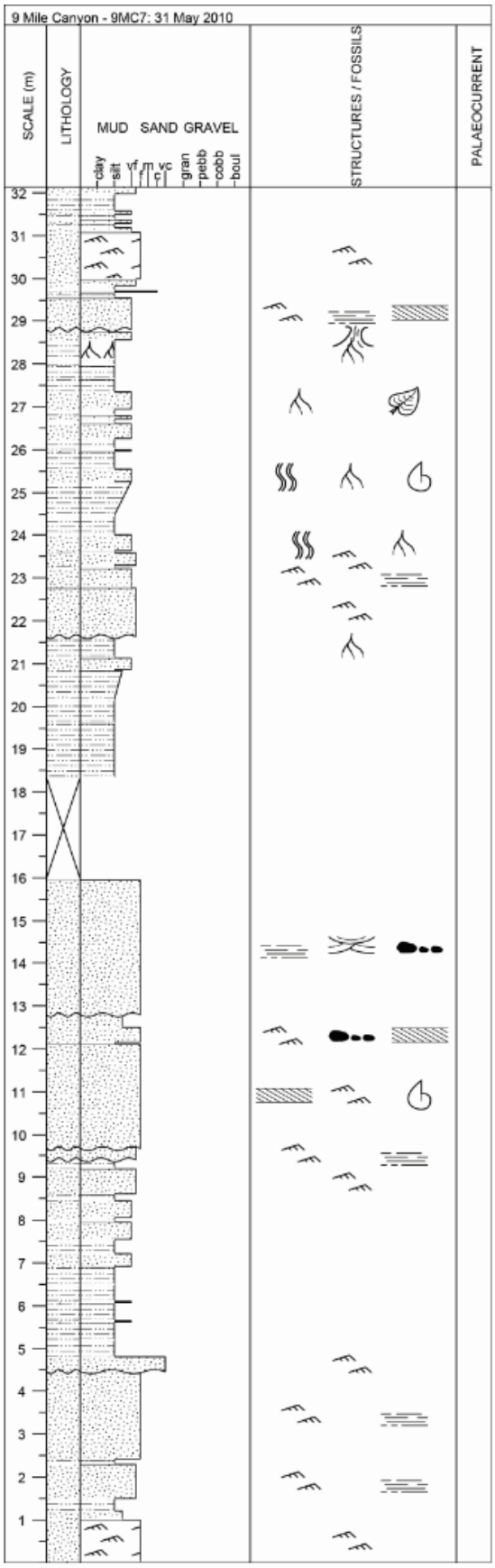
9 Mile Canyon - 9MC7: 31 May 2010
SCALE (m)
LITHOLOGY
MUD SAND GRAVEL
clay silt vf f m c vc gran pebb cobb boul
STRUCTURES / FOSSILS
PALAEOCURRENT

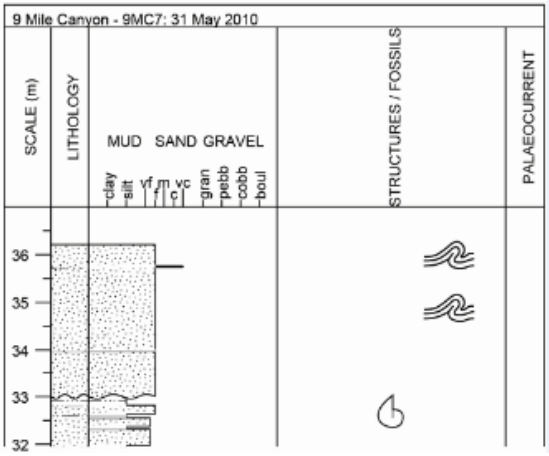
9 Mile Canyon - 9MC7: 31 May 2010
SCALE (m)
LITHOLOGY
MUD SAND GRAVEL
clay silt vf f m c vc gran pebb cobb boul
STRUCTURES / FOSSILS
PALAEOCURRENT